UNIVERSITY OF CALIFORNIA, SAN DIEGO

Constraints on Heterogeneity throughout the Earth's Mantle from Observations of Scattered Seismic Waves

A dissertation submitted in partial satisfaction of the
requirements for the degree
Doctor of Philosophy

in

Earth Sciences

by

Nicholas John Mancinelli

Committee in charge:

Professor Peter M. Shearer, Chair
Professor Peter Gerstoft
Professor T. Guy Masters
Professor Pui-Shum Shing
Professor Dave R. Stegman

2016

The dissertation of Nicholas John Mancinelli is approved, and it is acceptable in quality and form for publication on microfilm and electronically:

_____

_____

_____

_____

_____

Chair

University of California, San Diego

2016

DEDICATION

To Uncle Duke

EPIGRAPH

The game of science is, in principle, without end.
He who decides one day that scientific statements do not call for any further test,
and that they can be regarded as finally verified, retires from the game.

– Karl Popper
The Logic of Scientific Discovery, 1934

TABLE OF CONTENTS

Signature Page iii

Dedication iv

Epigraph v

Table of Contents vi

List of Figures ix

List of Tables xiii

Acknowledgements xiv

Vita xviii

Abstract of the Dissertation xix

Chapter 1 Introduction 1
1.1 Earth structure: Length scales and dimensions 1
1.2 Scattering observations 2
1.3 Random media theory 3
1.4 Modeling scattered energy with seismic particles 4
1.5 Thesis overview 6

References 8

Chapter 2 Reconciling discrepancies among estimates of small-scale mantle heterogeneity from PKP precursors 10
2.1 Introduction 11
2.2 Data selection and stacking 12
2.3 Seismic phonon models 15
2.4 Including lithospheric scattering 19
2.5 Discussion 20
2.5.1 Relevance to observations of P coda and Pdiff coda 20
2.5.2 Geodynamical interpretation 21
2.6 Conclusion 23

References 35

Chapter 3 On the frequency dependence and spatial coherence of PKP precursor amplitudes . . . 38
3.1 Introduction . . . 39
3.2 Methods I: Data stacking . . . 41
3.3 Methods II: Waveform modeling . . . 42
3.3.1 Random media models . . . 42
3.3.2 Phonon models . . . 43
3.4 Fitting the frequency dependence . . . 44
3.5 Lateral variations . . . 46
3.6 Array processing . . . 49
3.7 Discussion . . . 51
3.7.1 The nature of lower-mantle scatterers . . . 51
3.7.2 Future work . . . 53

References . . . 67

Chapter 4 Constraints on the heterogeneity spectrum of Earth's upper mantle . . . 71
4.1 Introduction . . . 72
4.2 Methods . . . 75
4.2.1 Characterizing scattered energy in data . . . 75
4.2.2 Modelling I – Monte Carlo method . . . 76
4.2.3 Modelling II - Spectral element simulations . . . 79
4.3 Results . . . 81
4.4 Discussion . . . 84
Appendices . . . 102
4.A Generating cubes of random media . . . 102
4.B Comparison with tomography . . . 103
4.B.1 Spherical spectra . . . 103
4.B.2 Power spectral density . . . 104
4.B.3 Direct comparisons between power-per-degree and power-spectral-density . . . 106
4.B.4 Proof . . . 107

References . . . 108

Chapter 5 Evidence for a reduced velocity gradient in the lowermost outer core from the range dependence of $PKKP$ precursor amplitudes 113
5.1 Introduction . . . 114
5.2 Methods . . . 115
5.2.1 Data stacking . . . 115
5.2.2 Waveform modeling . . . 116
5.3 Scattering throughout the Earth . . . 117

5.3.1 Inner-core scattering and $PKIJKP$ 117
5.3.2 Outer-core scattering 118
5.3.3 CMB topography 119
5.3.4 Lower-mantle scattering 119
5.3.5 Scattering near the Earth's surface 119
5.4 The validity of ray theory 120
5.5 Perturbing the outer-core velocity gradient 121
5.6 A plausible velocity model for the base of the outer core . 121
5.7 Discussion 123
5.8 Conclusion 124

References 129

Chapter 6 Conclusion 132
6.1 Summary of findings 132
6.2 Future research directions 133
6.2.1 Pdiff coda and $PKKP_x$ 133
6.2.2 Phase velocity spectra 134
6.2.3 Modeling heterogeneity spectra with geodynamics 135
6.3 Final remarks and outstanding challenges 136

References 138

LIST OF FIGURES

Figure 2.1: Top: Hammer projection showing source (blue circles) and receiver (red triangles) locations for waveforms analyzed in this study. Bottom: The green markers show approximate CMB entry-exit points. 25
Figure 2.2: Top: Data stack showing the time and range dependence of PKP precursors. The time series are sampled at 20 Hz and are stacked in 0.5° range bins. Times are relative to the $PKPdf$ onset... 26
Figure 2.3: Comparison of different weighting schemes used to elicit globally averaged precursor amplitudes. 27
Figure 2.4: Vertical cross-sections of the data stack with 95% confidence limits from bootstrap resampling. To enhance visibility of the precursors, the stacks are scaled up by a factor of five at negative times.... 28
Figure 2.5: Preferred model plotted against the 95% confidence intervals of the data stack. Precursors are enhanced by a factor of three. . . 29
Figure 2.6: A demonstration of how these data are able to constrain correlation length. Left: An exponential model with $a = 2$km and $\epsilon = 0.2\%$ underpredicts the precursor amplitude at high ranges. Right: An exponential model with $a = 18$km... 30
Figure 2.7: Synthetics generated by the seismic phonon algorithm plotted against our data stacks. The left column shows the *Hedlin et al.* (1997) preferred values of a and ϵ, whereas the right column shows the *Margerin and Nolet* (2003b) values.... 31
Figure 2.8: A comparison of a best-fitting whole-mantle scattering model with a best-fitting CMB scattering model.... 32
Figure 2.9: Two methods that account for strong scattering in the lithosphere. The leftmost column shows the uncorrected output of our preferred seismic phonon model. The center column shows the broadened amplitudes after convolution... 33
Figure 2.10: Seismic phonon predictions of preferred mantle scattering models from studies of Pdiff coda (left) and P coda (right). Convolution applied to correct for $PKPdf$ broadening. The precursors are enhanced... 34

Figure 3.1: PKP precursor stacks, showing globally-averaged amplitude as a function of time and epicentral distance for different frequency bands. White curves delineate onset times for scattered energy at various depths in the lower mantle.... 56

Figure 3.2: Synthetic PKP precursor amplitudes, as computed using the phonon algorithm for H-G random media with $\epsilon = 0.5\%$ and $a = 1000$ km. 57
Figure 3.3: Comparison of heterogeneity spectra proposed to model PKP precursors. The blue dotted line is the exponential model published by *Mancinelli and Shearer* (2013). The dashed curves indicate results from older studies... 58
Figure 3.4: Comparison between observed (thick black curves) and predicted PKP precursor amplitudes for three different types of random media. The dashed black lines mark the 95% confidence intervals for the data stacks. 59
Figure 3.5: Comparison between observed (thick black curves) and predicted PKP precursor amplitudes for a variety of H-G models. The dashed black lines mark the 95% confidence intervals for the data stacks. 60
Figure 3.6: Apparent lateral variations in PKP precursor amplitude. Measurements are grouped into 20° cells based on the CMB entry (upper map) or CMB exit (lower map) points for PKP_{df}. Each cell is subdivided into 8 azimuth bins... 61
Figure 3.7: A scatterplot of absolute difference in log-amplitude versus ray separation (gray dots). Due to the large number of points, we only plot every 500^{th} one. The median for the complete set of points is plotted in each bin (black circles).... 62
Figure 3.8: Stations used to locate the origin of PKP precursor energy from the M_{W} 7.6 30 September 2009 event in southern Sumatra.... . 63
Figure 3.9: (upper) Example seismogram recorded at station PFO filtered from 1–2 Hz. (center) Fourth-root vespagram assuming the theoretical backazimuth of 305° of the recording at the array in Figure 3.8.... 64
Figure 3.10: Fourth-root stacks in slowness azimuth space for 3-s windows around the earliest precursor (upper), the second precursor (center), and the PKP_{df} arrival (lower). 65
Figure 3.11: (upper) A record section of the PKP precursor waveforms filtered from 0.25–2.0 Hz. These have been aligned on the reference phase PKP_{df} which was subsequently removed. (center) Waveform alignment after the cross-correlation... 66

Figure 4.1: A comparison of recorded (black) and synthetic (red) seismograms for the 9 September 2010 Mw 6.2 earthquake near the coast of Central Chile. Synthetic seismograms were computed as part of the Global Shake Movie project... 89

Figure 4.2: Illustration of the smoothing procedure. This random heterogeneity model has strong small-scale heterogeneity in the upper mantle and weak large-scale heterogeneity in the lower mantle.... 90
Figure 4.3: Cross-section through an example 3D mantle model with random heterogeneity. The mantle is divided into two layers. The upper mantle—600 km thick— has stronger heterogeneity than the lower mantle.... 91
Figure 4.4: SEM model setup. 26,484 receivers are located in the gray region (50-130° range) at $\sim 1°$ spacing. The source is placed at the intersection of the equator and the prime meridian, at a depth of 20 km. 92
Figure 4.5: A comparison between the phonon and SEM methods for P-coda. The SEM synthetics were computed for a thrust source. They were filtered from 20–40s before stacking. The phonon code was run at 30s.... 92
Figure 4.6: Time and range dependence of P-coda filtered from 5–10s (upper-left), 10–20s (upper-right), 20–40s (lower-left), and 30–60s (lower-right). Data are plotted in gray; 95% confidence bounds obtained by regional bootstrapping are shown... 93
Figure 4.7: Fits of our preferred model (dashed red) to the 1-Hz data stacks published by Shearer and Earle, 2004. Phonon code run at 1s. 95
Figure 4.8: The preferred heterogeneity spectrum based on fits to scattering observations and tomography results. Two alternate spectra are plotted that fit the scattering observations almost as well. Bounds for the preferred spectrum are shown... 96
Figure 4.9: Lateral variations in P-coda amplitude when filtered from 10–20s. Data are grouped based on their ray endpoints (both source- and receiver-side). For each populated "bin" we show the associated source cell and receiver cell... 97
Figure 4.10: Random realizations of two-phase mixtures of basalt (dark green) and harzburgite (light green). The mixtures are self-similar so any linear length-scale may be applied to the axes. 98
Figure 4.11: Predicted spectra for a marble-cake mixture of basalt and harzburgite. The net power of the spectrum is affected by changing the basalt fraction of the mixture. These models assume mixing occurs primarily at wavelengths... 99
Figure 4.12: Tradeoffs between the thickness of the scattering layer and the required rms velocity perturbations. The thinnest layer tested (denoted by a red x) did not fit the data as well as the thicker layers.... 100

Figure 5.1: Spatial distribution of the $PKKP$ dataset used in this study.... 125

Figure 5.2: Globally-averaged $PKKP$ precursor stacks (black); the standard error of the mean is shown by gray shading. The red curves represent phonon code predictions for scattering (left) in the uppermost 200 km of the mantle... 126
Figure 5.3: **(A)** Ray-theoretical travel times of the $PKKP$ triplication for velocity model *iasp*91. **(B)** Comparison between ray-theoretical and 1-Hz reflectivity amplitudes for $PKKP_{bc}$.... 127
Figure 5.4: **(A)** One-dimensional reference models of the lowermost outer-core. The initial model we use is *iasp*91 (*Kennett and Engdahl*, 1991); models *ak*135 (*Kennett et al.*, 1995) and PREM (*Dziewonski and Anderson*, 1981) are plotted... 128

LIST OF TABLES

Table 4.1: Mean-free-paths (in km) for P energy (l_P) and S energy (l_S) for the preferred heterogeneity model. The superscript t denotes the transport mean-free-path. 101

ACKNOWLEDGEMENTS

I would like to start by thanking my advisor, Peter Shearer. Without his guidance over that past four and a half years, virtually none of the work presented in this thesis would have been possible. I entered the Ph. D. program at Scripps with little formal training in geophysics, so Peter basically taught me how to do publication-worthy seismology research from scratch. It has been a great pleasure to work under his guidance, and I have learned a tremendous amount about practicing science due to his constant, thoughtful mentorship. The most important lesson I learned from Peter's example can be summed up by the following words from physicist Richard Feynman, "If you have a theory, you must try to explain what's good and what's bad about it equally. In science, you learn a kind of standard integrity and honesty." I would also like to thank him for sending me abroad to Germany, Austria, and Japan in order to visit collaborators and to attend the EGU and SEDI conferences, and for encouraging me to attend numerous conferences and workshops within the United States.

Next, I would like to thank the members of my thesis committee for their advice throughout the years. Thanks to Peter Gerstoft for his keen eye, especially regarding the technical aspects of my thesis. I enjoyed our weeknight track workouts—these really helped to improve my half-marathon time! I'd like to thank Guy Masters for educating me on all matters regarding long-period seismology, and for conversations on thermal versus compositional heterogeneity within the mantle. Thank you to Benson Shing for his timely responses to all my emails and for always making time to meet with me. Thanks to Dave Stegman for his mentorship over the years, for his genuine interest in the welfare of the geophysics students, and for the many conversations we had about compositional stirring in the mantle.

I would like to thank my other coauthors, Tine Thomas and Qinya Liu, who contributed to the science presented in Chapters 3 and 4. Tine invited me to visit her research group in Münster (twice!), where she taught me all about array processing and introduced me to possibly my favorite German food, currywurst. I am grateful for her many detailed suggestions that significantly improved the quality of Chapter 3. Although nearly all of my interactions with Qinya were

through email exchanges, I found her to be a wonderful and pleasant collaborator. Her expertise regarding the spectral element method was instrumental to the long-period scattering research presented in Chapter 4.

Thank you to Dave Stegman, Kerry Key, and Lynn Russell for hiring me to be a TA for their undergraduate classes. I appreciate having had the regular opportunity to develop my teaching skills by leading discussion sections and developing problem sets. Although I wasn't an official TA for Kevin Brown's structural geology class, I'd like to thank him for trusting me to drive a mini-van full of undergraduates during one of his weekend field trips. His trust ultimately turned out to be misguided, however, as I managed to "run into the only bloody boulder in Death Valley." Thankfully nobody was hurt, or had to be left behind in the desert.

Thanks to those who provided fieldwork opportunities to students such as myself who take for granted the fact that data actually needs to be collected in order for science to happen. In particular, thank you to Eric Lindsey, Yuri Fialko, and Kang Wang for taking me on their GPS field trips. Thanks to Frank Vernon and his lab for including me in the Nodal array deployment at Sage Brush Flat. Thanks to Adrian Doran, Gabi Laske, and the OBS lab for inviting me to participate in the Patton Seismicity Research Cruise aboard the R/V Robert Gordon Sproul.

Thanks to the students and postdocs that have made studying at Scripps so much fun. I am grateful to have found friends in the diversely talented geophysics cohort of which I was part: Maggie, Shi, Wenyuan, Peter, Kang, Lauren, Qian, and Kyle. I appreciate the kind support and advice from other seismology students and postdocs with whom I overlapped, including Wei, Adrian, Daniel, Janine, Xiaowei, Marine, Zhongwen, Qiong, and Robin. I'd like to thank Zhitu for his regular curiosity regarding my work, and I look forward to continued conversations and collaborations with him at Brown. Thank you to my office-mate Kang for his patience regrading my incessant stream of trivial questions about the workings of GMT and UNIX; and office-mate Erica for her help with LaTeX formatting issues, and for giving other helpful tidbits of advice throughout the years. Thanks to Soli

who was my reliable surfing buddy for many years, and who is quite possibly the best GP student rep ever elected in the history of IGPP. I'd also like to acknowledge my non-geophysicist friends: Sean, Eiren, Julia, Max, and Jess, whose support kept me sane during the final months leading up to my defense. Without the help of these friends (and many more who remain unnamed!) it would not have been possible to weather the most difficult parts of the Ph. D. experience.

Last, and certainly not least, I am thankful for the support of Caitlin, my now-fiancée, who has been with me since the days before I had even received my letter of acceptance from Scripps back in 2011. I am deeply grateful for the sacrifices she has made to join me here in San Diego during the final year of my Ph. D., and for her encouragement to pursue the postdoc opportunity at Brown. I have also been blessed to be part of a large and involved Italian–American family composed of parents, grandparents, aunts, uncles, cousins, great aunts and uncles, second cousins, friends of the family, families of friends, and, now, future in-laws! I would like to thank all of them for their support throughout the years, and to my parents, Joseph and Lillian, for pushing me from a young age to work hard towards academic success, and for sending me to the best schools that they could. In recent years, my brother Michael has developed an annoying tendency to over-achieve. Three Ivy League football championships plus a degree from Harvard are a few of his recent accomplishments. Despite being four years younger, he even managed to land a "real job" before me. So here is my attempt to keep up, Michael. A Ph. D. thesis. Sibling rivalries aside, my brother has been extremely understanding of the challenges faced by students in academia, and for that I am grateful.

Chapter 2, in full, is a reformatted version of the material as it appears in Geophysical Journal International: Mancinelli, N. J., and P. M. Shearer, Reconciling discrepancies among estimates of small-scale mantle heterogeneity from PKP precursors, Geophys. J. Int., 195, 1721-1729, doi: 10.1093/gji/ggt319, 2013. I was the primary investigator and author of this paper.

Chapter 3, in full, has been submitted for publication of the material as it may appear in Journal of Geophysical Research – Solid Earth: Mancinelli, N. J., P. M. Shearer, and C. Thomas, On the frequency dependence and spatial coherence

of PKP precursors. I was the primary investigator and author of this paper.

Chapter 4, in full, has been submitted for publication of the material as it may appear in Journal of Geophysical Research – Solid Earth: Mancinelli, N. J., P. M. Shearer, and Q. Liu, Contraints on the heterogeneity spectrum of the upper mantle. I was the primary investigator and author of this paper.

Chapter 5, in full, has been submitted for publication of the material as it may appear in Geophysical Research Letters: Mancinelli, N. J., and P. M. Shearer, Evidence for a reduced velocity gradient in the lowermost outer core from the range dependence of $PKKP$ precursor amplitudes. I was the primary investigator and author of this paper.

VITA

2011	B. S. in Physics, University of Notre Dame
2013	M. S. in Earth Sciences, University of California, San Diego
2016	Ph. D. in Earth Sciences, University of California, San Diego

PUBLICATIONS

Mancinelli, N. J., and P. M. Shearer, Evidence for a reduced velocity gradient in the lowermost outer core from the range dependence of $PKKP$ precursor amplitudes, *Geophys. Res. Lett.*, submitted.

Mancinelli, N. J., P. M. Shearer, and C. Thomas, On the frequency dependence and spatial coherence of PKP precursor amplitudes, *J. Geophys. Res.*, submitted.

Mancinelli, N. J., P. M. Shearer, and Q. Liu, Constraints on the heterogeneity spectrum of Earth's upper mantle, *J. Geophys. Res.*, submitted.

Ma, Z., G. Masters, and N. Mancinelli, Two-dimensional global Rayleigh wave attenuation model by accounting for finite-frequency focusing and defocusing effect, *Geophys. J. Int.*, *204*(1), 631–649, doi:10.1093/gji/ggv480, 2015.

Mancinelli, N. J. and P. M. Shearer, Reconciling discrepancies among estimates of small-scale mantle heterogeneity from PKP precursors, *Geophys. J. Int.*, *195*(3), 1721–1729, doi:10.1093/gji/ggt319, 2013.

ABSTRACT OF THE DISSERTATION

Constraints on Heterogeneity throughout the Earth's Mantle from Observations of Scattered Seismic Waves

by

Nicholas John Mancinelli

Doctor of Philosophy in Earth Sciences

University of California, San Diego, 2016

Professor Peter M. Shearer, Chair

We place constraints on the amounts and length scales of seismic velocity variations throughout the mantle that are beyond the resolving capabilities of seismic tomography. We model global stacks of various seismic phases that are thought to have a scattering origin, using a Monte Carlo phonon method.

In Chapter 2, we forward model stacks of over 10,000 high-frequency ($\sim$1 Hz) PKP precursor waveforms by distributing velocity perturbations of $\sim$0.1% throughout the lowermost mantle, resolving a debate between older studies. We confirm that models where scattering is distributed uniformly throughout the lowermost mantle better match the observations than those where scattering is restricted to a thin region just above the core–mantle boundary.

In Chapter 3, we characterize the frequency dependence of PKP precursors at central frequencies ranging from 0.5 to 4 Hz. At greater frequencies, we observe more scattered energy, particularly at shorter ranges. We model this observation by invoking heterogeneity at length scales from 2 to 30 km. Amplitudes at 0.5 Hz, in particular, suggest the presence of more heterogeneity at scales >8 km than present in previously published models.

In Chapter 4, we constrain the heterogeneity spectrum of Earth's upper mantle at scales from a few kilometers to tens-of-thousands of kilometers using observations from high-frequency scattering, long-period scattering, and tomography. We explore geodynamically plausible scenarios that might be responsible for the rms and fall-off rate of the proposed spectrum, including a self-similar mixture of basalt and harzburgite.

In Chapter 5, we stack a large global dataset of 1-Hz $PKKP$ waveforms to constrain globally-averaged properties of $PKKP$ precursors. We propose a new 1-D reference model that fits both our $PKKP$ precursor amplitudes and constraints on absolute PKP_{bc} travel times. Our globally averaged $PKKP$ precursor observations are consistent with random CMB topography with rms variations of $\sim$440 m and a horizontal correlation length of $\sim$7 km.

Finally, in Chapter 6, we discuss outstanding challenges and future prospects for deep Earth scattering research.

Chapter 1

Introduction

1.1 Earth structure: Length scales and dimensions

Much of what is known about deep Earth structure relies upon observations of seismic waves that have traveled long distances from their source. At periods longer than 1 second, most teleseismic body-wave energy arrives as the so-called deterministic phases: P, S, PP, PcP, PKP, PKS, and so on. To first order, the travel times of these phases can be explained by models of seismic velocity that vary only with depth. Perhaps the most striking feature of these 1-D models is the division of the Earth into three main layers: the solid mantle, the liquid outer-core, and the solid inner-core.

The travel times for phases with specific source–receiver geometries often vary systematically with respect to the 1-D model prediction, suggesting the presence of three-dimensional (3-D) variations in seismic velocity. The exercise of mapping 3-D changes in seismic properties—called *seismic tomography*—has resulted in a set of 3-D global models that generally agree on the amplitude and location of large-scale structure. Global-scale differences in seismic velocity are thought to indicate thermal variations throughout the mantle. Most tomography models place features in the upper mantle that are strongly correlated with surface tectonics, including 'warm' low-velocity regions beneath spreading centers and

'cool' high-velocity regions beneath continental cratons. In the lower mantle, tomography models reveal two antipodal zones of reduced shear-velocity, which may represent hot, dense piles of primordial material.

Most current generation tomography models are well correlated out to spherical harmonic degree 16, at least in the uppermost mantle. This suggests that only structures larger than ∼2400 km are reliably mapped. The lack of correlation among competing tomography models at smaller scales likely stems from differences in data selection and the theories applied, but virtually all of the 3-D models are artificially smooth because of the regularization required to stabilize geophysical inverse problems. An additional limitation in resolving small-scale structure is imposed by the physics of wave propagation, as long-period waves tend to respond to material properties that are averaged over sub-wavelength variations.

The focus of this thesis concerns deep Earth structure beyond the resolving capabilities of seismic tomography. Whereas mapping the amplitude and location of all small-scale structure within the Earth is currently beyond reach, quantifying the amount (i.e., rms amplitude) of 3-D structure within the mantle as a function of length-scale is a more tractable problem. Such constraints are valuable to the broader community because they may provide compelling evidence for the presence of compositional heterogeneity throughout the mantle, as small-scale thermal anomalies are not likely to persist over geologic timescales. These constraints may also provide insight to the nature of mantle convection, as different modes of fluid mixing are thought to produce distinct signatures in the heterogeneity spectrum.

1.2 Scattering observations

Standard 1-D models of seismic velocity fail to predict the portion of seismic energy that is observed to arrive between the main phases, most notably at short periods. A typical high-pass-filtered seismogram, for example, shows an impulsive P-wave arrival followed by a decaying high-frequency wavetrain (termed P-coda). *Aki and Chouet* (1975) proposed that small-scale three-dimensional (3-D) perturbations in seismic velocity scatter energy away from the direct wave,

thereby causing the later high-frequency arrivals.

Scattered arrivals are, in general, incoherent from station to station, so stacking amplitudes (i.e., envelope functions) is more effective than stacking waveforms. In practice, seismic amplitudes are challenging to interpret because observations are highly variable from station to station. This is due to a variety of 3-D wave-propagation effects including geometrical spreading, focusing/defocusing, reflection and transmission at interfaces, and attenuation (both intrinsic and scattering).

We make robust globally-averaged amplitude estimates by stacking hundreds, thousands, or even tens-of-thousands of envelope functions without regard to specific source or receiver positions. This approach sacrifices spatial resolution but improves measurements of average scattered energy relative to direct energy. For most of the studies presented in this thesis, we constrain the globally-averaged scattering parameters (i.e., the magnitude and scale-length of small-scale fluctuations in density and velocity) by forward modeling the observations.

In situations where the spacing of seismic stations is small compared to the seismic wavelength, it may be possible to observe coherent scattered arrivals. Methods such as beamforming that stack array records to resolve the direction of the incoming wavefront may be used to constrain the positions of individual scatterers.

1.3 Random media theory

Deterministic mapping of small-scale structure is currently beyond reach. A more manageable problem is to characterize a medium by its statistical properties. In other words, how strong is the heterogeneity and how is this strength distributed across different scale lengths? Random media theory, extensively reviewed in *Sato and Fehler* (1998), provides the quantitative framework to address these questions.

We can decompose a three-dimensionally varying wave velocity V into a sum of the mean velocity V_0 and the perturbation δV:

$$V(\mathbf{r}) = V_0 + \delta V(\mathbf{r}) = V_0 \left[1 + \xi(\mathbf{r})\right] \tag{1.1}$$

where $\mathbf{r}$ is the position vector and $\xi(\mathbf{r})$ is the fractional fluctuation of wave velocity. The 3-D autocorrelation function (ACF) is an ensemble average

$$R(\mathbf{x}, \mathbf{y}) = \langle \xi(\mathbf{y}) \xi(\mathbf{y} + \mathbf{x}) \rangle. \tag{1.2}$$

If we make the assumption of stationarity, the ACF only depends on the lag-distance vector $\mathbf{x}$, and hence the statistical properties of a random medium are completely defined by $R(\mathbf{x})$. Equivalently, the 3-D power-spectral-density function (PSDF or $P(\mathbf{m})$, where $\mathbf{m}$ is the angular wavenumber vector) can be used to specify the statistics of the random medium. These two functions are related by 3-D Fourier transform:

$$P(\mathbf{m}) = \iiint_{-\infty}^{\infty} R(\mathbf{x}) e^{-i\mathbf{m}\cdot\mathbf{x}} \, d\mathbf{x}. \tag{1.3}$$

In the studies presented in this thesis, we assume that the heterogeneity is isotropic, so these functions exhibit spherical symmetry ($r = ||\mathbf{x}||$ and $m = ||\mathbf{m}||$). $P(m)$ is often referred to as the *heterogeneity spectrum*.

1.4 Modeling scattered energy with seismic particles

The Monte Carlo phonon algorithm developed by *Shearer and Earle* (2004) provides a powerful means to model the global scattered wavefield. Previous algorithms generally focused on modeling isolated phases by summing scattering contributions from volume elements distributed throughout the Earth, which involved independent calculations of geometrical spreading, reflection/transmission effects at discontinuities, and intrinsic attenuation. Such algorithms could easily grow to become quite complex, and—as will be discussed in Chapter 2—are prone to coding errors.

The Monte Carlo phonon algorithm takes an approach that is much simpler: it treats the seismic energy field as a sum of discrete particle that travel along ray theoretical trajectories and experience random scattering events from probabilities derived from the heterogeneity spectrum of the medium. This method

- naturally accounts for geometrical spreading effects;
- naturally accounts for scattering attenuation and thus conserves energy;
- includes intrinsic attenuation (energy lost to heat or crystal dislocation);
- includes reflection/transmission effects at discontinuites;
- handles both weak (single) and strong (multiple) scattering;
- and handles wave polarizations and conversions between P and S.

A main advantage of this approach is that the full seismic energy field (the direct phases included) is simultaneously computed in an energy-conserving framework. This facilitates the researcher's ability to evaluate how several phases are at once affected by an arbitrary heterogeneity model. This advantage will become increasingly important as researchers begin to converge on a single heterogeneity model that simultaneously explains observations of the many scattered phases.

The phonon approach is most defensible when used to model scattering at periods shorter than $\sim$1 s, where the ray-theoretical basis of this code is expected to be valid. In Chapter 4, however, we attempt to model long-period scattering with the phonon code by broadening the output through an extra convolution with the filter wavelet. Advances in computing power over the last decade have made it possible to run spectral-element simulations of global wave propagation for Earth models with arbitrary 3-D complexity. In particular, the SPECFEM3D_GLOBE (SEM, for short) software package (*Komatitsch et al.*, 2002) is capable of generating synthetic seismograms that are accurate to 20 seconds or shorter, provided that one has access to sufficient computing power. Using the Stampede supercomputer to generate SEM synthetics for specific realizations of random media, we are able to verify the accuracy of the Monte Carlo phonon algorithm at periods longer than 20 s.

1.5 Thesis overview

Chapters 2, 3, 4, and 5 of this thesis were originally written to be self-contained articles suitable for individual publication. Although they were initially written to be read in isolation, the main chapters are closely related to one another in theme.

In Chapter 2, we analyze PKP precursors—a scattered phase that has unique sensitivity to lower mantle structure—to place constraints on small-scale heterogeneity throughout the lowermost mantle. The main focus of this study is to resolve the order-of-magnitude disagreement between *Hedlin et al.* (1997) and *Margerin and Nolet* (2003). The former study proposed that rms perturbations throughout the lower mantle ought to be on the order of 1% to generate the observed quantity of scattered energy, whereas the latter found that rms perturbations of 0.1% are sufficient.

Chapter 3 details our exploration of the frequency dependence and spatial coherence of PKP precursor amplitudes. We find that the frequency dependence suggests a broader spectrum of scale lengths than previously proposed. Low-frequency precursors, in particular, suggest an increased amount of structure larger than ∼8 km in size. We also observe that PKP precursor amplitudes display large-scale lateral variations, in agreement with an earlier study by *Hedlin and Shearer* (2000). Finally, we use array methods (e.g., *Rost and Thomas*, 2002) on groups of stations which may be able to resolve the source–receiver ambiguity on a global scale.

In Chapter 4, we measure and model scattered amplitudes at periods longer than 1 Hz to constrain the broad spectrum of heterogeneity within the upper mantle. We find significant amounts of heterogeneity at scales from 5–500 km, and we propose a single spectrum that matches constraints from (1) long-period scattering observations, (2) high-frequency scattering observations, and (3) long-wavelength constraints from tomography models. We propose that the observed ∼1/wavenumber spectral falloff at small-scales may be due to a marble-cake mixture of basalt and harzburgite (*Batchelor*, 1959; *Antonsen and Ott*, 1991; *Agranier et al.*, 2005; *Ricard et al.*, 2014).

In Chapter 5, we constrain short-wavelength topography on the core–mantle boundary from observations of $PKKP$ precursors, improving upon an earlier study by *Earle and Shearer* (1998). We implement scattering due to a rough surface into the phonon code framework by computing scattering probabilities from a mathematical theory derived by *Bataille and Flatté* (1988). An interesting finding is that widely-used 1-D velocity models fail to produce the observed range dependence of the $PKKP$ precursor amplitudes. We propose a new 1-D velocity model that gives better fits the $PKKP$ precursor observations, while also matching PKP_{bc} travel-time constraints from *Souriau* (2015).

Finally, in Chapter 6, we briefly summarize the main findings presented in this thesis and discuss future research plans.

References

Agranier, A., J. Blichert-Toft, D. Graham, V. Debaille, P. Schiano, and F. Albarède (2005), The spectra of isotopic heterogeneities along the mid-Atlantic Ridge, *Earth and Planetary Science Letters*, *238*, 96–109, doi:10.1016/j.epsl.2005.07.011.

Aki, K., and B. Chouet (1975), Origin of coda waves: Source, attenuation, and scattering effects, *Journal of Geophysical Research*, *80*(23), 3322—-3342, doi:10.1029/JB080i023p03322.

Antonsen, T. M., and E. Ott (1991), Multifractal power spectra of passive scalars convected by chaotic fluid flows, *Physical Review A*, *44*(2).

Bataille, K., and S. M. Flatté (1988), Inhomogeneities near the core–mantle boundary inferred from scattered PKP waves recorded at the Global Digital Seismograph Network, *Journal of Geophysical Research*, *93*(B12), 15,057–15,064, doi:10.1029/JB093iB12p15057.

Batchelor, G. K. (1959), Small-scale variation of convected quantities like temperature in turbulent fluid: Part 1. General discussion and the case of small conductivity, *Journal of Fluid Mechanics*, *5*(01), 113–133, doi:10.1017/S002211205900009X.

Earle, P. S., and P. M. Shearer (1998), Observations of high-frequency scattered energy assocated with the core phase $PKKP$, *Geophysical Research Letters*, *25*(3), 405–408.

Hedlin, M. A. H., and P. M. Shearer (2000), An analysis of large-scale variations in small-scale mantle heterogeneity using Global Seismographic Network recordings of precursors to PKP, *Journal of Geophysical Research*, *105*(B6), 13,655.

Hedlin, M. A. H., P. M. Shearer, and P. S. Earle (1997), Seismic evidence for small-scale heterogeneity throughout the Earth's mantle, *Nature*, *387*(6629), 145–150, doi:10.1038/387145a0.

Komatitsch, D., J. Ritsema, and J. Tromp (2002), The spectral-element method, Beowulf computing, and global seismology, *Science*, *298*(5599), 1737–1742, doi:10.1126/science.1076024.

Mancinelli, N. J., and P. M. Shearer (2013), Reconciling discrepancies among estimates of small-scale mantle heterogeneity from PKP precursors, *Geophysical Journal International*, *195*(3), 1721–1729, doi:10.1093/gji/ggt319.

Margerin, L., and G. Nolet (2003), Multiple scattering of high-frequency seismic waves in the deep Earth: PKP precursor analysis and inversion for mantle granularity, *Journal of Geophysical Research*, *108*(B11), 2514.

Ricard, Y., S. Durand, J.-P. Montagner, and F. Chambat (2014), Is there seismic attenuation in the mantle?, *Earth and Planetary Science Letters*, *388*(0), 257–264, doi:http://dx.doi.org/10.1016/j.epsl.2013.12.008.

Rost, S., and C. Thomas (2002), Array seismology: methods and applications, *Reviews of Geophysics*, *40*(3), 1–2.

Sato, H., and M. C. Fehler (1998), *Seismic Wave Propagation and Scattering in the Heterogeneous Earth*, Springer.

Shearer, P. M., and P. S. Earle (2004), The global short-period wavefield modelled with a Monte Carlo seismic phonon method, *Geophysical Journal International*, *158*(3), 1103–1117, doi:10.1111/j.1365-246X.2004.02378.x.

Souriau, A. (2015), Presumption of large-scale heterogeneity at the top of the outer core basal layer, *Earth and Planetary Science Letters*, *415*, 175–182, doi: 10.1016/j.epsl.2015.01.024.

Chapter 2

Reconciling discrepancies among estimates of small-scale mantle heterogeneity from PKP precursors

Abstract

We stack amplitudes of over 10,000 high-frequency (∼1 Hz) PKP precursor waveforms, amassed from broadband global seismic data with source-receiver distances between 120° and 145° recorded from 1990–2012. We forward model the stacked precursor envelope with an energy-conserving, multiple-scattering algorithm to find that an r.m.s. velocity perturbation of ∼0.1% fits the data reasonably well, in agreement with *Margerin and Nolet* (2003b). Similar results can be obtained using single-scattering (Born) theory, given the relatively weak scattering produced by our preferred model. The ramp-like increase in PKP precursor amplitudes with time is best fit with whole mantle scattering rather than models where scattering is restricted to the core-mantle boundary. Correctly modeling the relative amplitude of PKP precursor amplitudes compared to $PKPdf$ requires taking into account the pulse broadening and coda of $PKPdf$, which can be done

either empirically or by including a strongly scattering lithospheric layer in the multiple-scattering code. Several mantle scattering models proposed to explain other scattered seismic phases predict PKP precursor amplitudes much larger than those observed.

2.1 Introduction

Seismic scattering by small-scale heterogeneities in Earth's lowermost mantle causes short-period energy to arrive before the core phase PKP (*Cleary and Haddon*, 1972). The strength and depth extent of such heterogeneity, however, still remains a subject of debate. *Doornbos and Vlaar* (1973) originally argued for volumetric scatterers distributed 900 km above the core-mantle boundary (CMB), but *Haddon and Cleary* (1974) preferred to restrict the heterogeneity to a 200-km-thick layer above the CMB. Later, *Doornbos* (1978) used perturbation theory to show that topography on the CMB could describe the precursor amplitudes and onset times. Discrepancies among these early studies are difficult to reconcile because of possible selection biases on the then limited number of available seismograms. (See *Shearer* (2007) for more a more detailed history of this subject.)

Two more recent analyses of PKP precursors, *Hedlin et al.* (1997) and *Margerin and Nolet* (2003b), used global stacking techniques to elicit the time and range dependence of the precursor amplitudes. These two studies agreed that small-scale ($\sim$10 km) heterogeneity distributed throughout the mantle explains the time dependence of observed PKP precursor amplitudes better than models where scattering is restricted to the D$''$ region. *Margerin and Nolet* (2003b), however, contested the 1% r.m.s. velocity perturbation originally proposed by *Hedlin et al.* (1997) to explain the strength of the precursors, arguing instead for a much weaker value between 0.1% and 0.2%.

The reason for the discrepancy between the two studies has remained unclear, including whether it reflects different data processing choices or differences in theoretical modeling of the scattering. *Hedlin et al.* (1997) employed a single-scattering theory (e.g., *Chernov*, 1960) to sum Born scattering kernels for various

mantle depth layers while *Margerin and Nolet* (2003b) used a multiple-scattering approach. However, for the 0.1% velocity perturbation proposed by *Margerin and Nolet* (2003b), the scattering should be relatively weak, so there should not be a large difference between single and multiple scattering theories.

To resolve this disagreement, we perform a similar but independent analysis on a much larger dataset of PKP precursors, modeling their stacked amplitudes using a Monte Carlo seismic phonon algorithm (e.g., *Shearer and Earle* 2004, 2008; *Peng et al.* 2008) which conserves energy and allows for multiple scattering. Our best-fitting model agrees with *Margerin and Nolet* (2003b), yet we also find that a single-scattering approximation achieves similar results. We confirm that PKP observations favor whole mantle scattering rather than scattering from just the CMB or the D″ layer and show how strong scattering in the lithosphere can roughly explain observed $PKPdf$ waveform broadening. Observed PKP precursor amplitudes provide strong constraints on lower mantle scattering strength, and we show how two models proposed to explain other high-frequency scattered phases predict PKP precursor amplitudes much higher than those observed. Finally we discuss the implications of these results for whole-Earth scattering profiles and geodynamic and geochemical models.

2.2 Data selection and stacking

Since *Margerin and Nolet* (2003b), the amount of global seismic data has increased enormously. Using the Standing Order for Data (*Owens et al.*, 2004) to download data from the Incorporated Research Institutions for Seismology (IRIS), we obtained more than 150,000 broadband PKP waveforms recorded at epicentral distances between 120° and 145° with Mw $\geq$ 5.7 for shallow events (depth $<$ 50 km) and with Mw $\geq$ 5.5 for deeper events. Figure 2.1 shows the source-receiver distribution of the data used, as well as their associated CMB entry-exit points where the earliest-arriving precursor energy is likely to be scattered.

Prior to stacking, we bandpass filter the traces from 0.7–2.5 Hz and align them on their $PKPdf$ arrival times as calculated from PREM (*Dziewonski and*

Anderson, 1981). After alignment, we reject traces that exhibit low signal-to-noise ratios. Next, we compute the envelope function for each trace and subtract the average pre-event noise power. Because the energy arriving 0 to 20 s before the main arrival is of primary interest, we define the pre-event window to be 20 s to 60 s before $PKPdf$. Finally, we normalize each trace by the maximum amplitude arriving between 0 s and 5 s (i.e., the PKP arrival) and sum them in 0.5-degree range bins. Roughly 1000 seismograms contribute to the final stack in each range bin. Figure 2.2 shows the time and range dependence of the precursor amplitudes, with the white curves showing ray-theoretical scattering onset times as a function of scattering depth.

Although Figure 2.2 is a pleasing image, it may not accurately represent globally averaged PKP precursor behavior. As Figure 2.1 makes clear, the source and receiver distribution is very non-uniform and previous studies have suggested that there exist considerable 3-D variations in heterogeneity strength. *Vidale and Hedlin* (1998), for instance, found exceptionally strong scattering near the CMB beneath the Pacific Ocean north of Tonga. *Hedlin and Shearer* (2000) identified strongly scattering areas beneath central Africa, parts of North America, and north of India. *Margerin and Nolet* (2003b) constructed sub-stacks based on region and observed stronger-than-average stacked envelopes for the Tonga-Eurasia corridor. Using short-period PcP reflections, *Rost and Thomas* (2010) found a P-wave reflector at 110 km above the CMB beneath the Kenai peninsula.

To reduce the possible biasing effects of the non-uniform station coverage, including the high concentration of stations in the United States and Europe, we apply a weighting scheme that emphasizes data from poorly sampled regions of the lower mantle. For an individual trace recorded at location (θ,ϕ), we count the total number of traces, N, within a certain angular distance, Δ, from (θ,ϕ). During the stacking procedure, we then weight each trace by $1/N$, so that receiver-sparse areas influence the final stack as much as receiver-dense areas. As shown in Figure 2.3, we experiment with different Δ values to find that the main features of the precursor envelope remain largely unaffected by the weighting. This strengthens the notion that PKP precursors are a global feature, despite some degree of lateral

variability. For higher choices of Δ, the stacked precursor envelope becomes less smooth. We attribute this behavior to the strong down-weighting of most traces in the stack, excepting those few with rare source-receiver paths. Upon stacking, these rare traces are insufficient in number to form a smooth envelope.

In addition to reducing bias due to non-uniform data coverage, we would like to estimate error bars for the PKP precursor amplitudes, which ideally should include the effects of our limited data coverage rather than just variability in the raw dataset. Thus, instead of treating each trace as an independent measurement, we construct multiple sub-stacks that group similar ray geometries and treat these as statistically independent measurements. More specifically, we divide Earth's surface into twelve equal-area cells and group traces that have traversed along similar corridors through the Earth. Because we group traces based on both source and receiver location, there are 144 possible combinations. However, only about thirty of these groups are populated because source-receiver distances for PKP precursors are limited to between 120° and 145°. To compute error bars, we apply a bootstrap resampling algorithm that repeatedly averages random combinations of these 30 populated groups. The resulting 95% confidence intervals are shown in Figure 2.4.

Although our dataset is much larger than those used in previous studies, our stacked PKP precursor amplitudes are quite similar. With increasing time, the observed envelope emerges rather slowly after the ray theoretical onset (plotted in Figure 2.4). Since the main phase ramps-up in a similarly gradual way, this behavior may result from waveform broadening effects caused by strong heterogeneity in the lithosphere. With increasing range, a robust precursor signal emerges from the noise at about 125° and increases gradually until 143°, where geometrical focusing near the b-caustic makes interpretation difficult.

We explored alternatives to the alignment strategy described above. Since PREM is a one-dimensional Earth model, we do not expect all of the traces to line up perfectly with the PREM predicted travel time curve. Large-scale lateral heterogeneity results in a travel time spread of about ±1s, thereby limiting the time resolution of the data stack. Attempts to align the traces with an autopicking

algorithm or a maximum amplitude criterion were abandoned since they did not produce appreciatively clearer results and in some cases produced artifacts.

Our stacks agree with previous studies, so it is very unlikely that the factor-of-ten discrepancy between *Hedlin et al.* (1997) and *Margerin and Nolet* (2003b) arises from data selection biases or from subtleties in their stacking procedures. In the next section, we explore the possibility that the disagreement arises from differences in modeling assumptions.

2.3 Seismic phonon models

We use the Monte Carlo seismic phonon method described by *Shearer and Earle* (2004) to forward model the PKP precursor amplitudes. Though the details of numerical implemetation differ, this algorithm is similar to the one developed in *Margerin and Nolet* (2003a). In brief, the method tracks individual energy particles sprayed from a seismic source located at the surface as they travel along trajectories from a large table of precomputed ray paths. Upon entering a scattering volume, a random path length is assigned to the particle. Once the particle exceeds that path length, a scattering event occurs and a random new direction and path length are assigned. When the particle returns to the surface, it is summed in an appropriate time-range bin. The method is designed such that, when the number of summed particles becomes large, the distribution of path lengths is exponential with mean value l (since the probability of scattering along the ray path is constant) and the distribution of scattering angles matches the basic scattering patterns given by *Sato and Fehler* (1998).

This method obeys energy conservation, allows for multiple scattering, and naturally accounts for geometrical spreading and out-of-plane scattering effects. For computational efficiency, we initially consider P-to-P scattering only and restrict the seismic source to spray particles only along ray parameters, p, between 0 and 0.116 s/km. In the following section, we will discuss how additional scattering (P-to-S and S-to-P) in the lithosphere may help describe the slow decay of PKP coda.

We divide the mantle into three concentric scattering volumes, each described by a mean-free path, l. The heterogeneity power spectrum in each volume is modeled with an exponential autocorrelation function (see *Sato and Fehler* 1998), parameterized by r.m.s. velocity perturbation, ϵ, and correlation length, a. The models assume a velocity-density scaling factor, ν, of 0.8 to be consistent with previous studies. This parameter controls the amount of backscattering and should not significantly affect our results since PKP precursors are generated by near-forward scattering . To be certain that this is the case, we rerun our calculations with $\nu = 0$, i.e. with no density perturbations, and find that the synthetics are unaffected. Presumably the choice of ν would be more relevant in the modeling of phases such as $PKKP$ where backscattering is dominant. We determine the wavenumber from 1.3 Hz, the dominant frequency of the data, and the mean background velocity of each volume. The precomputed raypaths are based on a modified version of IASP91 (*Kennett and Engdahl*, 1991) where the sharp corner in the velocity profile at 2740 km depth is slightly smoothed.

The relatively weak scattering we assume for the lower mantle does not produce much pulse broadening or coda in $PKPdf$, i.e., the $PKPdf$ pulses are much sharper than those seen in the data stacks. It is likely that the main source of $PKPdf$ pulse broadening and coda is strong scattering in the lithosphere. Because PKP precursor ray paths also traverse the lithosphere, they should be similarly affected. Thus, correctly modeling the relative amplitudes of PKP precursors compared to $PKPdf$ requires taking these pulse broadening effects into account, which in general will tend to increase precursor amplitudes compared to the peak $PKPdf$ amplitude. This is most easily done by convolving the seismic phonon results, in power, with a empirical function that roughly matches the $PKPdf$ observations. Later we will show how similar results can be obtained by explicitly including strong scattering in the lithosphere.

It is currently impractical to perform a rigorous grid search for a and ϵ because of the length of time required for each forward model. Through trial and error, we find that heterogeneity distributed throughout the entire mantle with $\epsilon = 0.1\%$ and $a = 6$ km closely agrees with the data stack, as shown in Figure 2.5.

Smaller values of a (e.g., 2 km) tend to over-predict amplitudes at short ranges and under-predict amplitudes at long ranges; larger values of a (e.g., 18 km) exhibit the opposite behavior. Figure 2.6 illustrates this effect of a on the synthetics.

This model assumes an inner core Q_α of 360 (*Bhattacharyya et al.* 1993). More recently, *Monnereau et al.* (2010) observed that the inner core exhibits hemispherical variations in both v_p and Q_α. The center of the low attenuation ($Q_\alpha = 410$) hemisphere is beneath the Americas and the high attenuation hemisphere ($Q_\alpha = 160$), beneath the Indian Ocean. We test how these other Q-values would affect our preferred model; we would have to adjust ϵ by less than $\pm 15\%$ to achieve equally good fits. The CD branch, which is unaffected by inner core attenuation, arrives just after the DF branch. In the case of strong core attenuation, the CD arrival takes the place of DF as the reference phase.

Figure 2.7 shows the preferred models from *Hedlin et al.* (1997) and *Margerin and Nolet* (2003b) as calculated by the seismic phonon method. The model proposed by *Hedlin et al.* (1997) overpredicts the observed amplitudes by a margin much larger than allowed by the data uncertainties whereas the model put forth by *Margerin and Nolet* (2003b) provides a reasonable fit. To test whether the poor fit of *Hedlin et al.* (1997) comes from using a single-scattering approach, we restrict the seismic phonon algorithm to output only singly scattered particles. We find, however, that 90% of the energy arriving near PKP experiences zero scattering events (these comprise the direct wave); 9% are scattered once (the Born term); and the remaining 1% are scattered multiple times. Therefore, a single-scattering assumption is unlikely to cause a factor of ten under-prediction of the scattered amplitudes.

Why, then, do our results disagree with those published by *Hedlin et al.* (1997)? We obtained a copy of the Born scattering code used by *Hedlin et al.* (1997) and were able to identify two problems that together resulted in a systematic under-prediction of the Born kernels by about a factor of eight. Specifically, the time bins in the numerical integration scheme were incorrectly normalized and the geometrical spreading factor was miscalculated for the second leg of each scattered wave. This accounts for the discrepancy. The overall shapes of the kernels,

however, are not significantly altered by this bug, so the *Hedlin et al.* (1997) conclusion that whole-mantle scattering fits the data better than CMB-only scattering remains valid. We confirm this result in our phonon calculations by restricting scattering to a 200-km-thick region above the CMB and choosing ϵ and a until we achieve a reasonable fit. Though the differences are admittedly subtle, the best fitting CMB-only model shown in Figure 2.8 rises more steeply than the data, then flattens while the data continue to rise, and under-predicts the observed amplitudes near the $PKPdf$ onset by a margin larger than the uncertainty estimates allow. If we increase ϵ to fit the later arriving precursors, the model increasingly over-predicts the earliest arriving amplitudes. This was previously noted by both *Hedlin et al.* (1997) and *Margerin and Nolet* (2003b).

Before moving on, we should emphasize that this result is based upon data that are narrow-band-filtered around 10 km. Features at longer or shorter scale lengths may—and probably do—exist, but these filtered data are not sensitive to them. As noted by *Cormier* (2000), the distinctness of D″ may disappear when one only considers the high-frequency part of the spectrum. We have chosen to work in this frequency band for the sake of resolving the disagreement between *Hedlin et al.* (1997) and *Margerin and Nolet* (2003b), but future work should make an effort to probe longer and shorter wavelengths.

We should also note that this method is subject to the limitations of ray theory, and—in its current form—is unable to model diffracted waves. We hope that we have avoided potential problems with this approximation by working in a sufficiently high frequency band, which is supported by the non-observation of the PKP diffracted wave near the b-caustic in our data stacks. Another potential issue is the amplification of the waves scattered in and out of the b-caustic, which this method treats via ray (or rather, particle) densities. We justify this approach because it is impossible to get infinite energy near a caustic because the algorithm sprays a finite number of particles. As computational capabilities improve, it would be useful to see how well global 3D numerical simulations of the wave equation agree with this high-frequency approximation.

2.4 Including lithospheric scattering

As shown by the white travel times curves in Figure 2.2, scattered energy near the b-caustic may arrive after the $PKPdf$ onset. If these amplitudes could be accurately observed, one could make stronger conclusions about the depth extent of small-scale structure in the mid-mantle. However, *Hedlin and Shearer* (2002) showed that in practice the large statistical variability in PKP coda makes constraining mid-mantle heterogeneity difficult. It is believed that much of this variability is caused by incoherence in depth phase arrivals between stacked events. Additionally, the observed waveforms pass through the strongly heterogeneous lithosphere, and the $PKPdf$ branch traverses the inner core, which has been shown to scatter high-frequencies (Cormier and Li 2002; Peng et al. 2008).

Although this study focuses primarily on fitting PKP precursors, we want our models to match, at least crudely, the coda shapes. Strong scattering in the lithosphere will spread energy out from both the PKP precursors and the main arrival. However, because the PKP precursors are already spread out in time, the result will be to increase the amplitude of the precursors relative to the peak $PKPdf$ amplitude. This effect can double the relative precursor amplitude just before the onset of $PKPdf$, most notably at ranges where the precursor onset time is earliest.

To incorporate the effect of the lithosphere, we develop and compare two different approaches. Figure 2.9 shows how each method affects the uncorrected amplitudes. The first approach, used previously to produce Figures 2.5, 2.7, and 2.8, simply entails a convolution, in power, of the seismic phonon output with an empirical function. In the second approach, the seismic phonon method explicitly models the lithospheric scattering. To the original three mantle volumes discussed in the previous section, we add a lithospheric scattering volume with $\epsilon = 4\%$ and $a = 4$ km from 0–200 km depth. We also augment the scattering strength in the uppermost mantle volume (depth range 200–600 km) by increasing ϵ to 3%. Improving upon the first approach, this method sprays particles for the full range of p and keeps track of P-to-S and S-to-P scattering. We like this approach because of its physical basis, but it is computationally expensive to sum over the full range

of p for both P- and S-waves, often requiring hundreds of CPU hours to obtain an acceptably smooth result.

For this study, we have mainly used the convolution method because of its speed and simplicity. Ultimately, however, we would like to use the seismic phonon method to model the effects of whole Earth scattering on the full length of the PKP envelope. *Cormier and Li* (2002) suggested that scattering is the predominant attenuation mechanism of the inner core for the 0.02–2 Hz frequency band. If we relax the $Q_\alpha = 360$ assumption and instead use the Cormier and Li (2002) scattering model ($\epsilon = 8.4\%$, $a = 9.8$km) in the uppermost 300 km of the inner core, the modeled precursor amplitudes are not significantly affected. The change of inner-core attenuation mechanism does, however, cause an amplitude increase in PKP coda, but this inner-core scattering model produces less than 50% of the the coda amplitude observed in the data stack. The remaining coda power is most likely generated by scattering in the lithosphere.

2.5 Discussion

2.5.1 Relevance to observations of P coda and Pdiff coda

PKP precursors are uniquely valuable to the study of deep small-scale structure because of their sensitivity to the lowermost mantle and because they arrive before the main phase rather than in its coda. However, as reviewed by *Shearer* (2007), there are a number of other scattered seismic phases that have at least some sensitivity to deep-Earth scattering.

Earle and Shearer (2001) modeled global stacks of Pdiff coda with a mantle containing evenly distributed fine-scale heterogeneity of $a = 2$ km and $\epsilon = 1\%$. Later, *Shearer and Earle* (2004) modeled Pcoda amplitudes between 30° and 90° using the seismic phonon method with $a = 8$ km and $\epsilon = 0.5\%$ throughout the lower mantle. Though these two models are non-unique, they show that observations of P coda and Pdiff coda are compatible with whole-mantle scattering. However, these models have lower-mantle velocity perturbations much stronger than the 0.1% perturbations that we have shown are consistent with PKP precursor

amplitudes. Thus, as shown in Figure 2.10, both proposed models systematically overpredict the data amplitudes. The reason for this discrepancy is not clear and will require further study. The *Earle and Shearer* (2001) *P*diff coda study used a single scattering theory and it is possible that strong scattering near the CMB could channel *P*diff scattered energy. *P* coda is dominated by strong scattering in the shallow Earth and it is possible that alternate models exist that could explain the data using only 0.1% velocity perturbations in the lowermost mantle. Alternatively, scattering in the lower mantle may be anisotropic, with stronger scattering occurring for the more horizontally traveling rays contributing to *P* coda than for the more vertically traveling rays contributing to *PKP* precursors. An analysis of broadband *PKP* waveforms by *Cormier* (1999) suggests that such anisotropy is unlikely to be present throughout the entire lower mantle, yet it may be a feature of the D″ layer. Our long-term objective is to find a self-consistent Earth model that can adequately explain the amplitudes of all the main scattered phases.

2.5.2 Geodynamical interpretation

Though a and ϵ have clear relevance to the Earth's velocity structure, these parameters should also provide constraints on geodynamical models of the mantle. The small values for a required to produce short-period precursors imply that the heterogeneity is of chemical, rather than thermal, origin. Here we identify possible avenues of interpretation.

- Slab recycling. Over geologic timescales, the near-surface rock cycle continuously creates compositional heterogeneity in the form of oceanic crust and underlying depleted lithosphere; subduction transports this heterogeneity into the mantle (e.g., *Stixrude and Lithgow-Bertelloni*, 2012). It has been proposed (e.g., *Brandenburg and van Keken*, 2007) that subducted oceanic crust may accumulate at the base of the mantle to form the seismically observed large low shear velocity provinces (LLSVPs). However, mantle convection models by *Li and McNamara* (2013) suggest that subducted oceanic crust is viscously stirred into the mantle at quicker rates than such structures would be able to form, implying that this heterogeneity may be distributed more

evenly throughout the mantle. Likewise, *Kaneshima and Helffrich* (2010) interpreted S-to-P scattering objects at mid-lower mantle depths (800 km to 2200 km) as subducted and folded oceanic crust. Their observations support the notion that small-scale heterogeneity persists for billions of years despite convective stirring and is ubiquitous in the lower mantle.

- Primordial mantle material. A portion of this chemical heterogeneity could be interpreted as primordial material which, through mantle convection, has been sheared, refolded, and interbedded with younger recycled material (e.g., *Albarède*, 2005). Mixing models by *Manga* (1996) support this notion that geochemical reservoirs can persist in the mantle for gigayears, provided that they are 10–100 times more viscous than the surrounding mantle.

- LLSVP-related silicate melt or iron enriched mantle. Using short-period arrays, *Frost et al.* (2013) deterministically located small-scale scatters that produced PKP precursors on seismograms recorded by the Yellowknife Array. These scatterers cluster into a ridge above the CMB beneath South Africa, possibly composed of dense residual material expelled to the edges of the LLSVP during convection.

- Small-scale variations in CMB topography. Although our preferred model contains heterogeneity uniformly distributed throughout the mantle, we cannot rule out contributions from CMB topography. Recently discovered rolling-hill structures on the CMB may have been formed by interactions between the outer core and the lowermost mantle (*Sun et al.*, 2012). Admittedly, these features are more than an order of magnitude larger than the ~ 10 km heterogeneities that would cause 1 Hz precursors, but such evidence for iron-rich structures at the base of the mantle raises the possibility that similar structures may exist at a smaller scale.

Absent from any of these interpretations is our preferred ϵ value of 0.1%. This global average may represent the product of the volume fraction of heterogeneous material and the velocity perturbation (in percent) of that material. To

determine which, if any, of the above interpretations provides the most plausible explanation for small-scale compositional heterogeneity in the mantle requires an interdisciplinary approach that considers both mineral physics and convective mixing calculations.

2.6 Conclusion

In summary, we have constructed global stacks of PKP precursor amplitudes from all available broadband seismograms recorded from 1990-2012 to find that they do not differ considerably from previous studies. We have modeled their envelopes using an energy-conserving, multiple-scattering approach to show, in accordance with *Margerin and Nolet* (2003b), that an r.m.s. perturbation of $\sim$0.1% explains the data. We have reconciled this result with the 1% value published by *Hedlin et al.* (1997) by finding a scaling error in their code. We have developed two separate methods to account for strong lithospheric scattering and have confirmed that small-scale ($\sim$10 km) heterogeneity is not confined to a 200-km-layer above the CMB. These results provide constraints on geodynamic and geochemical models of the lower mantle.

Acknowledgements

This research was supported by National Science Foundation grant EAR-111111. The authors thank Vernon Cormier, an anonymous reviewer, and the editor for suggestions that improved the quality of this manuscript. We wish to acknowledge the facilities of the IRIS Data Management System, and specifically the IRIS Data Management Center, which were used for access to waveform and metadata required in this study. The IRIS DMS is funded through the National Science Foundation under Cooperative Agreement EAR-1063471.

Chapter 2, in full, is a reformatted version of the material as it appears in Geophysical Journal International: Mancinelli, N. J., and P. M. Shearer, Reconciling discrepancies among estimates of small-scale mantle heterogeneity from PKP

precursors, Geophys. J. Int., 195, 1721-1729, doi: 10.1093/gji/ggt319, 2013. I was the primary investigator and author of this paper.

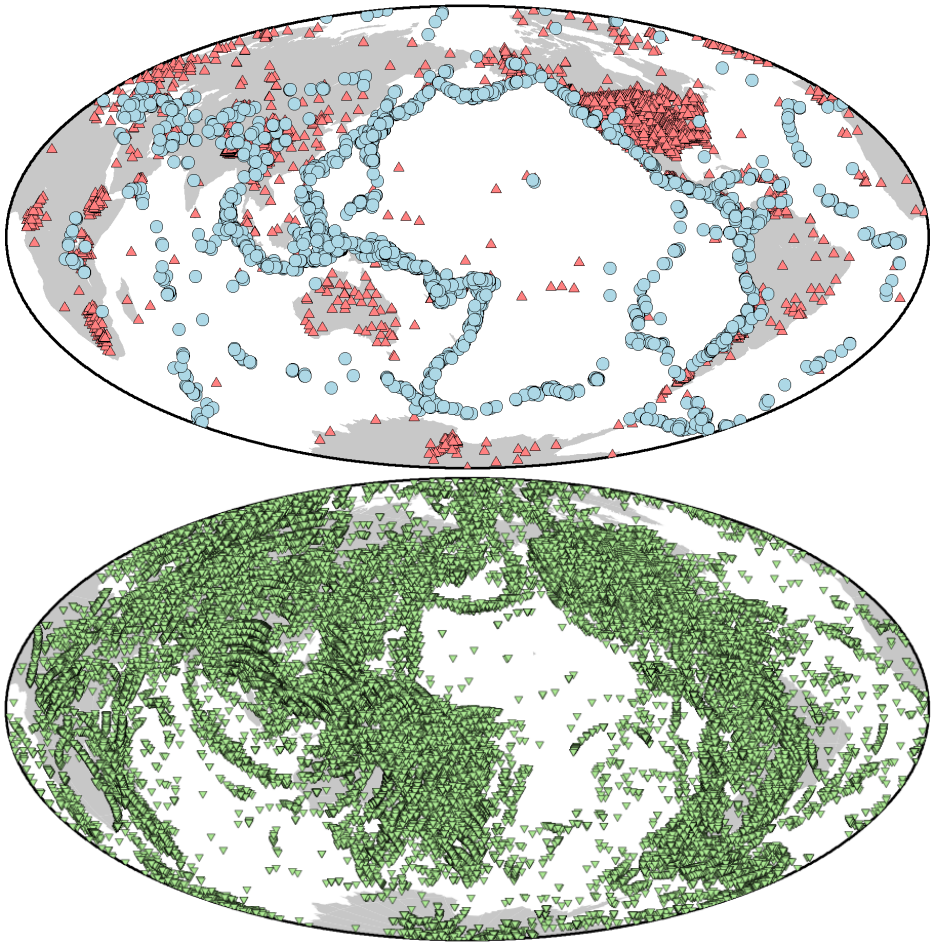

Figure 2.1: Top: Hammer projection showing source (blue circles) and receiver (red triangles) locations for waveforms analyzed in this study. Bottom: The green markers show approximate CMB entry-exit points.

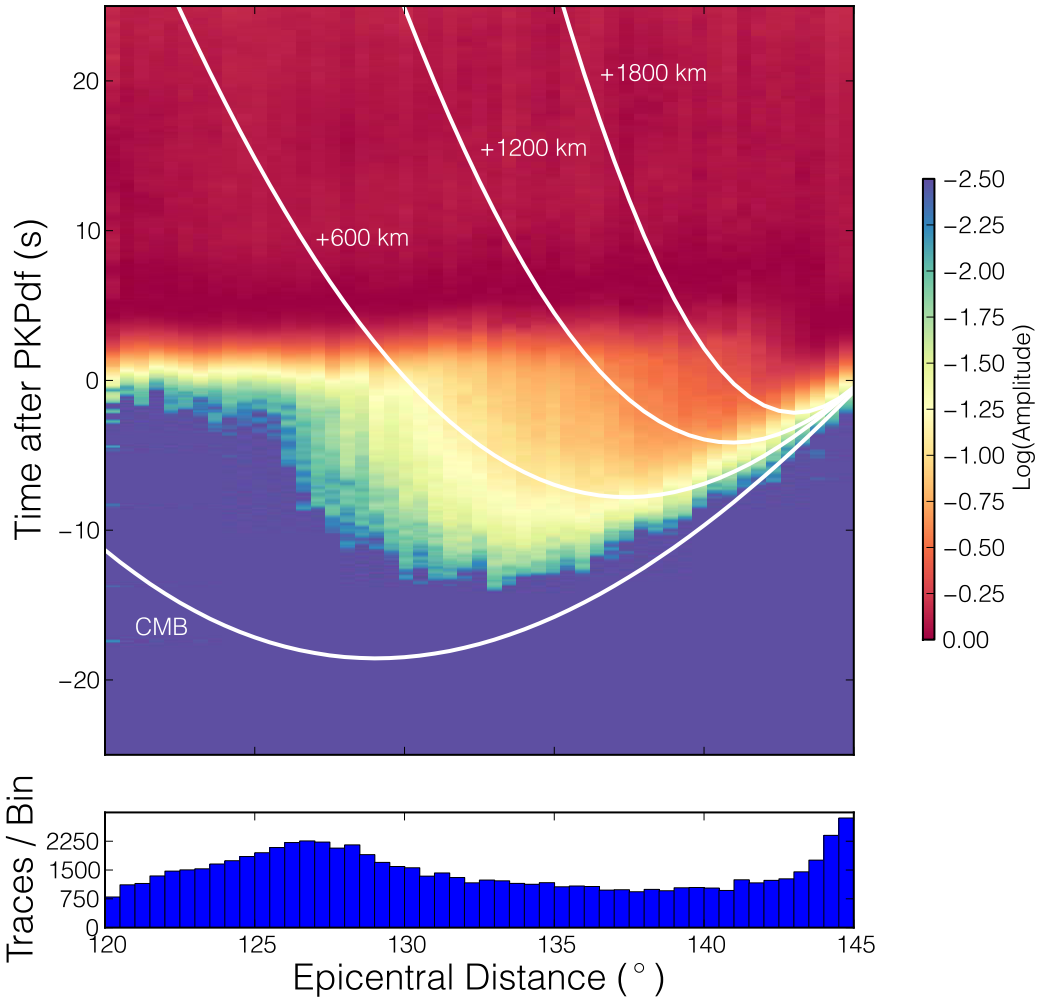

Figure 2.2: Top: Data stack showing the time and range dependence of PKP precursors. The time series are sampled at 20 Hz and are stacked in 0.5° range bins. Times are relative to the $PKPdf$ onset and amplitudes are relative to the $PKP(df,cd)$ maximum at each range. The white curves show earliest possible ray-theoretical arrival times for energy scattered above the CMB (units in km above the CMB). Bottom: Number of recordings stacked in each range bin.

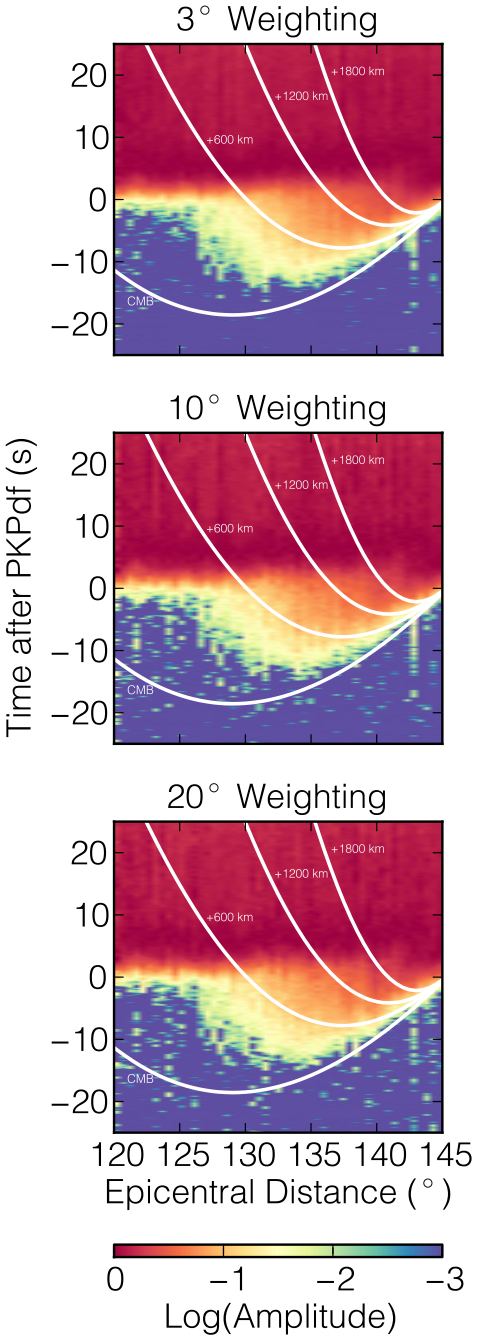

Figure 2.3: Comparison of different weighting schemes used to elicit globally averaged precursor amplitudes.

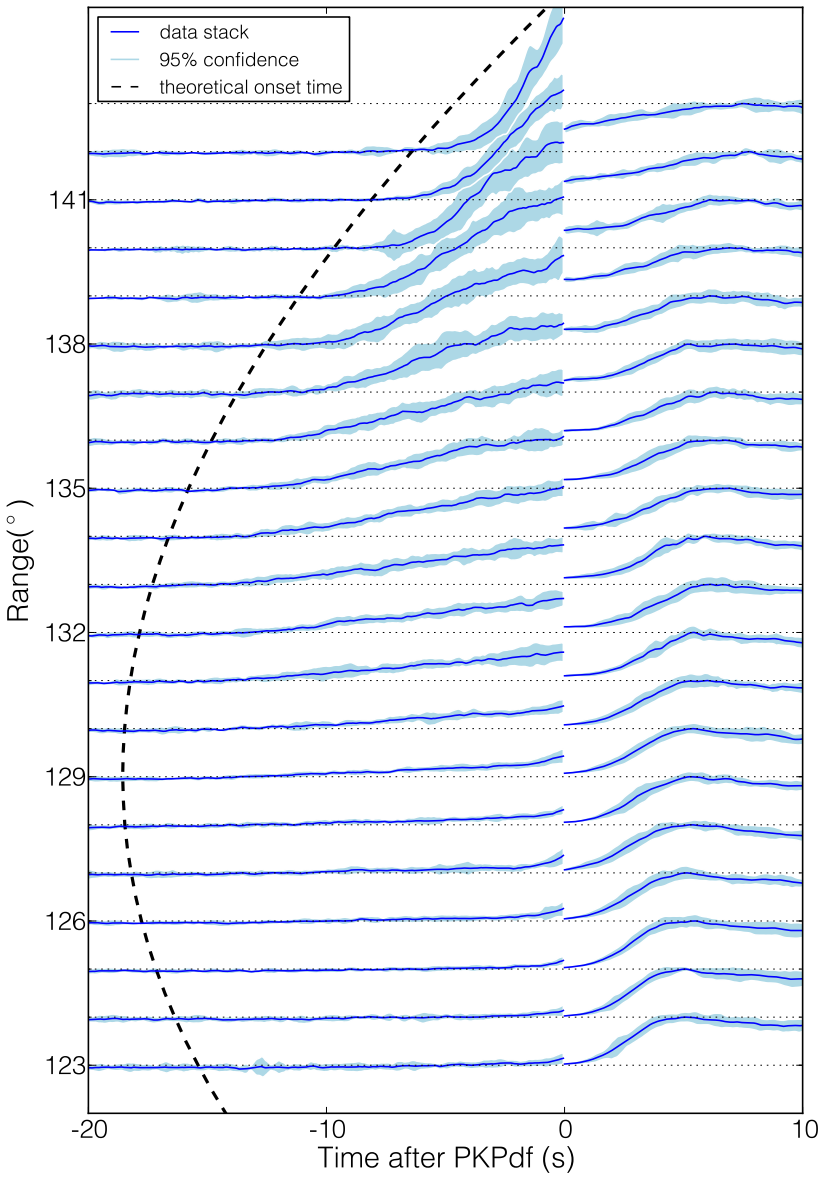

Figure 2.4: Vertical cross-sections of the data stack with 95% confidence limits from bootstrap resampling. To enhance visibility of the precursors, the stacks are scaled up by a factor of five at negative times. The dashed line shows the ray theoretical onset time for waves scattered at the CMB.

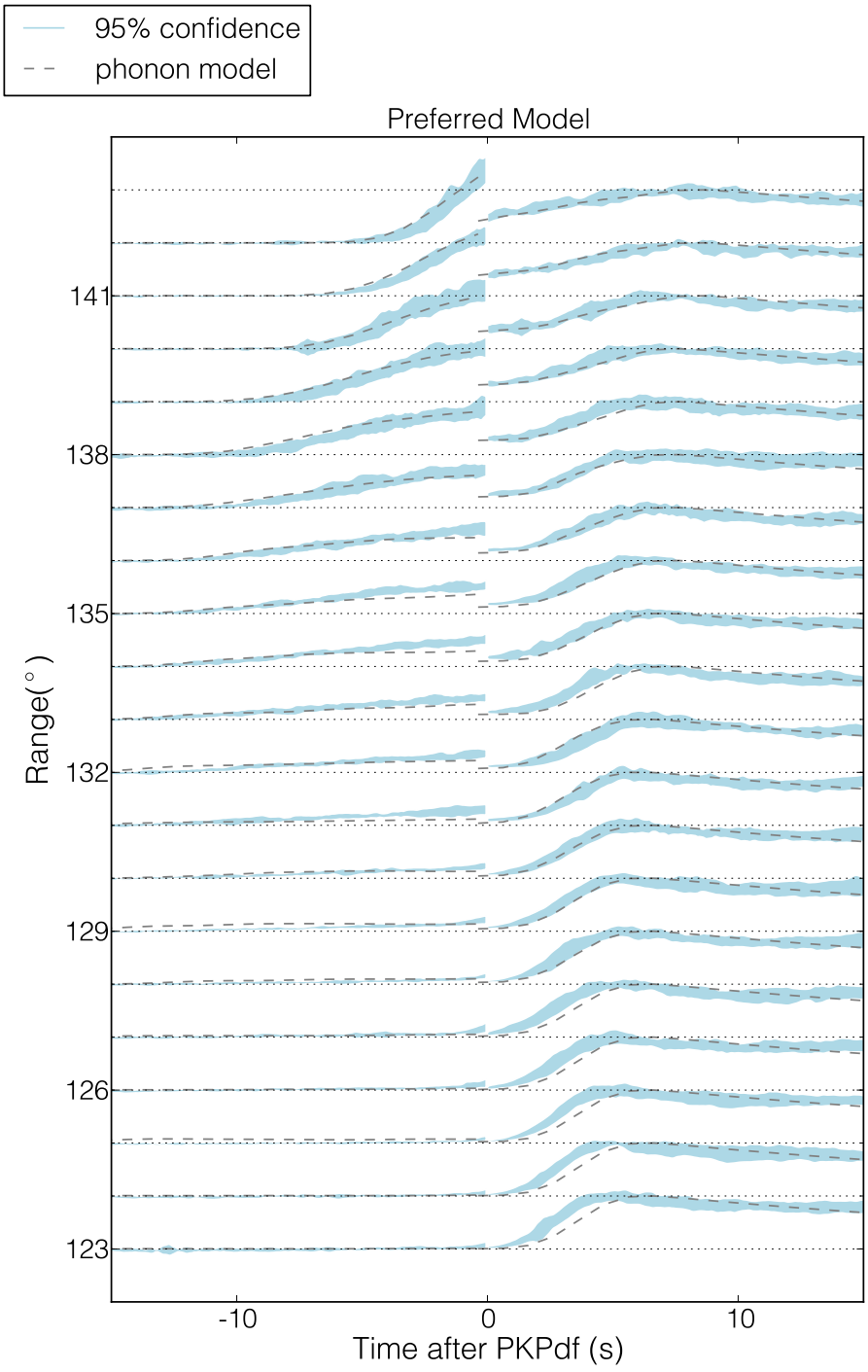

Figure 2.5: Preferred model plotted against the 95% confidence intervals of the data stack. Precursors are enhanced by a factor of three.

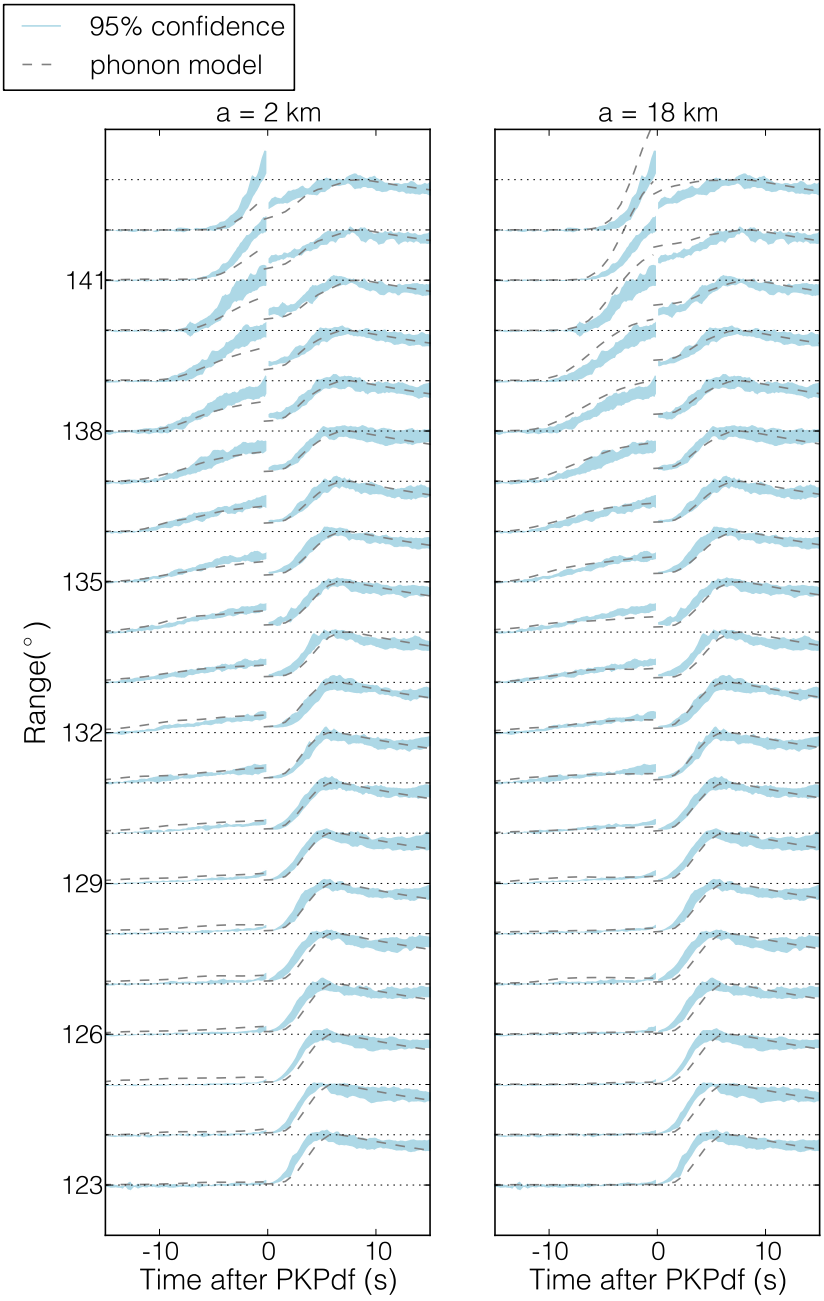

Figure 2.6: A demonstration of how these data are able to constrain correlation length. Left: An exponential model with $a = 2$km and $\epsilon = 0.2\%$ underpredicts the precursor amplitude at high ranges. Right: An exponential model with $a = 18$km and $\epsilon = 0.2\%$ overpredicts the precursor amplitudes at high ranges.

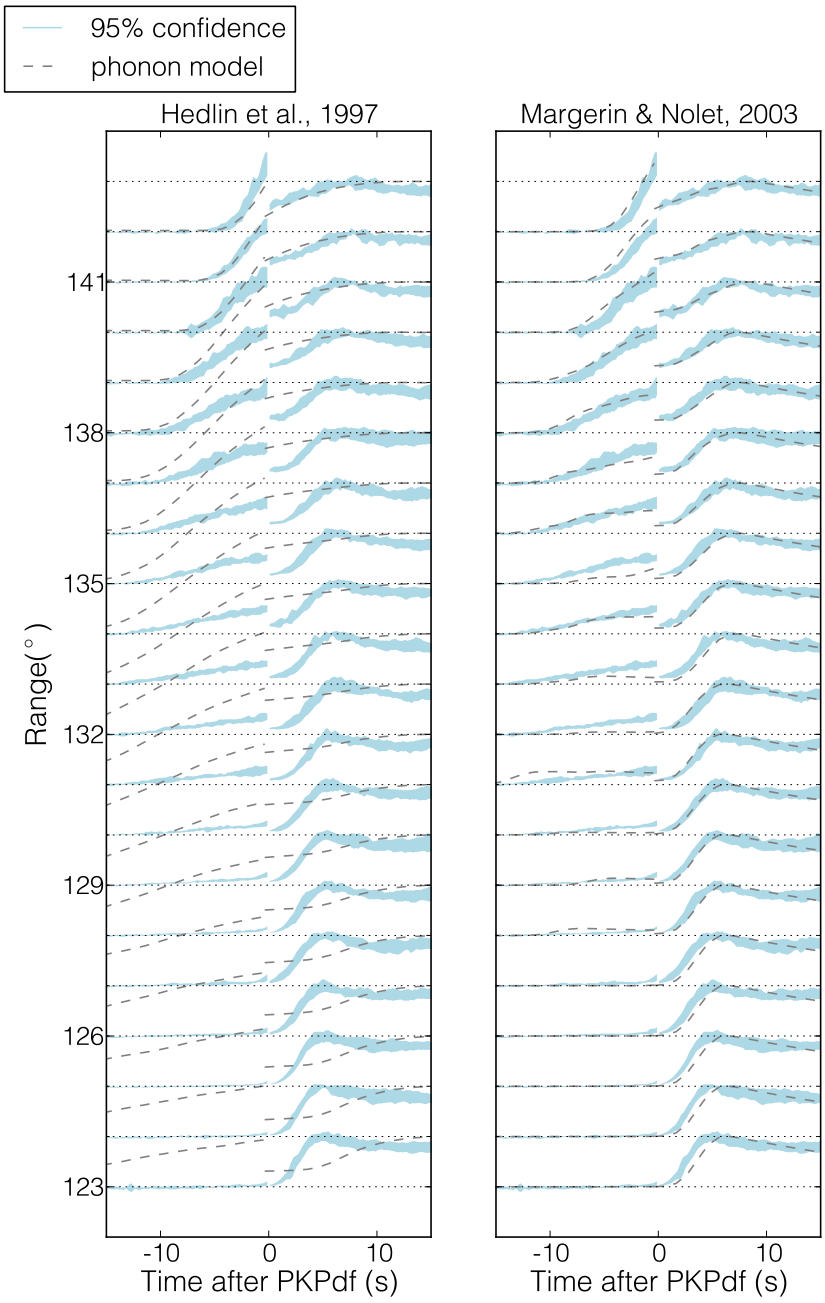

Figure 2.7: Synthetics generated by the seismic phonon algorithm plotted against our data stacks. The left column shows the *Hedlin et al.* (1997) preferred values of a and ϵ, whereas the right column shows the *Margerin and Nolet* (2003b) values. To enhance visibility of the precursors, the curves are magnified by a factor of three at negative times.

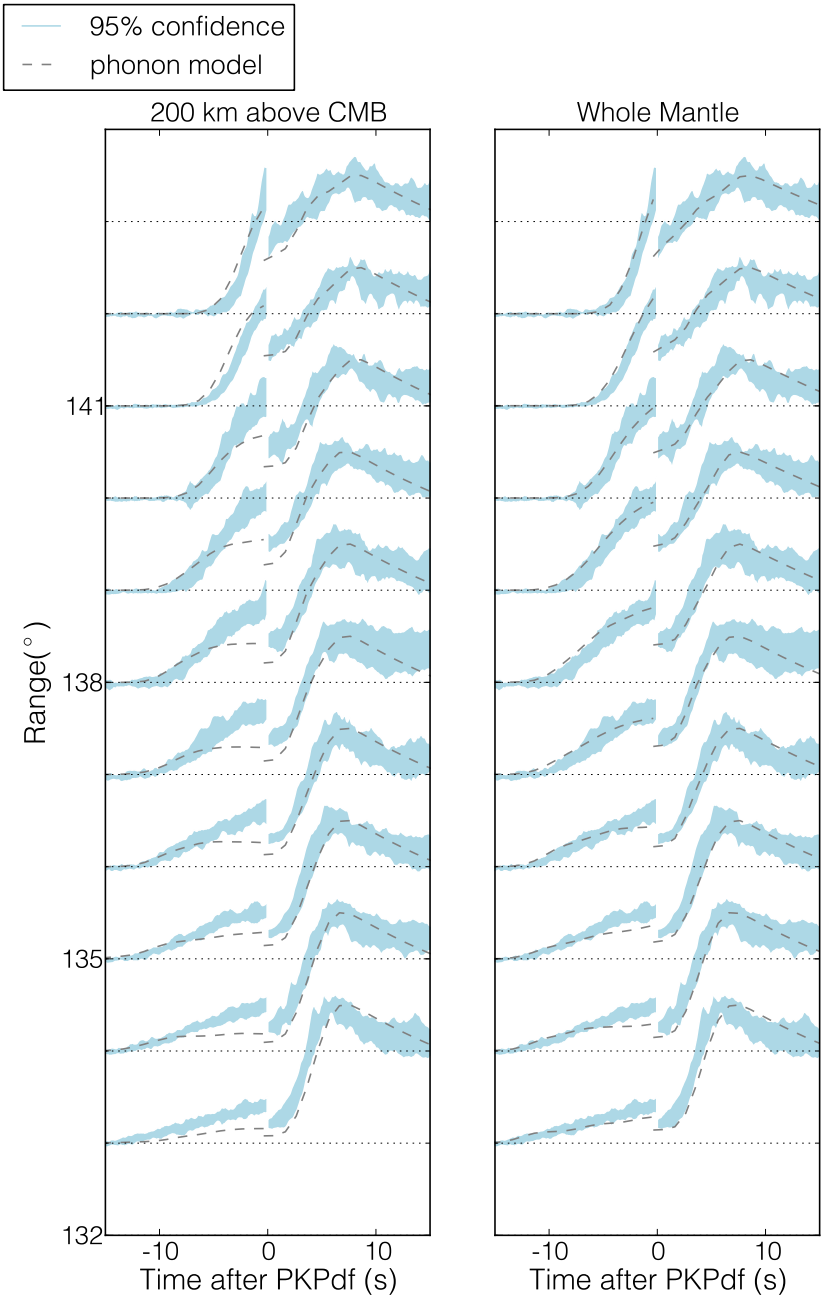

Figure 2.8: A comparison of a best-fitting whole-mantle scattering model with a best-fitting CMB scattering model. To highlight the difference between the two fits, the curves are magnified by a factor of three at negative times and by a factor of 1.5 at positive times.

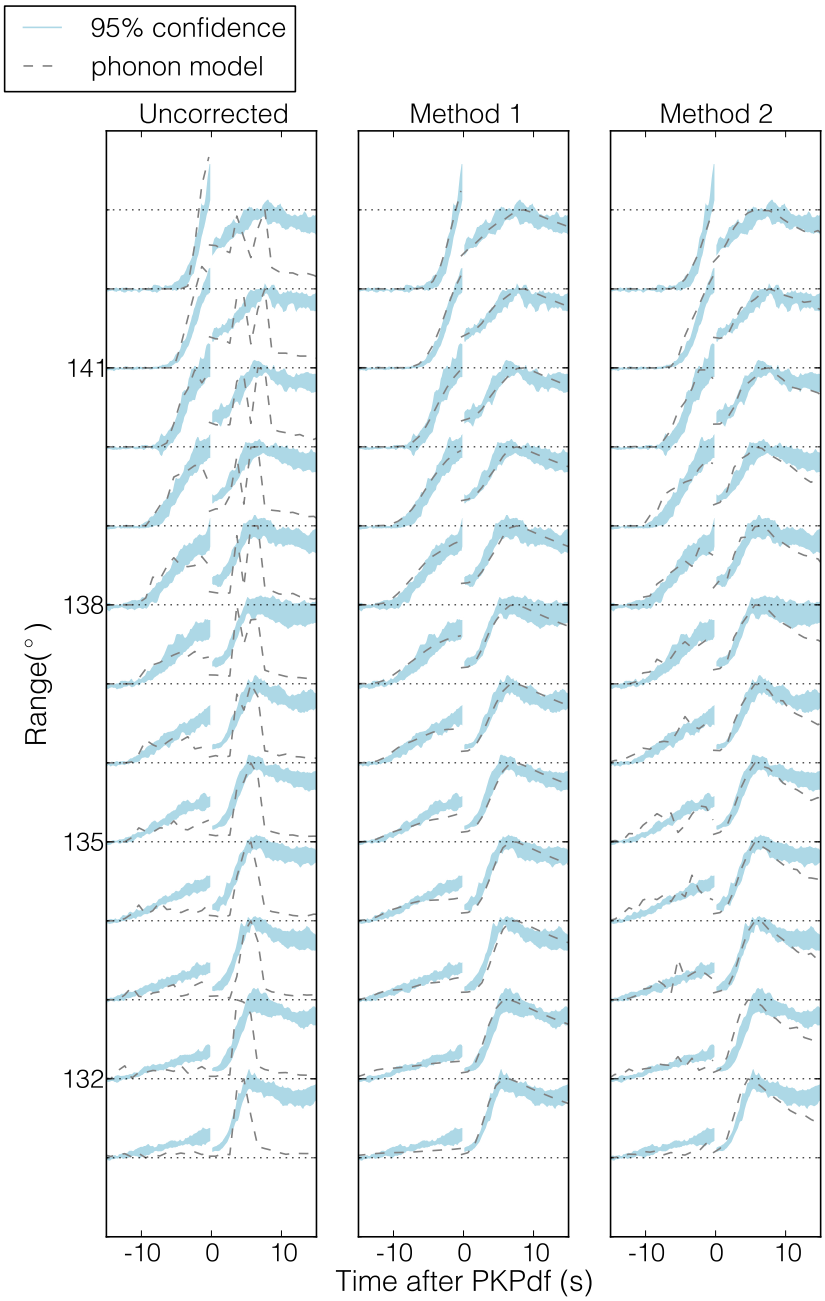

Figure 2.9: Two methods that account for strong scattering in the lithosphere. The leftmost column shows the uncorrected output of our preferred seismic phonon model. The center column shows the broadened amplitudes after convolution with an empirical function. The rightmost column shows broadened amplitudes obtained by direct modeling with the seismic phonon method. The precursors are enhanced by a factor of three.

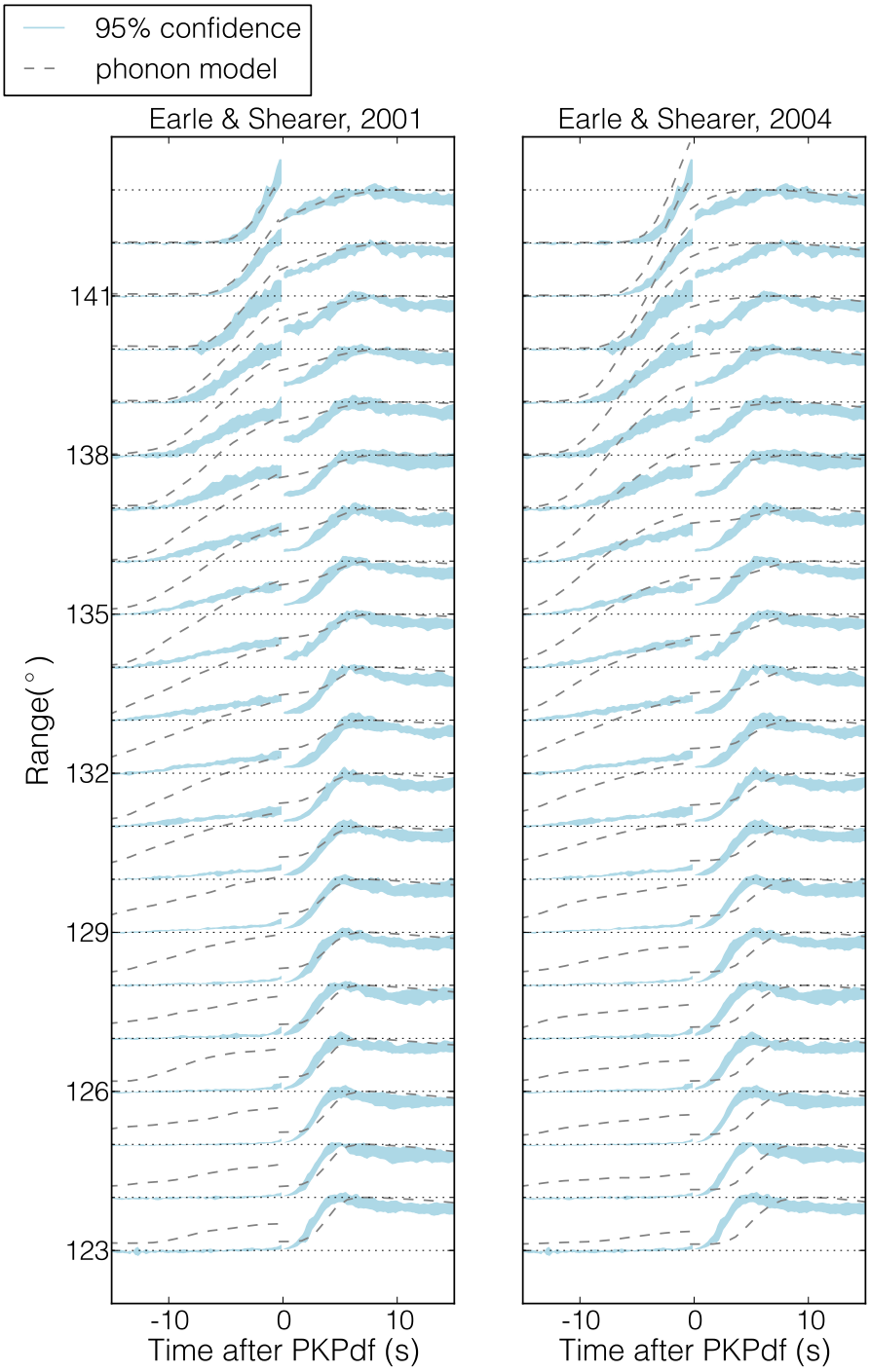

Figure 2.10: Seismic phonon predictions of preferred mantle scattering models from studies of Pdiff coda (left) and P coda (right). Convolution applied to correct for $PKPdf$ broadening. The precursors are enhanced by a factor of three.

References

Albarède, F., 2005. *The Survival of Mantle Geochemical Heterogeneities*, pp. 27–46, Earth's Deep Mantle: Structure, Composition, and Evolution.

Bhattacharyya, J., Shearer, P., and Masters, G., 1993. Inner core attenuation from short-period PKP(BC) versus PKP(DF) waveforms, *Geophysical Journal International*, **114**(1), 1–11.

Brandenburg, J. P. and van Keken, P. E., 2007. Deep storage of oceanic crust in a vigorously convecting mantle, *Journal of Geophysical Research: Solid Earth*, **112**(B6):B06403. doi:10.1029/2006JB004813.

Chernov, L. A., 1960. *Wave Propagation in a Random Medium*, vol. 960, McGraw-Hill.

Cleary, J. and Haddon, R., 1972. Seismic wave scattering near the core-mantle boundary: a new interpretation of precursors to PKP, *Nature*, **240**(5383), 549–551.

Cormier, V. F., 1999. Anisotropy of heterogeneity scale lengths in the lower mantle from $PKIKP$ precursors, *Geophysical Journal International*, **136**(2), 373–384.

Cormier, V. F., 2000. D$''$ as a transition in the heterogeneity spectrum of the lowermost mantle, *Journal of Geophysical Research: Solid Earth*, **105**(B7), 16193–16205.

Cormier, V. F. and Li, X., 2002. Frequency-dependent seismic attenuation in the inner core 2. A scattering and fabric interpretation, *Journal of Geophysical Research: Solid Earth*, **107**(B12), ESE 14–1–ESE 14–15.

Doornbos, D., 1978. On seismic-wave scattering by a rough core-mantle boundary, *Geophysical Journal of the Royal Astronomical Society*, **53**(3), 643–662.

Doornbos, D. and Vlaar, N., 1973. Regions of seismic wave scattering in the Earth's mantle and precursors to PKP, *Nature*, **243**, 58–61.

Dziewonski, A. M. and Anderson, D. L., 1981. Preliminary Reference Earth Model, *Physics of the Earth and Planetary Interiors*, **25**(4), 297–356.

Earle, P. S. and Shearer, P. M., 2001. Distribution of fine-scale mantle heterogeneity from observations of Pdiff coda, *Bulletin of the Seismological Society of America*, **91**(6), 1875–1881.

Frost, D. A., Rost, S., Selby, N. D., and Stuart, G. W., 2013. Detection of a tall ridge at the coremantle boundary from scattered PKP energy, *Geophysical Journal International*, doi:10.1093/gji/ggt242.

Haddon, R. and Cleary, J., 1974. Evidence for scattering of seismic PKP waves near the mantle-core boundary, *Physics of the Earth and Planetary Interiors*, **8**(3), 211–234.

Hedlin, M. A. and Shearer, P. M., 2000. An analysis of large-scale variations in small-scale mantle heterogeneity using Global Seismographic Network recordings of precursors to PKP, *Journal of Geophysical Research*, **105**(B6), 13655–13673.

Hedlin, M. A. and Shearer, P. M., 2002. Probing mid-mantle heterogeneity using PKP coda waves, *Physics of the Earth and Planetary Interiors*, **130**(3), 195–208.

Hedlin, M. A., Shearer, P. M., and Earle, P. S., 1997. Seismic evidence for small-scale heterogeneity throughout the Earth's mantle, *Nature*, **387**(6629), 145–150.

Kaneshima, S. and Helffrich, G., 2010. Small scale heterogeneity in the mid-lower mantle beneath the circum-Pacific area, *Physics of the Earth and Planetary Interiors*, **183**(1–2), 91–103, Special Issue on Deep Slab and Mantle Dynamics.

Kennett, B. L. N. and Engdahl, E. R., 1991. Traveltimes for global earthquake location and phase identification, *Geophysical Journal International*, **105**(2), 429–465.

Li, M. and McNamara, A. K., 2013. The difficulty for subducted oceanic crust to accumulate at the Earth's core-mantle boundary, *Journal of Geophysical Research: Solid Earth*.

Margerin, L. and Nolet, G., 2003a. Multiple scattering of high-frequency seismic waves in the deep Earth: Modeling and numerical examples, *Journal of Geophysical Research: Solid Earth*, **108**(B5), 2234, doi:10.1029/2002JB001974.

Margerin, L. and Nolet, G., 2003b. Multiple scattering of high-frequency seismic waves in the deep Earth: PKP precursor analysis and inversion for mantle granularity, *Journal of Geophysical Research*, **108**(B11), 2514, doi:10.1029/2003JB002455.

Monnereau, M., Calvet, M., Margerin, L., and Souriau, A., 2010. Lopsided growth of earth's inner core, *Science*, **328**(5981), 1014–1017.

Owens, T. J., Crotwell, H. P., Groves, C., and Oliver-Paul, P., 2004. SOD: Standing Order for Data, *Seismological Research Letters*, **75**(4), 515–520.

Peng, Z., Koper, K. D., Vidale, J. E., Leyton, F., and Shearer, P., 2008. Inner-core fine-scale structure from scattered waves recorded by LASA, *Journal of Geophysical Research*, **113**, B09312, doi:10.1029/2007JB005412

Rost, S. and Thomas, C., 2010. High resolution CMB imaging from migration of short-period core reflected phases, *Physics of the Earth and Planetary Interiors*, **183**(12), 143 – 150, Special Issue on Deep Slab and Mantle Dynamics.

Sato, H., and M. C. Fehler (1998), *Seismic Wave Propagation and Scattering in the Heterogeneous Earth*, Springer.

Shearer, P. M., 2007. Deep earth structure–seismic scattering in the deep earth, in *Treatise on Geophysics*, pp. 695 – 729, ed. Schubert, G., Elsevier, Amsterdam.

Shearer, P. M. and Earle, P. S., 2004. The global short-period wavefield modelled with a Monte Carlo seismic phonon method, *Geophysical Journal International*, **158**(3), 1103–1117.

Shearer, P. M. and Earle, P. S., 2008. Observing and modeling elastic scattering in the deep Earth, *Advances in Geophysics*, **50**, 167–193.

Stixrude, L. and Lithgow-Bertelloni, C., 2012. Geophysics of chemical heterogeneity in the mantle, *Annual Review of Earth and Planetary Sciences*, **40**(1), 569–595.

Sun, D., Helmberger, D. V., Jackson, J. M., Clayton, R. W., and Bower, D. J., 2012. Rolling hills on the core–mantle boundary, *Earth and Planetary Science Letters*, **361**, 333342.

Vidale, J. E. and Hedlin, M. A., 1998. Evidence for partial melt at the core–mantle boundary north of Tonga from the strong scattering of seismic waves, *Nature*, **391**(6668), 682–685.

Chapter 3

On the frequency dependence and spatial coherence of PKP precursor amplitudes

Abstract

Studies now agree that small-scale (∼10 km) weak (∼0.1%) velocity perturbations throughout the lowermost mantle generate the globally-averaged amplitudes of 1-Hz precursors to the core phase, PKP. The possible frequency dependence and spatial coherence of this scattered phase, however, has been given less attention. Using a large global dataset of ∼150,000 PKP precursor recordings, we characterize the frequency dependence of PKP precursors at central frequencies ranging from 0.5 to 4 Hz. At greater frequencies, we observe more scattered energy (relative to the reference phase PKP_{df}), particularly at shorter ranges. We model this observation by invoking heterogeneity at length scales from 2 to 30 km. Amplitudes at 0.5 Hz, in particular, suggest the presence of more heterogeneity at scales >8 km than present in previously published models. Using a regional bootstrap approach, we identify large (>20°), spatially-coherent regions of anomalously strong scattering beneath the West Pacific, East Africa, and Central/North America. Finally, as proof of concept, we use array processing techniques to lo-

cate the origin of scattered energy observed in Southern California by the Anza and Southern California Seismic Networks. The energy appears to come primarily from out-of-plane scattering on the receiver-side. We suggest that such improvised arrays can increase global coverage and may reveal whether a majority of precursor energy comes from localized heterogeneity in the lowermost mantle.

3.1 Introduction

Small-scale structure in Earth's lowermost mantle scatters seismic energy away from direct seismic waves, exciting a precursory wavetrain to the inner-core phase PKP_{df} (*Cleary and Haddon*, 1972). Studies now agree that small-scale ($\sim$10 km) velocity perturbations of $\sim$0.1% distributed throughout the lower mantle match the globally-averaged time- and range-dependence of the precursor amplitudes at 1 Hz (*Margerin and Nolet*, 2003a; *Mancinelli and Shearer*, 2013), but there is still uncertainty regarding the primary type of heterogeneity responsible for lower-mantle scattering (*Waszek et al.*, 2015). Several ideas have been proposed, including core-mantle boundary (CMB) topography (*Doornbos*, 1978), partial melt (*Vidale and Hedlin*, 1998), remnants of fossil slabs (*Cao and Romanowicz*, 2007), dense material related to Large Low-Shear Velocity Provinces (LLSVPs) (*Frost et al.*, 2013), and Ultra-Low Velocity Zones (ULVZs) (*Yao and Wen*, 2014). In order to gain further insight into which of these is the primary cause of lower-mantle scattering, we present a study of the frequency dependence and spatial coherence of PKP precursors.

Since it has become generally accepted that PKP precursors are scattered waves from the deep mantle, several types of random media have been invoked to model them. *Bataille and Flatte* (1988) approximated the spectrum of inhomogeneities in the lowermost mantle by a power law, solving for the exponent by measuring changes in precursor amplitude with respect to scattering angle. *Cormier* (1995) used Gaussian media with correlation lengths from 20–35 km and rms velocity perturbations around 10% to synthesize precursor waveforms that matched a limited set of observed seismograms. Shortly thereafter, *Hedlin et al.* (1997)

modeled a global stack of precursor waveforms with exponential random media with a correlation length of 8 km. *Margerin and Nolet* (2003a), likewise, modeled global stacks of 1-Hz waveforms with exponential media, but found that the observed range dependence was not well matched. To better fit the observations, they proposed an alternative model richer in small-scale heterogeneity, noting that the correlation length associated with this model was fundamentally unresolvable due to the limited range of observations. Others (*Hedlin et al.*, 1997; *Mancinelli and Shearer*, 2013), however, found that adjusting the correlation length of an exponential model provided sufficient control in fitting range-dependence of the precursor energy.

Less attention has been paid to the possible frequency dependence of PKP precursors. Although regional studies (*Cormier*, 1999; *Thomas et al.*, 1999, 2009) have explored the frequency content of the scattered energy, global studies (*Hedlin et al.*, 1997; *Margerin and Nolet*, 2003a; *Mancinelli and Shearer*, 2013) have focused on observations in a single frequency band centered at 1 Hz, because the scattered energy has the highest signal-to-noise at that frequency. In theory, observations of scattered energy at a given frequency are primarily sensitive to structure comparable in size to the seismic wavelength. Observations over a range of frequencies, therefore, ought to provide direct constraints on how heterogeneity power changes with length scale and thus should help discriminate between the various types of random media that have been proposed.

Here, we present global stacks of PKP precursors filtered in four non-overlapping bands with central frequencies ranging from 0.5–4.0 Hz. We show that the range-dependence of the scattered energy changes as a function of frequency. To model this observation, we generate synthetics from several types of random media models, ultimately finding that power-law heterogeneity spectra with exponents of -3 and -2.6 produce better fits than exponential models. We then attempt to map possible lateral variations in lower-mantle scattering strength by comparing regional stacks of data with the global average. We find large-scale regions of strong scattering beneath the West Pacific, East Africa, and Central/North America. The statistical significance of these observations is confirmed by boot-

strap resampling and spatial coherence tests. Lastly, we demonstrate as a proof of concept that groups of nearby stations can be used to estimate the source regions of scattered energy. We use array processing techniques—vespagrams, beamforming, and waveform cross-correlation—to locate the source of the scattered energy recorded in Southern California. In light of these findings, we conclude with a discussion of the likely sources of lower-mantle scattering and of promising future research directions.

3.2 Methods I: Data stacking

We obtain a global dataset of PKP waveforms from an online archive maintained by the Incorporated Research Institutions for Seismology (IRIS). In this study, we use the same data that were used in the single-frequency study by *Mancinelli and Shearer* (2013), composed of ∼150,000 broadband vertical channels (BHZ) recorded from 1990–2012 for shallow events (depth $<$ 50 km) with $M_{\mathrm{W}} \geq 5.7$ and deep events with $M_{\mathrm{W}} \geq 5.5$.

At each frequency, we characterize the time- and range-dependence of the scattered energy by employing an envelope stacking procedure similar to previous PKP-precursor studies (*Hedlin et al.*, 1997; *Margerin and Nolet*, 2003a; *Mancinelli and Shearer*, 2013). To characterize the frequency dependence, we repeat the stacking procedure with different bandpass filters (0.4–0.75 Hz, 0.75–1.5 Hz, 1.5–3 Hz, and 3–6 Hz). A separate culling step is applied for each frequency, so each stack may be composed of a different subset of seismograms. The number of seismograms in each stack varies with both range and frequency; the exact numbers are shown in Figure 3.1. Despite the relatively small number of seismograms in the 3- to 6-Hz stack, bootstrap resampling tests suggest that the stacked precursor amplitudes are stable. We apply this procedure on waveforms filtered from 5–10 Hz (not shown), but no signal is discernible at these high frequencies. We also obtain stacks at lower frequencies (0.1–0.2 Hz and 0.2–0.4 Hz, not shown), but these observations may be influenced by diffraction near the b-caustic and we do not attempt to model them in this study. At frequencies lower than 0.1 Hz, the precursors are indiscernible

because they overlap with the main phase (c.f., *Thomas et al.*, 2009).

The most remarkable feature of these stacks is that, with increasing frequency, the precursors become more visible at shorter ranges. Since precursors are understood to be waves scattered into and out of the b-caustic at 145° (*Cleary and Haddon*, 1972), this suggests that increased amounts of large-angle scattering is involved at higher frequencies. For 3-D heterogeneity spectra of the form $P(m) \propto m^n$, the scattering pattern is proportional to m^{4+n} (*Shearer and Earle*, 2004, eq. 4). Thus, to have increasing scattering power with frequency for a given angle, the power-law exponent n must be greater than -4. (For reference, an exponential model has an exponent of -4 in the large wavenumber limit.) In the following section we will explicitly define various forms of the heterogeneity spectrum and discuss how well each fits the observed PKP precursor amplitudes.

3.3 Methods II: Waveform modeling

3.3.1 Random media models

To forward model the global stacks, we take a statistical approach. We define heterogeneity power as a function of wavenumber, and from this assumption we calculate the scattering properties of the medium as a whole. Each random medium is parameterized by an autocorrelation function, $R(\mathbf{x})$, or alternatively, its three-dimensional (3-D) Fourier transform, the power spectral density function (PSDF):

$$P(\mathbf{m}) = \iiint_{-\infty}^{\infty} R(\mathbf{x}) e^{-i\mathbf{m}\cdot\mathbf{x}} d\mathbf{x} \tag{3.1}$$

where $\mathbf{x}$ is the lag position vector and $\mathbf{m}$ is the angular wavenumber vector. In this study, we consider only random media with isotropic heterogeneity properties. In mathematical terms, R and P depend only on x and m, respectively, where $x = ||\mathbf{x}||$ and $m = ||\mathbf{m}||$ (*Sato et al.*, 2012).

3.3.2 Phonon models

Once a PSDF has been defined for each scattering layer within our model, we use a particle-based phonon approach (*Shearer and Earle*, 2004) to forward calculate the wavefield. We run each simulation at a single frequency, f_0, computed as the harmonic mean of the filter bandlimits, f_1 and f_2, i.e.:

$$f_0 = \left[\frac{1}{2} \left(f_1^{-1} + f_2^{-1} \right) \right]^{-1} . \tag{3.2}$$

This parameter affects the scattering coefficients and intrinsic attenuation.

In this study, we distribute heterogeneity throughout the lowermost 1200 km of the mantle. Previous work has shown that full mantle scattering gives better fits to the time-dependence of the 1-Hz stacked precursors than do models where heterogeneity is restricted to the CMB or the D″ region (*Hedlin et al.*, 1997; *Cormier*, 1999; *Margerin and Nolet*, 2003a; *Mancinelli and Shearer*, 2013). We confirm that a 1200-km-thick scattering layer is an appropriate assumption for this work by forward modeling the time-dependence at various frequencies. Layers thicker than 1200 km do not appear to affect the synthetics, probably because most of the scattered energy from shallower depths arrives after PKP_{df}. Shrinking the layer down to a thickness of 200 km (i.e., D″ scattering) produces synthetics with constant amplitudes at greater times; this does not match the observed ramp-like time-dependence. There is an exception at 4 Hz where the uncertainties in the data stacks are too large to distinguish between the two cases.

Scattering by strong heterogeneity in the lithosphere and upper mantle affects the precursor amplitudes indirectly by broadening the PKP_{df} arrival and exciting postcursors (*Cormier*, 1995; *Thomas et al.*, 2000). Since the precursors are already spread out in time, the relative amplitude of the precursor wavetrain is effectively increased. At the cost of computational speed, lithospheric scattering can be modeled directly by the phonon code. Alternatively, one can convolve the output of the phonon code, in power, with an empirical broadening function to account for this effect. Since both methods produce similar results (*Mancinelli and Shearer*, 2013), we use the convolution approach for the sake of computational efficiency.

To be consistent with previous studies, we assume that the P-wave quality factor (Q_α) for the inner core is 380 (*Bhattacharyya et al.*, 1993). Another parameter that we have to set is the velocity-density scaling ratio ν; we choose 0.8 which is the estimated lithospheric value from Birch's Law. It has been shown previously that adjusting this parameter has no significant effect on the modeled precursor amplitudes since forward (rather than backward) scattering is involved (*Mancinelli and Shearer*, 2013).

3.4 Fitting the frequency dependence

Before moving into a quantitative discussion of the various models and their data fits, we would like to illustrate how simple models can produce the observed change in the PKP precursor range-dependence as a function of frequency. Figure 3.2, for example, shows the phonon code prediction for a random media model with an H-G spectrum (Equation 3.4, below) that contains self-similar heterogeneity at length scales smaller than 1000 km. These images show greater amounts of scattered energy at short ranges with increasing frequency, just as is observed in the data stacks.

For a more quantitative treatment, we compare our global stacks with phonon code predictions of the scattered wavefield assuming various types of random media. We focus on finding a single spectrum that simultaneously fits the range-dependence in each of the four frequency bands (0.5, 1, 2, and 4 Hz). To assess the performance of each model, we plot the mean amplitude in a 6-s time window before the onset of PKP_{df} for each range bin. The 95% confidence intervals are estimated using a similar procedure. We find models that achieve reasonble fits to the data by trial and error; a formal inversion is currently impractical due to the time required to run each phonon model and the lack of a convergence criterion that is reliable for a large set of models.

The first spectrum we test is the exponential random media model previously published by *Mancinelli and Shearer* (2013). The 3-D PSDF is given by

$$P(m) = \frac{8\pi\epsilon^2 a^3}{\left(1 + a^2 m^2\right)^2} \tag{3.3}$$

and is plotted in Figure 3.3 with a correlation length, a, of 6 km and an rms velocity fluctuation, ϵ, of 0.2%. Exponential models have more small-scale structure than Gaussian models, but most of the variance remains at wavelengths comparable to the correlation length. For a correlation length of about 6 km, as was preferred by *Mancinelli and Shearer* (2013), the observations are fit reasonably well, although there is not enough scattered energy at ranges greater than 138° at 0.5 Hz (Figure 3.4). If one raises the correlation length of the exponential model to 50 km in order to increase the amount of low-angle scattering, the fits at 1, 2, and 4 Hz degrade because of the relatively rapid fall-off rate of the PSDF.

Margerin and Nolet (2003a) proposed an H-G spectrum (after *Henyey and Greenstein*, 1941) that is richer in fine-scale heterogeneity:

$$P(m) = \frac{\epsilon^2 a^3}{(1 + a^2 m^2)^{1.5}}. \tag{3.4}$$

This spectrum has the property of self-similarity (i.e., constant power-per-octave) in the limit where $am \gg 1$. When testing these models, we find that an upper limit on the correlation length a is unresolvable, which was also noted by *Margerin and Nolet* (2003a). As shown in Figure 3.5, including heterogeneity as large as 30–80 km produces better fits to the long range ($> 140°$) precursors at 0.5 Hz. The correlation length of 30 km provides enough large-scale heterogeneity to fit the observations within error, but extending this value to 80 km does produce a model that more closely tracks the 0.5-Hz stack. Increasing the correlation length to values greater than 80 km does not significantly alter the model prediction. We notice that the H-G models systematically overpredict scattering at 2 Hz at ranges greater than 140°.

To address this, we try an Alternate Model (hereafter referred to by AM) that is even richer than H-G in fine-scale structure:

$$P(m) = \frac{\epsilon^2 a^3}{(1 + a^2 m^2)^{1.3}}. \tag{3.5}$$

This model still fits the range-dependence at 0.5, 1, 2, and 4 Hz within the estimated data uncertainties, and more closely matches the long-range amplitudes at 2 Hz. Thus, we argue that the AM spectrum has the "best-fitting" power-law

exponent of -2.6. The predictions of the three types of models (i.e., exponential, H-G, and AM) are shown together with the data in Figure 3.4.

Although the phonon code accounts for multiple scattering, it is interesting to reevaluate whether single (Born) scattering is a suitable assumption for this problem. For the best fitting H-G model with $a = 80$ km, the lower-mantle mean-free-paths are 40,000; 14,000; 5,900; and 2,800 km for 0.5, 1, 2, and 4 Hz respectively. Benchmarking tests from *Margerin and Nolet* (2003b) suggest that mean-free-times less than 400 s (i.e., mean-free-paths shorter than ∼5300 km) require multiple scattering to be accurate within 20% error. Therefore, single scattering seems to be adequate for PKP precursors at 0.5, 1, and 2 Hz, but possibly not at 4 Hz. The transport mean-free-paths (c.f., *Przybilla et al.*, 2009)—580,000; 290,000; 140,000; and 71,000 km—are considerably larger than the standard mean-free-paths. This suggests that the scattering pattern is strongly anisotropic (i.e., most scattering events redirect energy by only a very small angle); this is not surprising considering that the preferred H-G model has increased amounts of large-scale structure.

In Equations 3.4 and 3.5, the parameter ϵ represents a scaling factor rather than the rms velocity fluctuations of the medium. Strictly speaking, the H-G and AM spectra have infinite variance when integrated over the entire spectrum. This, of course, is unphysical. To estimate the physical variance, one should integrate the spectrum only to a wavenumber corresponding to half of the seismic wavelength (*Margerin and Nolet*, 2003a, eq. 12). At lower-mantle velocities and at a maximum frequency of 4 Hz, the largest wavenumber (smallest wavelength, respectively) that we can expect to constrain is ~ 4 km^{-1} (2 km).

3.5 Lateral variations

Mapping lateral variations in scattering strength may help in understanding the nature of the lower-mantle scatterers. This problem is complicated by the fact that both source- and receiver-side heterogeneity scatter precursor energy, and one cannot uniquely map amplitudes observed at a single station to a point

of origin in the lower mantle. In an initial attempt at this problem, *Hedlin and Shearer* (2000) inverted for scattering source regions using Global Seismographic Network (GSN) recordings of PKP precursors. The authors noted rough correlations between large-scale tomography anomalies including the African plume and the Tethys trench, but acknowledged that these were "tentative rather than definitive" based on bootstrap resampling tests. In a recent global study of PKP precursors, *Waszek et al.* (2015) found no correlation between scattering and large-scale velocity structure at the core–mantle boundary (CMB) and noted much variability of the amplitudes within each region.

Here we attempt to solve the problem in a different way. For each seismogram in our dataset, we calculate the CMB piercing points for the PKP_{df} phase. We divide the surface of the CMB into 20° regional cells and group the waveforms by the source-side piercing point. We further divide each regional cell into 8 azimuth bins and construct a 2-D stack (e.g., Figure 3.1) for the data (bandpass filtered from 0.7–2.5 Hz) in each bin. We measure the average amplitude deviation of each regional stack by subtracting the global average (*Mancinelli and Shearer*, 2013) and taking a weighted mean of the resulting difference in a 20-s window before the onset of PKP_{df}. The weights correct for the fact that weak amplitudes tend to occur at short ranges whereas strong amplitudes tend to occur at long ranges. This distills each regional 2-D stack into a single scalar measurement that can be plotted on a map. We quantify the statistical significance of each measurement by bootstrap resampling the set of seismograms and recomputing the 2-D stack and its associated scalar statistic. We deem a regional deviation to be significantly strong (or weak, respectively) if 95% of 1000 bootstrap estimates are above (or below) zero. We repeat this entire exercise assuming that the scattering occurs near the receiver-side piercing point.

After plotting the median deviations for each bin on the maps in Figure 3.6, we find large regions of spatially-coherent strong scattering in the West Pacific, Central/North America, and East Africa. We also identify several regions that display azimuthally-dependent scattering behavior. Receiver-side scattering in western North America, for example, shows stronger-than-average amplitudes for rays

coming from the south and weaker-than-average amplitudes for rays coming from the north. Also, the region near 0° E 60° S displays strong scattering for rays along the ENE–SWS axis and weak scattering along for rays the WNW–ESE axis. These patterns may arise from the shape of the scatterers (i.e., anisotropic heterogeneity) or from differences in scattering properties in the far-side scattering regions. In 9 out of the 10 cases where both maps show a deviation in the same bin, both maps agree on the sign of the deviation. The only exception is a bin near 20° N 70° W.

As an additional check on the reliability of these observations, we conduct a test to determine the average spatial coherence of PKP precursor amplitudes for our global dataset. What we want is a measure, as a function of ray separation, of how likely it is for two measurements of precursor amplitudes to be similar. We define the log-amplitude difference between a pair of precursor waveforms with amplitudes A_1 and A_2 as $\log_{10}(A_1^*) - \log_{10}(A_2^*)$; the asterisks denote that the raw amplitudes have been divided by the global average to correct for systematic variations caused by the range-dependence of this phase. The ray separation is defined as $\sqrt{(\Delta_s^2 + \Delta_r^2)/2}$ where Δ_s and Δ_r are the great circle distances between the two sources and the two receivers, respectively. For each pair, we plot the absolute difference between the log-amplitudes versus ray separation in Figure 3.7. Due to the variability in these measurements it is difficult to see a trend when looking at the raw scatter plot. To address this, we split the measurements into bins by ray separation (log scale) and plot the median absolute log-amplitude difference in each bin (black circles, Figure 3.7). These medians reveal a trend whereby the absolute differences in log-amplitude increase with greater values of ray separation from about 0.02° to 90°. This suggests that large-scale global variations in precursor amplitude do exist within our dataset.

Ideally we would expect the log-amplitude difference to approach zero at increasingly small values of ray separation. We observe, however, that this parameter stops decreasing at ray separations between 0.01° and 0.05°; this is likely because of incoherent noise recorded at nearby (but not colocated) stations. For the case of colocated channels (not plotted because of log x-axis), the log-amplitude difference is nearly zero.

3.6 Array processing

Array methods provide another means to better understand the origin of lower mantle scattering. Determining the slowness and backazimuth of precursor waves can in principle resolve the source–receiver ambiguity discussed in the previous section (*Thomas et al.*, 1999; *Cao and Romanowicz*, 2007; *Frost et al.*, 2013). In recent years, many broadband stations have been deployed to address questions about the lithosphere and upper mantle. Here we explore how data from these stations could be used to expand global coverage of precursor slowness and backazimuth measurements.

We apply array processing techniques (*Rost and Thomas*, 2002) to PKP precursors from the 30 September 2009 M_{W} 7.6 earthquake in southern Sumatra recorded by an array of stations in Southern California. The array geometry is shown in Figure 3.8. The primary goal of this exercise is to determine whether the precursor energy originates from the source- or receiver-side. Using the Seismic Handler analysis program (*Stammler*, 1993), we construct 4th-root vespagrams to constrain the precursor slowness. Prior to stacking, the seismograms are filtered to high frequency (1–2 Hz). We find that the precursor energy is diffuse in the vespagrams when assuming the theoretical backazimuth of 305°, yet the energy of the main phase is strong and the slowness is well constrained. As shown in Figure 3.9, reducing the backazimuth to about 275° gives clear precursor energy in the vespagram with a slowness of 3.2 ± 0.3 s/° followed by a weaker precursor with a slowness of 2.0 ± 0.2 s/°. A grid-search over the slowness and backazimuths suggests that the backazimuth of the scattered precursors is $275 \pm 7°$ (Figure 3.10).

To check the calibration of our array, we measure the backazimuth and slowness of the PKP_{df} phase. We observe the slowness to be 2.6 ± 0.3 s/°. This is significantly larger (by about 0.7 s/°) than the theoretical slowness of 1.9 s/°, suggesting that local structure (e.g., dipping sediment layers) may be biasing our precursor measurements towards larger slownesses. The observed backazimuth of PKP_{df} is $300 \pm 10°$, which is in agreement with the theoretical backazimuth of 305°. Measuring the slowness of the later arriving phases PP and SKS confirm that our array biases the slowness of these phases, so we apply a correction of -0.5

s/° to the measurements in the previous paragraph.

Developing an ideal set of mislocation vectors for this array would require analyses of many phases from earthquakes all over the globe (e.g., *Krüger and Weber*, 1992), which is beyond the scope of this study. Despite the lack of a detailed mislocation vector, we argue that enough information is present to resolve the source–receiver ambiguity. The measured (and corrected) backazimuths and slownesses suggest that both precursors are scattered from out-of-plane heterogeneity on the receiver side. Synthetic tests with the phonon code confirm this. In addition to the backazimuth and slowness, the arrival time provides information that helps locate the depth of the scatterer. According to ray theoretical calculations, in-plane CMB scattering produces energy that arrives 18 s prior to PKP_{df}; scattering at 600 km above the CMB produces energy 5 s prior to PKP_{df}. The precursors revealed by the vespagram analysis show arrival times 12 and 6 s before PKP_{df}, suggesting that the observed energy is scattered within the deepest 600 km of the mantle. The upper limit of 600 km is a conservative bound because the scattered energy comes from out-of-plane and thus travels a greater distance. Locations and depth constraints that are more precise may be obtained by using weighted stacking methods (e.g., the F-statistic, *Frost et al.*, 2013), but even with our relatively simple analysis we are able to resolve the source–receiver ambiguity and determine that the scattered energy comes from outside the great-circle path.

We also experiment with another method relying on the cross-correlation of waveforms to obtain time-shifts (with errors) that provide optimal alignment of the precursor waveforms. After aligning the broadband waveforms on the PKP_{df} phase, we filter the seismograms between 0.25 and 2.0 Hz and set all amplitudes to zero after the theoretical PKP_{df} onset time. Then, we align the collection of precursors using a cross-correlation algorithm (e.g., *Reif et al.*, 2002). The results of this procedure are shown in Figure 3.11. From the resulting set of optimal time shifts, we can estimate the best-fitting plane wave that corresponds with the arriving energy. Weighted least-squares estimation yields a plane wave with 1.4 s/° and a backazimuth of 260°. Since these waveforms are aligned on PKP_{df} prior to cross-correlation, a correction of 1.9 s/° is added to this estimate to obtain the

absolute slowness of the precursor energy. These values are in rough agreement with those obtained from the beamforming analysis above, again suggesting that the observed precursor energy comes from out-of-plane receiver-side scattering.

We tried this technique on a variety of arrays, and we found that it works best with a relatively broad-band filter (0.25–2.0 Hz) and arrays of closely spaced stations. We found many good precursor recordings by Transportable Array (TA) stations, but in most cases the station spacing was too coarse for our methods to perform very well. The precursor waveforms need to be highly similar in order for the cross-correlation algorithm to work, and this is not the case for many of the arrays we tried. EarthScope Flexible Array stations, although generally more closely spaced than TA stations, displayed dissimilar precursor waveforms from station to station, making it difficult to constrain the origin of the scattered energy. We have not yet tried using data from the Flexible Array experiments deployed in the eastern United States, but these may yield better results given the higher-density spacing and presumably simpler local structure. We leave an exploration of these data for future work.

3.7 Discussion

3.7.1 The nature of lower-mantle scatterers

The motivation behind the research presented in this paper is to better understand the nature of small-scale heterogeneity in the lowermost mantle. Results from the frequency-dependence, spatial coherence, and array processing suggest that the lower mantle consists of a ubiquitous scattering fabric with localized strong scatterers responsible for generating high-amplitude precursors. Here we discuss the implications of our three main results.

(1) We find that H-G random media with correlation lengths of 30 km or larger produce good fits to the global stacks of PKP precursors at 0.5, 1, 2, and 4 Hz. Although the H-G model was previously proposed by *Margerin and Nolet* (2003a) to model the range dependence of precursor amplitudes at a single frequency, their focus was to increase the amount of heterogeneity at length scales

smaller than 15 km. They tested H-G models with correlation lengths of 15, 30, and 80 km and concluded that their observations could not favor any of these models over the others. Here we have confirmed that the H-G model outperforms the exponential model, but we argue that correlation lengths ≥ 30 km provide better fits to the 0.5 Hz observations. This represents an improved global constraint from the *Margerin and Nolet* (2003a) study and confirms the larger-scale lower mantle scatterers reported in regional studies of PKP precursors (*Wen and Helmberger*, 1998; *Thomas et al.*, 1999).

As things stand, it is likely that the lower-mantle heterogeneity obeys either an H-G or AM type spectrum with an arbitrarily large correlation length. In the limit where the correlation length increases to a very large value, the H-G and AM models approach a power-law form with exponents -3 and -2.6. The H-G spectrum possesses constant power-per-octave and has been associated with models of a marble-cake mantle structure resulting from convective mixing (*Batchelor*, 1959; *Antonsen and Ott*, 1991; *Agranier et al.*, 2005; *Ricard et al.*, 2014). At lowermost-mantle pressures and temperatures the shear-wave velocity contrast between basalt and harzburgite is about 2–4% (*Stixrude and Lithgow-Bertelloni*, 2012). In the upper-mantle, the shear-wave velocity contrast can be considerably larger, 10–20% (*Xu et al.*, 2008). This may explain why globally-averaged small-scale velocity perturbations in the upper mantle and lithosphere have been reported to be an order of magnitude larger than those in the lower-mantle (*Shearer and Earle*, 2004, 2008). Another plausible idea is that short-wavelength changes in the fast axis of an anisotropic fabric can scatter energy much like volumetric heterogeneity can. Such textures—either volumetric or anisotropic—may be the source of the ubiquitous PKP precursors, which have been observed in almost every region of the globe (*Hedlin and Shearer*, 2000; *Waszek et al.*, 2015).

Of course, this result relies on the assumption that ray theory is valid at 0.5 Hz for ranges as large as 142°. Close to the b-caustic (at 145°) the effect of diffraction is expected to become increasingly more important at reduced frequencies. The combined effects of diffraction and scattering are difficult to evaluate at this time because of the great computational cost in running global spectral element

simulations accurate to a period of 1 s.

(2) We observe significant large-scale lateral variations in PKP precursor amplitude. Spatially-coherent regions of strong scattering appear beneath the West Pacific, Central/North America, and East Africa. The anomalies beneath Central/North America and the West Pacific were previously noted by the *Hedlin and Shearer* (2000) study, who suggested that the strong scattering may be due to remnants of the Farallon Slab and Tethys Trench. A small area of strong scattering east of Japan is shown by *Hedlin and Shearer* (2000), but we find a much broader region of strong scattering that extends throughout much of the West Pacific. We also observe a few cases of azimuthally-dependent scattering (e.g., *Cormier*, 1999); these may be caused by anisotropic heterogeneity within the observed regions.

(3) We experiment with using various arrays of stations to constrain the slowness and backazimuth of PKP precursor energy, as has been done in some previous studies. It is likely that dense local arrays deployed to address near-surface issues may expand our coverage of scattering in the deep Earth. Although mislocation vectors may be lacking for these improvised arrays, in many cases they may be able to resolve the source–receiver ambiguity. We present an example where the array processing techniques succeeded in locating out-of-plane receiver-side scattering close to the CMB near Southern California. The fact that arrays can precisely locate the slowness and backazimuth of precursor arrivals implies that small-scale heterogeneity may be, in many cases, quite localized. If this is the case, however, one might expect some regions to be devoid of scattering. This has not been routinely observed. Expanding array coverage should help address the question of how much scattered energy comes from localized, rather than distributed, heterogeneity.

3.7.2 Future work

Although this work has focused exclusively on PKP precursors, other phases may provide additional information about small-scale lower-mantle heterogeneity. The time- and range-dependence of 1-Hz P_{diff} coda, for example, was shown to be consistent with 1% perturbations with a correlation length of 2 km

under the assumption of single scattering (*Earle and Shearer*, 2001). Since more recent studies have shown that perturbations of this magnitude are too strong (*Mancinelli and Shearer*, 2013), further research should be done to determine the range of heterogeneity spectra that can match the observed amplitudes of P_{diff} coda.

P_{diff} coda filtered at longer periods could, in principle, help constrain heterogeneity power at intermediate scales of tens to hundreds of meters. This phase is challenging to model with the phonon code because it involves both diffraction and scattering. We performed SPECFEM3D_GLOBE (*Komatitsch and Tromp*, 2002a,b; *Chaljub et al.*, 2007) simulations for 3-D Earth models with random velocity heterogeneity distributed throughout the lower mantle. Preliminary tests, however, suggest that all of the long-period (20–40 s) P_{diff} coda energy can be modeled by reasonable amounts of heterogeneity in the lithosphere and upper mantle (*Mancinelli et al.*, 2015, submitted), so unique constraints on intermediate-scale heterogeneity in the lower mantle are not likely to come from this phase.

Another scattered phase, $P' \bullet P'$, consists of out-of-plane scattered energy from various depths in the mantle (*Earle et al.*, 2011). The long time-window for this phase suggests that it can be used to characterize heterogeneity throughout the mantle (*Rost et al.*, 2015). Although some success has resulted from using array techniques on this phase (*Earle et al.*, 2011; *Rost et al.*, 2015), characterizing its globally-averaged time-, range-, and frequency-dependence has been challenging thus far due to high-amplitude signal-generated noise from the surface waves that precede this phase. Future studies of $P' \bullet P'$ should focus on using deep earthquakes and innovative stacking methods to isolate the scattered energy associated with $P'P'$.

Acknowledgements

This research was supported by National Science Foundation grant EAR-111111 and the National Science Foundation Graduate Research Fellowship Program. The facilities of IRIS Data Services, and specifically the IRIS Data Man-

agement Center, were used for access to waveforms and related metadata used in this study. IRIS Data Services are funded through the Seismological Facilities for the Advancement of Geoscience and EarthScope (SAGE) Proposal of the National Science Foundation under Cooperative Agreement EAR-1261681. Computing resources for the SPECFEM3D_GLOBE simulations were provided by the Extreme Science and Engineering Discovery Environment (XSEDE), which is supported by National Science Foundation grant number ACI-1053575.

Chapter 3, in full, has been submitted for publication of the material as it may appear in Journal of Geophysical Research – Solid Earth: Mancinelli, N. J., P. M. Shearer, and C. Thomas, On the frequency dependence and spatial coherence of PKP precursors. I was the primary investigator and author of this paper.

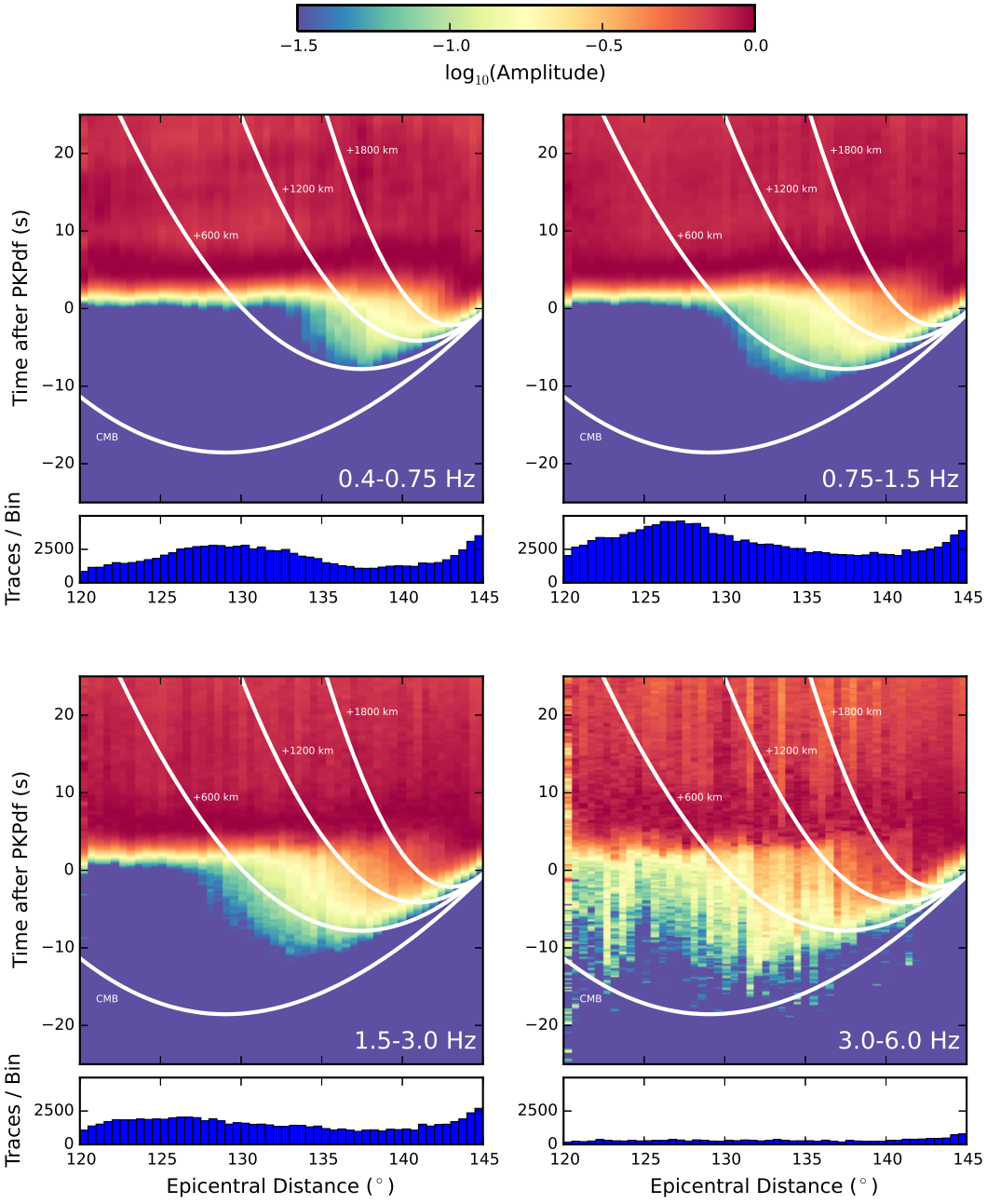

Figure 3.1: *PKP* precursor stacks, showing globally-averaged amplitude as a function of time and epicentral distance for different frequency bands. White curves delineate onset times for scattered energy at various depths in the lower mantle. Histograms show how many seismograms were used in each range bin. See *Mancinelli and Shearer* (2013) for more details.

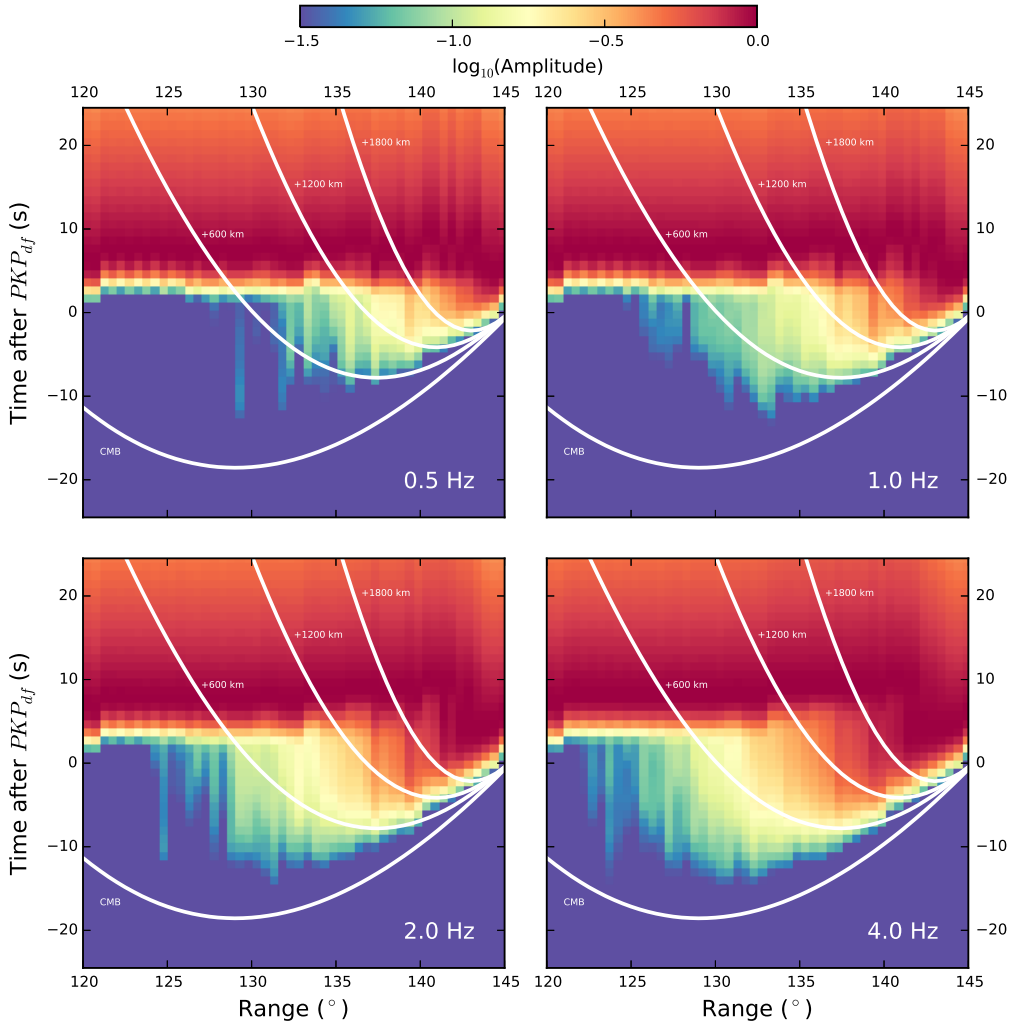

Figure 3.2: Synthetic PKP precursor amplitudes, as computed using the phonon algorithm for H-G random media with $\epsilon = 0.5\%$ and $a = 1000$ km.

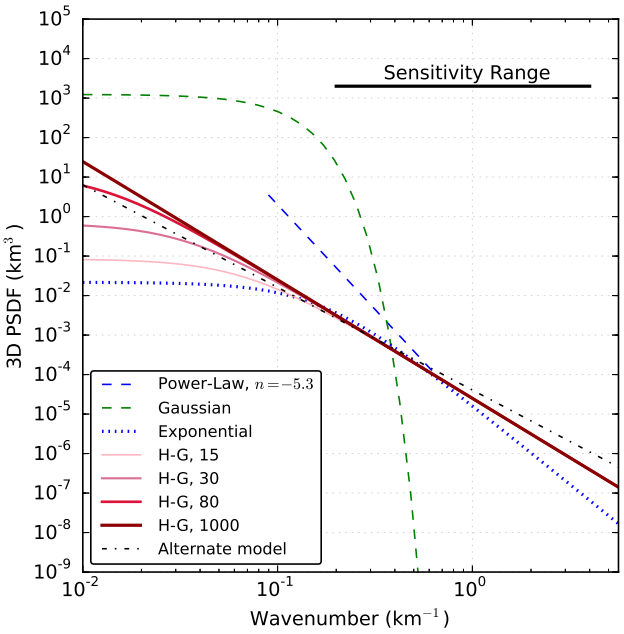

Figure 3.3: Comparison of heterogeneity spectra proposed to model PKP precursors. The blue dotted line is the exponential model published by *Mancinelli and Shearer* (2013). The dashed curves indicate results from older studies based on more band-limited observations (*Bataille and Flatte*, 1988; *Cormier*, 1995). The solid colored lines are H-G models with varying correlation lengths (15, 30, 80, and 1000 km) and $\epsilon = 0.5\%$. The dashed-dotted line is our Alternate Model (AM) with $a = 1000$ km and $\epsilon = 0.16\%$.

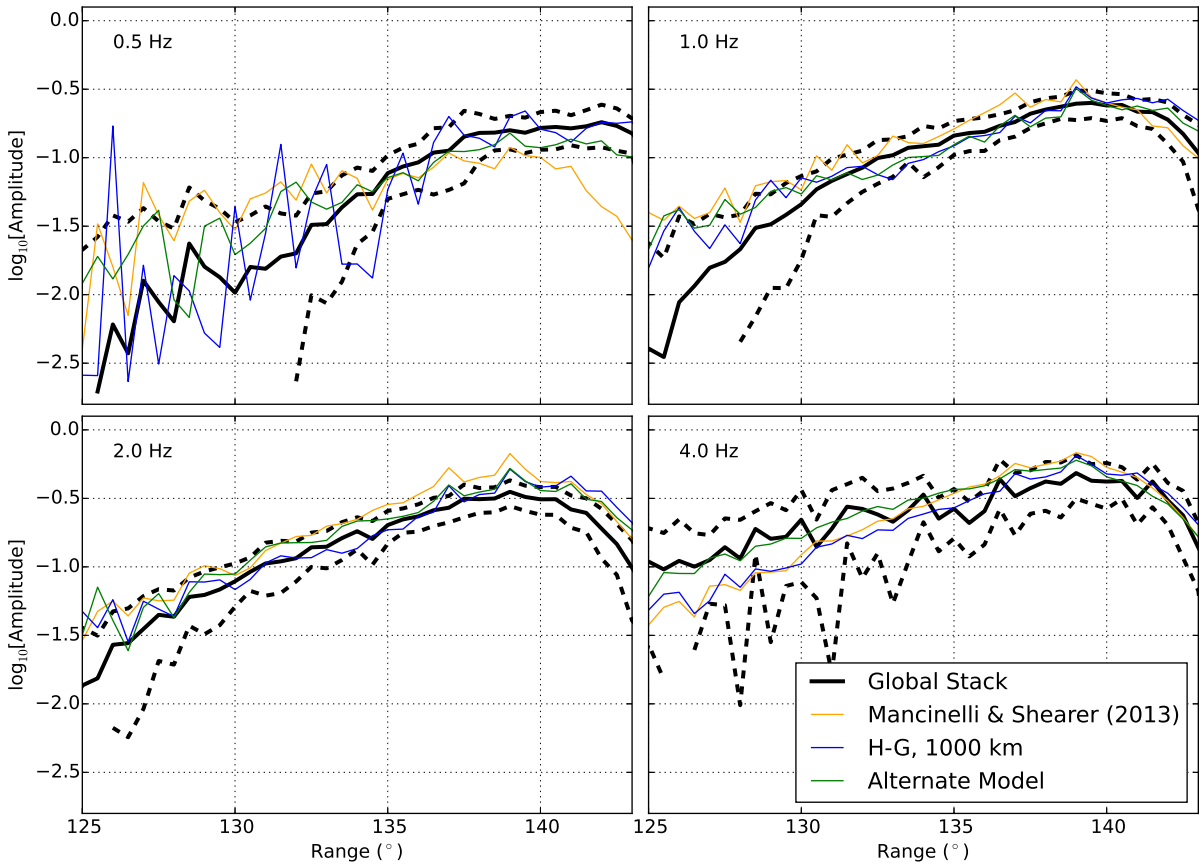

Figure 3.4: Comparison between observed (thick black curves) and predicted PKP precursor amplitudes for three different types of random media. The dashed black lines mark the 95% confidence intervals for the data stacks.

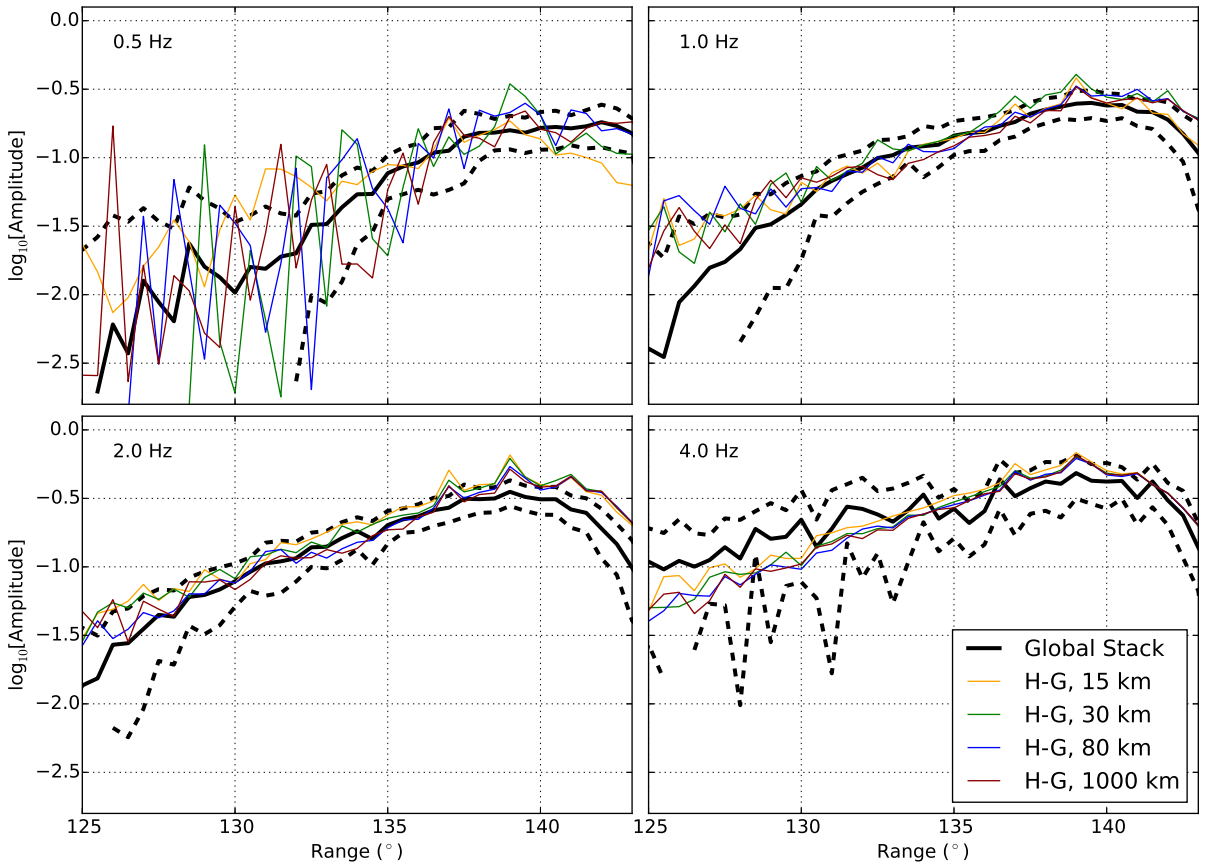

Figure 3.5: Comparison between observed (thick black curves) and predicted PKP precursor amplitudes for a variety of H-G models. The dashed black lines mark the 95% confidence intervals for the data stacks.

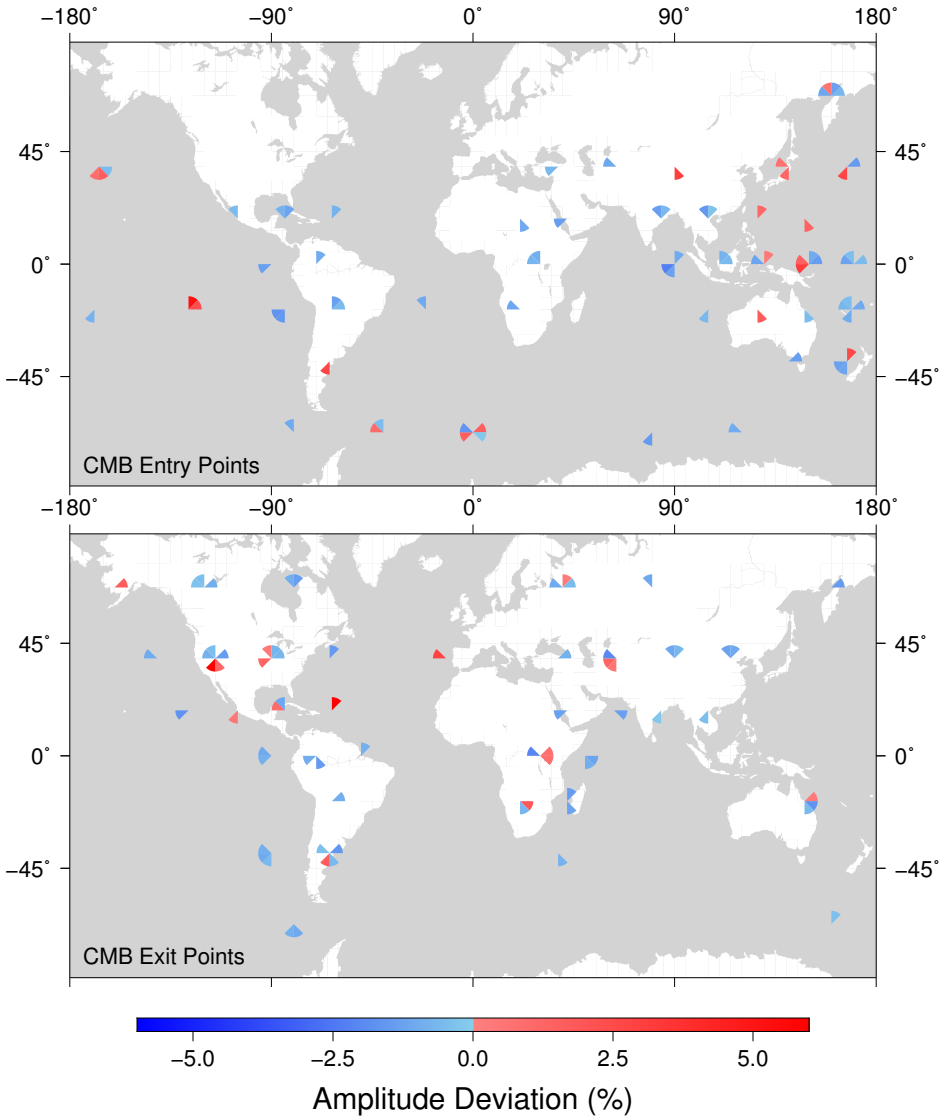

Figure 3.6: Apparent lateral variations in PKP precursor amplitude. Measurements are grouped into 20° cells based on the CMB entry (upper map) or CMB exit (lower map) points for PKP_{df}. Each cell is subdivided into 8 azimuth bins, which are plotted as colored pie wedges. The point of each wedge faces the source region (upper map) or the receiver region (lower map). For the upper map, of the 118 bins containing 5 or more traces, 74 (63%) deviate significantly (see main text) from the global average. For the lower map, of the 122 bins containing 5 or more traces, 79 (65%) deviate significantly from the global average. For clarity, only bins with significant deviations are plotted on these maps.

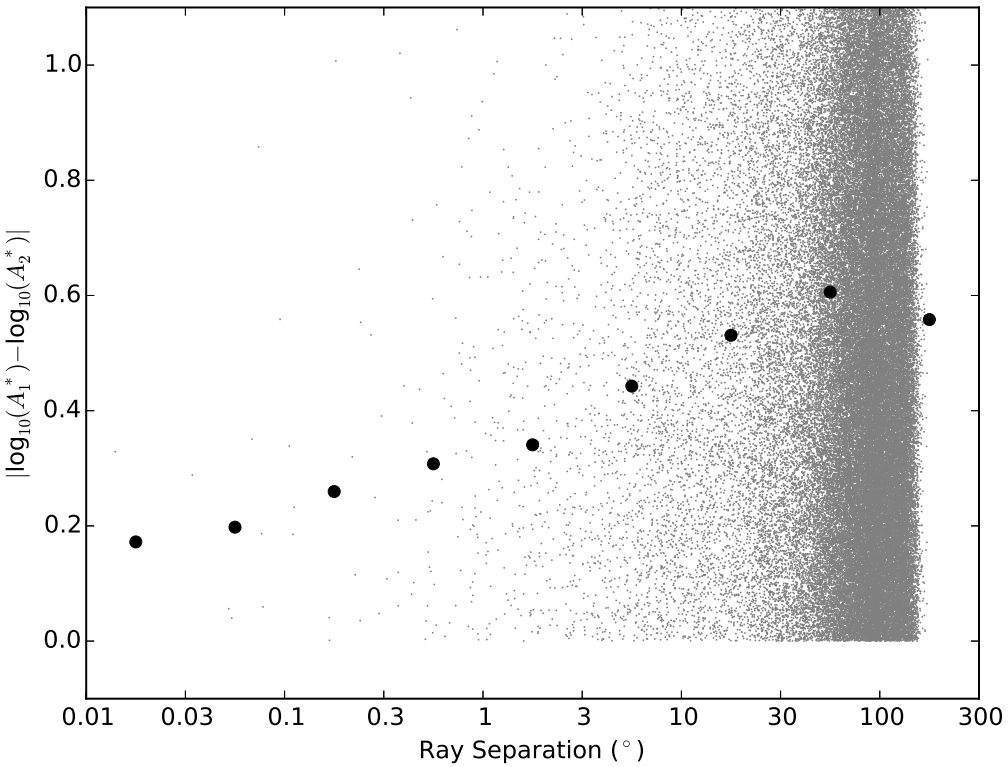

Figure 3.7: A scatterplot of absolute difference in log-amplitude versus ray separation (gray dots). Due to the large number of points, we only plot every 500^{th} one. The median for the complete set of points is plotted in each bin (black circles). We have restricted this analysis to 1-Hz seismograms recorded at ranges from 120–140°.

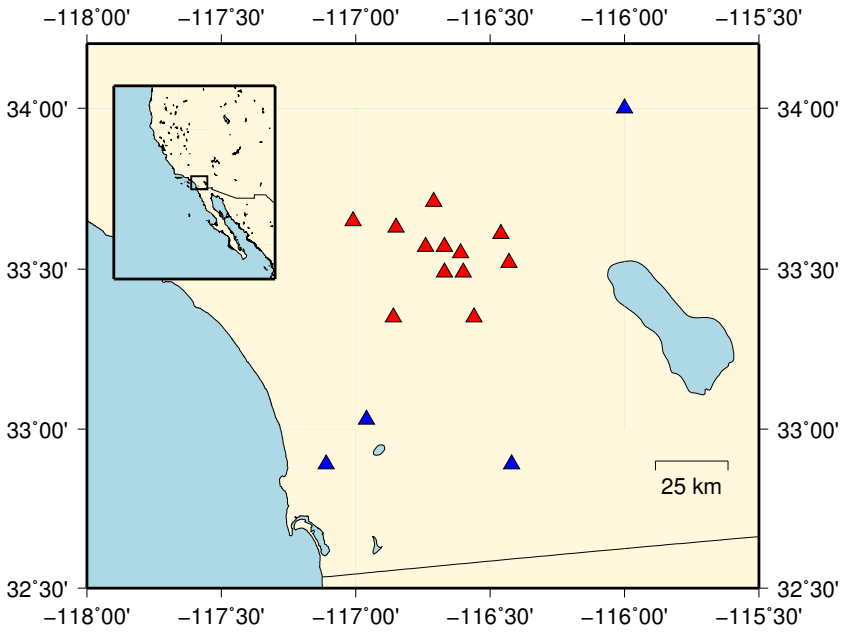

Figure 3.8: Stations used to locate the origin of PKP precursor energy from the M_W 7.6 30 September 2009 event in southern Sumatra. Red triangles (Anza Network: BZN, CRY, FRD, KNW, LVA2, PFO, RDM, SND, TRO, WMC; Southern California Seismic Network: DGR, PLM) were used in the beamforming exercise. The blue triangles (Anza Network: HWP, MONP2; Southern California Seismic Network: BEL; Transportable Array: 109C) were added for the cross-correlation analysis.

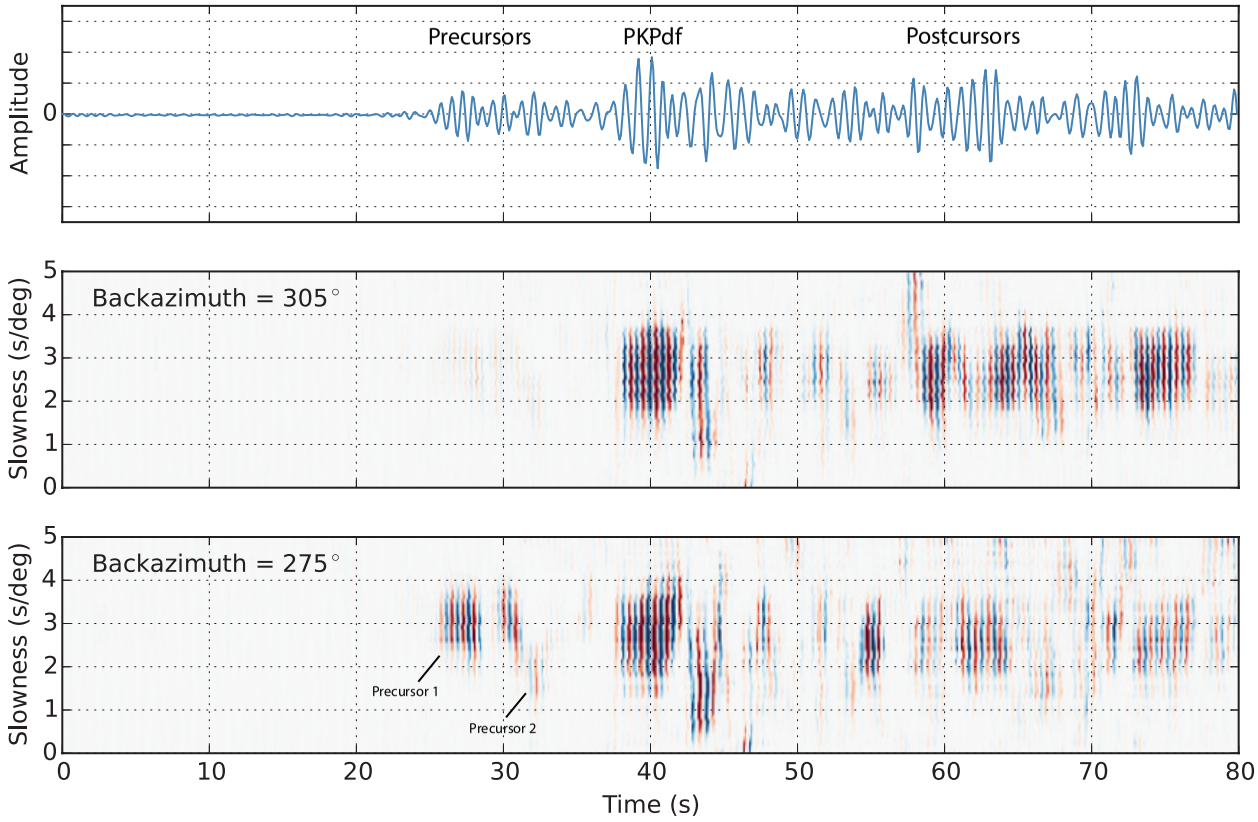

Figure 3.9: (upper) Example seismogram recorded at station PFO filtered from 1–2 Hz. (center) Fourth-root vespagram assuming the theoretical backazimuth of 305° of the recording at the array in Figure 3.8. (lower) Same as center, but assuming a backazimuth of 275°.

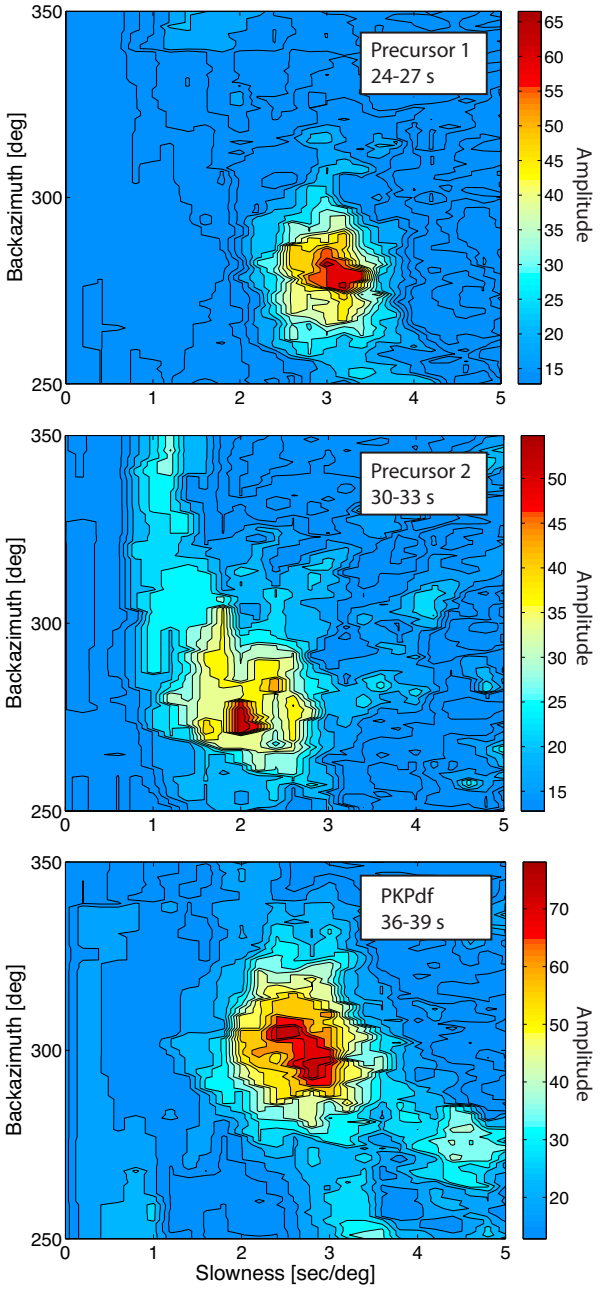

Figure 3.10: Fourth-root stacks in slowness azimuth space for 3-s windows around the earliest precursor (upper), the second precursor (center), and the PKP_{df} arrival (lower).

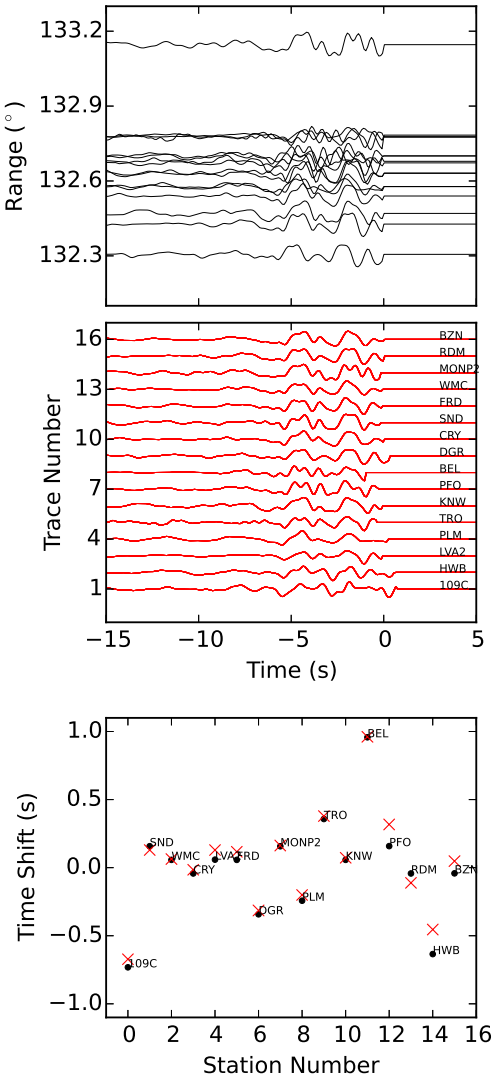

Figure 3.11: (upper) A record section of the PKP precursor waveforms filtered from 0.25–2.0 Hz. These have been aligned on the reference phase PKP_{df} which was subsequently removed. (center) Waveform alignment after the cross-correlation algorithm is applied. (lower) Observed travel-time shifts (black dots) compared with those predicted by a plane wave with slowness 1.4 s/° and a back-azimuth of 260° (red x's). Note that the waveforms were aligned on PKP_{df} prior to cross-correlation, so the PKP_{df} slowness (1.9 s/°) should be added to obtain an absolute slowness estimate.

References

Agranier, A., J. Blichert-Toft, D. Graham, V. Debaille, P. Schiano, and F. Albarède (2005), The spectra of isotopic heterogeneities along the mid-Atlantic Ridge, *Earth and Planetary Science Letters*, *238*, 96–109, doi:10.1016/j.epsl.2005.07.011.

Antonsen, T. M., and E. Ott (1991), Multifractal power spectra of passive scalars convected by chaotic fluid flows, *Physical Review A*, *44*(2).

Bataille, K., and S. M. Flatte (1988), Inhomogeneities near the core–mantle boundary inferred from scattered PKP waves recorded at the Global Digital Seismograph Network, *Journal of Geophysical Research*, *93*(B12), 15,057–15,064, doi:10.1029/JB093iB12p15057.

Batchelor, G. K. (1959), Small-scale variation of convected quantities like temperature in turbulent fluid: Part 1. General discussion and the case of small conductivity, *Journal of Fluid Mechanics*, *5*(01), 113–133, doi:10.1017/S002211205900009X.

Bhattacharyya, J., P. Shearer, and G. Masters (1993), Inner core attenuation from short-period PKP(BC) versus PKP(DF) waveforms, *Geophysical Journal International*, *114*(1), 1–11, doi:10.1111/j.1365-246X.1993.tb01461.x.

Cao, A., and B. Romanowicz (2007), Locating scatterers in the mantle using array analysis of PKP precursors from an earthquake doublet, *Earth and Planetary Science Letters*, *255*(1-2), 22–31, doi:10.1016/j.epsl.2006.12.002.

Chaljub, E., D. Komatitsch, J.-P. Vilotte, Y. Capdeville, B. Valette, and G. Festa (2007), Spectral-element analysis in seismology, *Advances in Geophysics*, *48*, 365–419.

Cleary, J. R., and R. a. W. Haddon (1972), Seismic wave scattering near the core-mantle boundary: a new interpretation of precursors to PKP, *Nature*, *240*, 549–551, doi:10.1038/240549a0.

Cormier, V. F. (1995), Time-domain modelling of $PKIKP$ precursors for constraints on the heterogeneity in the lowermost mantle, *Geophys. J. Int.*, *121*, 725–736.

Cormier, V. F. (1999), Anisotropy of heterogeneity scale lengths in the lower mantle from PKIKP precursors, *Geophysical Journal International*, *136*(2), 373–384, doi:10.1046/j.1365-246X.1999.00736.x.

Doornbos, D. J. (1978), On seismic-wave scattering by a rough core–mantle boundary, *Geophysical Journal of the Royal Astronomical Society*, *53*, 643–662.

Earle, P. S., and P. M. Shearer (2001), Distribution of fine-scale mantle heterogeneity from observations of P_{diff} coda, *Bulletin of the Seismological Society of America*, *91*(6), 1875–1881, doi:10.1785/0120000285.

Earle, P. S., S. Rost, P. M. Shearer, and C. Thomas (2011), Scattered $P'P'$ waves observed at short distances, *Bulletin of the Seismological Society of America*, *101*(6), 2843–2854, doi:10.1785/0120110157.

Frost, D. A., S. Rost, N. D. Selby, and G. W. Stuart (2013), Detection of a tall ridge at the core–mantle boundary from scattered PKP energy, *Geophysical Journal International*, *195*(1), 558–574, doi:10.1093/gji/ggt242.

Hedlin, M. A. H., and P. M. Shearer (2000), An analysis of large-scale variations in small-scale mantle heterogeneity using Global Seismographic Network recordings of precursors to PKP, *Journal of Geophysical Research*, *105*(B6), 13,655.

Hedlin, M. A. H., P. M. Shearer, and P. S. Earle (1997), Seismic evidence for small-scale heterogeneity throughout the Earth's mantle, *Nature*, *387*(6629), 145–150, doi:10.1038/387145a0.

Henyey, L. C., and J. L. Greenstein (1941), Diffuse radiation in the galaxy, *The Astrophysical Journal*, *93*, 70–83, doi:10.1086/144246.

Komatitsch, D., and J. Tromp (2002a), Spectral-element simulations of global seismic wave propagation—I. Validation, *Geophysical Journal International*, *149*(2), 390–412, doi:10.1046/j.1365-246X.2002.01653.x.

Komatitsch, D., and J. Tromp (2002b), Spectral-element simulations of global seismic wave propagation—II. Three-dimensional models, oceans, rotation, and self-gravitation, *Geophysical Journal International*, *149*(2), 390–412, doi:10.1046/j.1365-246X.2002.01653.x.

Krüger, F., and M. Weber (1992), The effect of low-velocity sediments on the mislocation vectors of the GRF array, *Geophys. J. Int.*, *108*, 387–393, doi:10.1111/j.1365-246X.1992.tb00866.x.

Mancinelli, N. J., and P. M. Shearer (2013), Reconciling discrepancies among estimates of small-scale mantle heterogeneity from PKP precursors, *Geophysical Journal International*, *195*(3), 1721–1729, doi:10.1093/gji/ggt319.

Mancinelli, N. J., P. M. Shearer, and Q. Liu (2015), Constraints on the heterogeneity spectrum of the upper mantle, *Journal of Geophysical Research*, *Submitted*.

Margerin, L., and G. Nolet (2003a), Multiple scattering of high-frequency seismic waves in the deep Earth: PKP precursor analysis and inversion for mantle granularity, *Journal of Geophysical Research*, *108*(B11), 2514.

Margerin, L., and G. Nolet (2003b), Multiple scattering of high-frequency seismic waves in the deep Earth: Modeling and numerical examples, *Journal of Geophysical Research*, *108*(B5), doi:10.1029/2002JB001974.

Przybilla, J., U. Wegler, and M. Korn (2009), Estimation of crustal scattering parameters with elastic radiative transfer theory, *Geophysical Journal International*, *178*(2), 1105–1111, doi:10.1111/j.1365-246X.2009.04204.x.

Reif, C., G. Masters, P. Shearer, and G. Laske (2002), Cluster analysis of long-period waveforms: Implications for global tomography, *EOS, Trans.*, *83*(47), 954.

Ricard, Y., S. Durand, J.-P. Montagner, and F. Chambat (2014), Is there seismic attenuation in the mantle?, *Earth and Planetary Science Letters*, *388*(0), 257–264, doi:http://dx.doi.org/10.1016/j.epsl.2013.12.008.

Rost, S., and C. Thomas (2002), Array seismology: methods and applications, *Reviews of Geophysics*, *40*(3), 1–2.

Rost, S., P. S. Earle, P. M. Shearer, D. A. Frost, and N. D. Selby (2015), Seismic Detections of Small-Scale Heterogeneities in the Deep Earth, in *The Earth's Heterogeneous Mantle*, pp. 367–390, Springer, doi:10.1007/978-3-319-15627-9.

Sato, H., M. C. Fehler, and T. Maeda (2012), *Seismic Wave Propagation and Scattering in the Heterogeneous Earth: Second Edition*, Springer.

Shearer, P. M., and P. S. Earle (2004), The global short-period wavefield modelled with a Monte Carlo seismic phonon method, *Geophysical Journal International*, *158*(3), 1103–1117, doi:10.1111/j.1365-246X.2004.02378.x.

Shearer, P. M., and P. S. Earle (2008), Observing and modeling elastic scattering in the deep Earth, *Advances in Geophysics*, *50*, 167–193.

Stammler, K. (1993), SeismicHandler—Programmable multichannel data handler for interactive and automatic processing of seismological analyses, *Computers & Geosciences*, *19*(2), 135–140, doi:10.1016/0098-3004(93)90110-Q.

Stixrude, L., and C. Lithgow-Bertelloni (2012), Geophysics of chemical heterogeneity in the mantle, *Annual Review of Earth and Planetary Sciences*, *40*, 569–595, doi:10.1146/annurev.earth.36.031207.124244.

Thomas, C., M. Weber, C. W. Wicks, and F. Scherbaum (1999), Small scatterers in the lower mantle observed at German broadband arrays, *Journal of Geophysical Research*, *104*(B7), 15,073–15,088.

Thomas, C., H. Igel, M. Weber, and F. Scherbaum (2000), Acoustic simulation of P-wave propagation in a heterogeneous spherical earth: Numerical method and application to precursor waves to PKPdf, *Geophysical Journal International*, *141*, 307–320, doi:10.1046/j.1365-246X.2000.00079.x.

Thomas, C., J. M. Kendall, and G. Helffrich (2009), Probing two low-velocity regions with PKP b-caustic amplitudes and scattering, *Geophysical Journal International*, *178*, 503–512, doi:10.1111/j.1365-246X.2009.04189.x.

Vidale, J. E., and M. A. H. Hedlin (1998), Evidence for partial melt at the core–mantle boundary north of Tonga from the strong scattering of seismic waves, *Nature*, *391*(6668), 682–685.

Waszek, L., C. Thomas, and A. Deuss (2015), PKP precursors : Implications for global scatterers, *Geophysical Research Letters*, *42*(May), 1–10, doi:10.1002/2015GL063869.1.

Wen, L., and D. V. Helmberger (1998), Ultra-Low Velocity Zones Near the Core-Mantle Boundary from Broadband PKP Precursors, *Science*, *279*(5357), 1701–1703, doi:10.1126/science.279.5357.1701.

Xu, W., C. Lithgow-Bertelloni, L. Stixrude, and J. Ritsema (2008), The effect of bulk composition and temperature on mantle seismic structure, *Earth and Planetary Science Letters*, *275*, 70–79, doi:10.1016/j.epsl.2008.08.012.

Yao, J., and L. Wen (2014), Seismic structure and ultra-low velocity zones at the base of the Earth's mantle beneath Southeast Asia, *Physics of the Earth and Planetary Interiors*, *233*, 103–111, doi:10.1016/j.pepi.2014.05.009.

Chapter 4

Constraints on the heterogeneity spectrum of Earth's upper mantle

Abstract

We constrain the heterogeneity spectrum of Earth's upper mantle at scales from a few kilometers to tens-of-thousands of kilometers using observations from high-frequency scattering, long-period scattering, and tomography. Tomography and high-frequency scattering constraints are drawn from previous studies, but constraints on mantle heterogeneity at intermediate scales (5–500 km) are lacking. To address this, we stack ∼15,000 long-period P-coda envelopes to characterize the globally-averaged scattered wavefield at periods from 5–60 s and at ranges from 50–98°. To fit these observations, we consider models of random mantle heterogeneity and compute the corresponding global wavefield using both a ray theoretical "seismic particle" approach and full spectral element simulations. Von Kármán random media distributed throughout the uppermost 600 km of the mantle with $a = 2000$ km, $\epsilon = 10\%$, and $\kappa = 0.05$ provide a good fit to the time-, range-, and frequency-dependence of the stacks, although there is a tradeoff between ϵ and the thickness of the assumed scattering layer. This random media model also fits previously published 1-Hz stacks of P-coda and agrees with constraints on long-wavelength structure from tomography. Finally, we explore geodynamically plausible scenarios

that might be responsible for the rms and fall-off rate of the proposed spectrum, including a self-similar mixture of basalt and harzburgite.

4.1 Introduction

Seismic tomography has imaged the large-scale structure of the mantle and seismic scattering studies have constrained the strength of mantle heterogeneity at very short length scales, but the full heterogeneity spectrum of the mantle has not yet been resolved. In particular, there is a sizable gap in our knowledge of mantle heterogeneity at intermediate scale lengths between about 5 and 500 km. Gaining a more complete understanding of mantle heterogeneity at all scales is essential to addressing key questions about Earth's history and dynamics, such as: What is the nature of mantle convection? Can geochemical reservoirs persist throughout geologic time? What is the ultimate fate of subducting slabs?

Over the past decades, global seismic tomography has made great progress toward constraining both the amplitude and location of large-scale lateral velocity perturbations in seismic velocities throughout Earth's mantle. Such efforts have resulted in a number of tomography models from different groups, all of which are based on regularized inversions of several types of seismic data, including: (1) travel times of direct and reflected phases, (2) normal-mode splitting measurements, (3) surface-wave dispersion measurements, and (4) full seismic waveforms. For structure within the uppermost 200 km of the mantle, most current-generation shear-wave models agree reasonably well to spherical harmonic degree 16, implying a global resolution limit of about 2400 km at these depths, although smaller features may be resolved in areas where favorable data coverage allows. In the deeper upper mantle (200–600 km) and the lowermost mantle (2500–2890 km), the models are well correlated out to degree 8. However, resolving large-scale mid-mantle structure (600–2500 km) is more challenging; in this depth range models are often uncorrelated even at the lowest degrees. See *Becker and Boschi* (2002) and *Meschede and Romanowicz* (2015a) for detailed comparisons among many recent mantle models.

Regional tomography models can resolve heterogeneities as small as a few hundred kilometers, although the exact resolution of each model depends upon several factors including (1) the types of seismic data used (surface-waves, body-waves, noise cross-correlations), (2) the inversion technique employed (matching travel times versus fitting waveforms), and (3) the locations of the receivers and sources, which are unique to every region. Again, see *Meschede and Romanowicz* (2015a) for a survey of recently published regional models.

A rigorous comparison between regional and global tomography models was initially undertaken by *Passier and Snieder* (1995), who found that regional tomography models of Europe displayed 15–30 times as much power as global models at overlapping scales (about degree 30). Later, *Chevrot et al.* (1998) emphasized the difficulty of comparing global and regional models due to fundamental differences in parameterization — the former is parameterized in terms of spherical harmonic basis functions and the latter is parameterized in terms of Fourier series — arguing that when the conversion from one basis to the other is properly done, global and regional tomography models are indeed consistent at overlapping length scales. Most recently, *Meschede and Romanowicz* (2015a) highlighted the importance of minimizing truncation effects when estimating spherical power spectra from regional models and used a multi-taper approach developed by *Wieczorek and Simons* (2005) to confirm that regional and global tomography models generally agree at overlapping length scales.

Despite the efforts of regional tomography, constraints on the amplitude of mantle structure smaller than a few hundred kilometers remain equivocal. Residuals of P-wave travel times suggest that about half of the heterogeneity power is at scales smaller than 300 km (*Gudmundsson et al.*, 1990). *Su and Dziewonski* (1992), on the other hand, used SS residuals to argue that features larger than 2500–3500 km are dominant.

High-frequency scattering studies provide compelling evidence for significant small-scale (1–10 km) heterogeneity throughout the lithosphere and upper mantle (e.g., *Sato and Fehler*, 1998; *Shearer and Earle*, 2004; *Kennett and Furumura*, 2013). The depth extent of this heterogeneity, however, is poorly resolved.

Global observations of PKP precursors suggest that small-scale heterogeneity persists throughout the lower mantle (*Hedlin et al.*, 1997), but recent studies report that these perturbations are likely smaller than those in the lithosphere and upper mantle by an order of magnitude (*Margerin and Nolet*, 2003a; *Mancinelli and Shearer*, 2013).

Taken as a whole, these studies suggest Earth's upper mantle is seismically heterogeneous at length scales spanning at least 4 orders of magnitude, from a few kilometers to tens of thousands of kilometers. However, our knowledge of the complete mantle heterogeneity spectrum is limited in two important ways: (1) We lack key constraints on global mantle heterogeneity power at intermediate scales (5–500 km), and (2) The different parameterizations used in tomography and scattering studies hamper their direct comparison. Addressing the first point will require both new observations and accurate methods for modeling the effects of intermediate-scale structures on the global seismic wavefield at arbitrary periods. Energy-conserving particle-based methods (*Margerin and Nolet*, 2003b; *Shearer and Earle*, 2004) are ideal for modeling global short-period scattering observations because of their low computational cost. It has not yet been shown, however, that these approaches are valid at periods much longer than 1 s, as ray-theoretical assumptions are expected to fail away from the infinite-frequency limit. Addressing the second point requires relating the power-per-degree on the surface of a sphere (used in most global tomography studies) with the power-spectral-density of velocity perturbations in a volume (used in most scattering studies).

Here we attempt to address these issues. Specifically, we (1) model the time, range, and frequency dependence of globally-averaged P-coda amplitudes with a single upper-mantle heterogeneity spectrum, (2) confirm the validity of a ray-theoretical modeling approach with full-wavefield spectral-element calculations, (3) relate our power-spectral-density function with large-scale constraints obtained from tomography models, and (4) suggest a geodynamically-plausible scenario for the generation of the observed upper-mantle heterogeneity spectrum.

4.2 Methods

Our study is motivated by the fact that long-period seismograms often display more energy between the main arrivals than is predicted by global tomography models (Figure 4.1). Our goal is to determine whether adding intermediate-scale (5–500 km) structure to the tomography models can produce scattering that can explain the excess observed energy. We begin by characterizing the average amplitude of scattered energy in a global dataset of seismograms at teleseismic distances. We then attempt to fit these observations by considering models of random mantle heterogeneity and computing the corresponding global wavefield using both a ray theoretical "seismic particle" approach and full spectral element simulations.

4.2.1 Characterizing scattered energy in data

We use "Standing Order for Data" (*Owens et al.*, 2004) to obtain a global dataset of broadband vertical waveforms down-sampled to 0.5 Hz from an online archive maintained by the Incorporated Research Institutions for Seismology Data Management Center (IRIS DMC). Because we are primarily interested in globally-averaged properties, we request data recorded at Global Seismic Network (GSN) stations. We obtain waveforms from 661 normal and thrust events (Mw $\geq$ 5.7, depth $\leq$ 50 km) occurring between 1 January 2010 and 17 July 2013. For reasons discussed later in the text, we exclude waveforms from events with strike-slip focal mechanisms.

To measure globally-averaged scattered energy as a function of time, range, and frequency, we construct global stacks after applying the following preprocessing steps. First, each waveform is filtered to isolate the frequency content of interest. Second, we assess the quality of each waveform by measuring the peak amplitude of the direct P-wave pulse relative to the peak amplitude of the "noise" in a window 150 to 50 s prior to the predicted P arrival. Waveforms with poor signal-to-noise ($\leq$ 10) are rejected. Third, we compute the envelope function of the time series and remove pre-event noise power from the entire trace. Fourth, we align the waveforms on the maximum amplitude occurring within $\pm$12 s of the predicted P

arrival time. Finally, we normalize the entire trace by the peak P-wave amplitude and stack each point in an appropriate time-distance bin.

Summing thousands of seismograms produces a smoothly-varying final stack that represents the globally-averaged time- and range-dependence of the scattered amplitudes. We repeat this procedure for a set of bandpass filters (5–10 s, 10–20 s, 20–40 s, 30–60 s) to assess how the scattered amplitudes depend upon frequency. Since the signal-to-noise check is applied separately at each frequency, the number of waveforms in each stack varies. The 5–10 s stack (near the microseism noise peak) has the fewest waveforms (6,371) and the 20–40 s stack has the most waveforms (17,382). Because our focus in this study is on intermediate frequencies, we do not analyze data at periods shorter than 5 s. However, later we will compare our results with the 1-Hz scattering study of *Shearer and Earle* (2004).

The specific design of the filter does not significantly affect the main result, but filters with weak sidelobes in the time-domain are preferred because they reduce contamination of the coda waves by energy leakage from the direct pulse. For consistency, it is important to use identical filters (i.e. the same sets of weights and the same algorithm) to process both the observed and synthetic waveforms.

Ideally, our global waveform stack represents Earth's globally averaged properties. However, our incomplete ray coverage, coupled with likely lateral variations in scattering strength, implies some uncertainty in this assumption. To assess this, we divide the observations into about 1,600 subsets based upon similar source-receiver geometries and apply the stacking procedure to each subset. The mean of the regionally-distinct substacks provides an estimate of the global average. Bootstrap resampling of the collection of substacks gives 2σ uncertainty bounds.

4.2.2 Modelling I – Monte Carlo method

Particle-based Monte Carlo methods provide a powerful tool for modeling seismic amplitudes at high frequencies (*Gusev and Abubakirov*, 1987; *Abubakirov and Gusev*, 1990; *Hoshiba*, 1991; *Margerin et al.*, 2000; *Bal and Moscoso*, 2000; *Shearer and Earle*, 2004). These methods treat the seismic wavefield as a sum

of discrete energy particles that individually experience random scattering events based on probabilities computed from the heterogeneity properties of the medium. These approaches naturally account for multiple-scattering and geometrical spreading effects in an energy-conserving framework. In this work, we use the Monte Carlo phonon algorithm developed by *Shearer and Earle* (2004).

Initially, we divide the mantle into three concentric scattering volumes. The first volume extends from the Earth's surface to a depth of 200 km; the second, from 200 km to 600 km; and the third, from 600 km to the core-mantle boundary. The heterogeneity in each volume is statistically parameterized by a von Kármán autocorrelation function (ACF) (*Sato and Fehler*, 1998),

$$R(r) = \frac{\epsilon^2 2^{1-\kappa}}{\Gamma(\kappa)} \left(\frac{r}{a}\right)^{\kappa} K_{\kappa}\left(\frac{r}{a}\right) \tag{4.1}$$

where r is the magnitude of the lag vector, a is the correlation length, and ϵ is the rms velocity perturbation. Γ is the gamma function and K_{κ} is the modified Bessel function of the second kind of order κ. This ACF applies to random media with isotropic properties; hence it depends only upon the magnitude, rather than the magnitude and direction, of the lag vector. The one-dimensional (1-D) Fourier-transform of Equation 4.1 gives the 1-D power-spectral-density function (PSDF)

$$P(m) = \frac{2\pi^{1/2}\Gamma(\kappa + 1/2)\,\epsilon^2 a}{\Gamma(\kappa)\left(1 + a^2 m^2\right)^{\kappa+1/2}} \tag{4.2}$$

where m is the magnitude of the wavenumber vector. Equation 4.2 resembles a power law with exponent $-2\kappa - 1$ for large wavenumbers ($am \gg 1$). The role of κ, then, is to control the relative proportion of large- to small-scale heterogeneity in this limit.

Before moving forward, a few more assumptions must be made. We assume that the fractional shear-wave velocity perturbations are equal to the fractional P-wave perturbations of the medium, and that the fractional density perturbations are proportional to the fractional velocity perturbation scaled by a factor of 80%. We assume that the the P-velocity to S-velocity ratio equals $\sqrt{3}$, which is true for a Poisson solid. Altering these parameters affects the directional scattering probabilities, as well as the probability of phase conversions between P and S.

For example, increasing the relative density perturbations increases the amount of backscatter (*Sato and Fehler*, 1998).

We assume an intrinsic attenuation model that is identical to the one favored by *Shearer and Earle* (2004), who noted that larger Q values provide better fits to high-frequency coda observations, possibly because Q models often include the effects of both scattering and intrinsic attenuation. Above a depth of 220 km, $Q_\alpha = 450$; beneath 220 km, $Q_\alpha = 2500$. For the attenuation of shear energy, we assume that $Q_\beta = (4/9)Q_\alpha$.

The code tracks individual seismic energy particles (termed *phonons*) that are sprayed over a discrete range of takeoff angles as they travel along trajectories obtained from a large table of pre-computed ray-paths for the 1-D reference model. Upon entering a scattering volume, a phonon is assigned a random path length — an instance of an exponentially distributed random variable whose mean is determined by the heterogeneity properties of the medium. Once the phonon travels its assigned distance it scatters in a random direction, where the directional probability is also governed by the heterogeneity properties. At this point, another random path length is generated from the distribution and the phonon travels onward. When the phonon returns to the free surface, its energy is summed in a time-distance array, and the phonon is reflected downward. As this process is repeated for a large number of phonons, the time-distance array continues to populate, eventually converging to a smooth model of the seismic-energy field. This method also handles P-to-S and S-to-P conversions and reflection/transmission effects at interfaces using a probabilistic framework. In these models, the phonons are sprayed from an isotropic source at the free surface. The S/P energy ratio is held constant at 23.4, based on theoretical results for a double-couple source averaged over all directions (*Sato*, 1984). For more details about this method, the reader is directed to *Shearer and Earle* (2004) and *Shearer and Earle* (2008).

This phonon method has been used previously to model scattered phases at frequencies near 1 Hz. In this study, however, we aim to model scattered waves at periods as long as 45 s. As a final step one must account for the broadening effects of the long-period filters used to process the waveforms. To this end, we compute

the envelope function of the filter and convolve it, in power, with the output of the phonon code. In the following section, we validate our use of the phonon method at long periods by comparing its results against spectral element calculations.

4.2.3 Modelling II - Spectral element simulations

Recent advances in computing power have made it possible to accurately simulate seismic wave-propagation in 3-D heterogeneous Earth models with full anisotropy, attenuation, and arbitrarily complex 3-D geometry (*Komatitsch and Tromp*, 2002a,b; *Chaljub et al.*, 2007; *Tromp et al.*, 2008). In particular, the SPECFEM3D_GLOBE (SEM, for short) software package (e.g., *Komatitsch et al.*, 2002) generates synthetic seismograms of global seismic waves accurate for periods from 17–500 s provided that one has access to a modest computer cluster (*Tromp et al.*, 2010). In our experience, synthetics accurate to 17 s can be computed in about 2 hours of computing time on 96 processors. We run simulations on parallel Xeon E5-2680 processors from the Texas Advanced Computing Center (TACC) Stampede system. By contrast, the particle-based modeling approach often converges to a stable solution within a few hours of computing time on a single processor, but it sacrifices phase information, generating only seismic energy envelopes. SEM calculations, on the other hand, produce complete waveforms. Another disadvantage of the phonon approach is that it is based on geometrical ray theory and thus neglects finite-frequency effects that become increasingly relevant at long periods.

In this section, we compare results of the phonon method and SEM. First, we explain how to generate random realizations of layered mantle heterogeneity in 3-D coordinates, and discuss how to interpolate this realization to the SEM mesh. Second, we show our source-receiver distribution for the test. Finally, we compare stacks of SEM synthetics with output from the phonon code and discuss where the two models agree and disagree.

To generate random earth models, we begin in the wavenumber domain. For each element in a $501 \times 501 \times 501$ array, we set the Fourier amplitude to a value defined by the PSDF of choice and randomize the phase component. Transforming

the array into the spatial domain, we obtain a cube of random media. Assuming that a side of this cube is equal to two times the radius of Earth, each voxel has a dimension of $25 \times 25 \times 25$ km. These models, then, can roughly capture heterogeneity as small as 50 km. See Appendix 4.A for details regarding the generation of these blocks of random media.

To include depth-varying heterogeneity in our models, we generate multiple cubes of random media, each with different heterogeneity spectra. We patch together concentric spherical shells from the different cubes to obtain a model that has depth-varying properties. To avoid the sharp velocity changes created by the boundary between two different random heterogeneity models, the transition areas between the spherical shells are smoothed by removing the power above a cutoff wavenumber in the Fourier domain (Figure 4.2). Figure 4.3 shows a slice through the equator of an example random 3-D Earth model with a von Kármán PSDF. We use a trilinear interpolation scheme to assign values from our evenly spaced random model to points on the SEM mesh, whose spacing generally varies with depth.

The setup for the SEM simulation is illustrated by Figure 4.4. To obtain many independent measurements per simulation, we place 26,484 virtual sensors at distances from 50 to 130 degrees from the source, at all azimuths. We place a virtual source at the equator, and experiment with different source radiation patterns. After each simulation, the synthetics are processed and stacked using the same code that processes the real data. The SEM mesh contains 256 spectral elements along each side of the six "chunks" in the cubed sphere. Benchmarks against semi-analytical normal-mode synthetic seimograms show that this mesh is accurate to periods of ~ 17s (*Komatitsch and Tromp*, 2002a,b).

Output from the two methods is compared in Figure 4.5. We find good agreement between the two methods for the scattered energy between P and PP at ranges from 50–96°. The agreement is best for isotropic, normal, and thrust sources. For strike-slip sources, however, the SEM synthetics have codas which are much more energetic than those modeled by the phonon code. This is likely due to the radiation pattern. For strike-slip events, the steep takeoff angles of

teleseismic P-waves means that they originate near a node in the P-wave radiation pattern. Scattering processes redirect S-waves and P energy radiated from other parts of the focal sphere into the P nodal plane; this results in high amplitude codas relative to the direct phase. In previous works (e.g., *Shearer and Earle*, 2004), it was implicitly assumed that stacking seismograms from many events would result in a net isotropic source, but here we find that including strike-slip events may bias results. Thus we exclude strike-slip events from this study.

Although the methods agree regarding the energy between P and PP, there was a marked disagreement on the amplitude of the PKP phase (not shown) in the 20–40 s band. The source of the discrepancy is likely due to destructive interference between PKP_{cd} and PKP_{df}. If this effect persists at higher frequencies, lower-mantle heterogeneity constraints from PKP precursors should be revisited. However, such an effort would require SEM simulations accurate to 1 Hz, which is well beyond the scope of this study.

4.3 Results

Here we describe the main features of the data stacks, and the predictions of our preferred model, as plotted in Figure 4.6. In addition to the direct P arrival, surface multiples PP and PPP are clearly visible. At long ranges, the relative amplitude of PP begins to increase. This is mainly due to the decrease in the amplitude of P approaching the onset of the shadow zone at 98°. At longer periods, the pulse-width of the main arrival broadens since the width of the time-domain pulse is proportional to the reciprocal of the bandwidth (in Hertz). Our global stacks show significant energy between the main phases, most notably between P and PP, which we interpret to be scattered from volumetric heterogeneity within the mantle. This scattered energy is most notable at high-frequencies, but is distinctly non-zero even at the longest observed period (30–60 s).

Using the phonon method, we test the sensitivity of the synthetics to heterogeneity at various depths within the mantle. Ultimately we find that our data do not possess the resolution to uniquely place heterogeneity in either the lithosphere

or upper mantle, so henceforth we treat the top 600 km as a single layer, although we will discuss how the assumed thickness of this layer affects results at the end of this section. We also find that scattered energy from the lower mantle is not needed to fit these data. In fact, if one makes the lower mantle as heterogeneous as the upper mantle, our synthetics predict that more scattered energy would be seen at long ranges than is observed. This is consistent with the notion that the lower mantle is much less heterogeneous than the upper mantle and lithosphere. Adding the weak amount of lower-mantle scattering required by PKP precursor results (*Margerin and Nolet*, 2003a; *Mancinelli and Shearer*, 2013) has a negligible effect on our results; thus for simplicity in this study we set the rms perturbations of the lower mantle to zero and focus on constraining the upper-mantle spectrum.

We find that a von Kármán PSDF (Equation 4.2) with a correlation length of 2000 km, an rms perturbation of 10%, and $\kappa = 0.05$ provides a good first-order fit to the observations at all periods. Moreover, this PSDF provides a reasonable fit to the 1-Hz P-coda stacks previously published by *Shearer and Earle* (2004) (Figure 4.7) and overlaps with long-wavelength constraints from tomography (Figure 4.8). The tomography constraints are derived from spherical harmonic spectra of the uppermost 250 km of the mantle published by *Meschede and Romanowicz* (2015a). This derivation can be found in Appendix 4.B.

Here are a few observations regarding the fitting process. Increasing κ increases the relative proportion of large- to small-scale heterogeneity, thereby affecting the frequency dependence of the synthetics. Values of κ close to zero fit the data well, but increasing κ much beyond 0.05 impedes our ability to fit the frequency dependence. Our preferred model has $\kappa = 0.05$ (rather than $\kappa = 0.01$) because the increased slope provides better agreement with the tomography results. Adjusting the correlation length has little effect on the synthetics, provided it remains greater than about 500 km. If the correlation length drops below this value, fits at the longest periods begin to degrade. Increasing the rms perturbation increases the amplitude of scattered energy, but not necessarily in a linear fashion. These models generally involve multiple scattering, having mean-free-paths ranging from about 7–500 km for our preferred spectrum (exact values depend on

frequency and depth, see Table 4.1). Due to our large choice of a (which is required to match the large-scale structure in tomography), most scattering events do not redirect energy far from the original direction of propagation. In media where forward-scattering is dominant, a more appropriate quantity for comparison is the transport (i.e. momentum transfer) mean-free-path (e.g., *Przybilla et al.*, 2009), which corrects for anisotropic scattering probabilities. Our preferred phonon models have transport mean-free-paths for P energy in the upper mantle of about 2,500, 4,600, 8,700, and 13,000 km for periods of 7.5, 15, 30, and 45 s, respectively. At 1 Hz, the transport mean-free-path is ~ 410 km.

An alternate spectrum (Alternate A) with $a = 500$, $\epsilon = 18\%$, and $\kappa = 0.01$ fits the scattering observations just as well, but does not overlap with the tomography constraints at small wavenumbers. More complicated spectra (e.g., Alternate B) fit the scattering observations well and plot within the bounds allowed by tomography. At present, it is difficult to distinguish among these more complicated heterogeneity spectra, but comparisons with phase velocity maps may improve constraints at long wavelengths. It may seem surprising that ϵ changes quite dramatically for seemingly small changes in κ. As κ approaches zero increasingly more heterogeneity is added at infinitesimal scales. Despite their differing ϵ values, Alternate A and the preferred spectrum plot almost on top of each other in Figure 4.8.

We investigate the possibility of lateral variations in scattering strength in our observations by employing the following procedure. For each data trace, we measure the mean amplitude of the P-coda in a window from 50–100 s after the peak P amplitude. The measurements are then divided into 1,637 groups based on ray-path endpoints. In each regional group, bootstrap resampling with replacement is applied to determine the mean and variance of the coda amplitude. After discarding the groups with few (< 5) or wildly variable (errorbars wider than 0.15) measurements, we sort the remaining ~ 350 groups from smallest to largest mean amplitude, and plot their spatial distribution.

We find significant lateral variations of the scattered energy at all periods of observation except the longest (30–60 s). Paths traversing the continents tend

to result in weaker-than-average codas, whereas paths traversing the oceans (in particular subduction zones) tend to display the opposite effect. This pattern is shown, for example, in the 10–20 s band of observation (Figure 4.9). Similar patterns are observed for the 5–10 s and 20–40 s bands.

To fit the subset of data from the 25% of the paths with the smallest scattered amplitudes, ϵ of the preferred spectrum needs to be reduced from 10% to 6%. Likewise, fitting the subset of data from the largest 25%, ϵ needs to be increased only slightly, from 10% to 11%. Spectra that match the regional substacks displaying either the strongest or weakest coda amplitudes are plotted in Figure 4.8.

Before moving on, we should note the linear tradeoff between ϵ and the assumed thickness of the upper mantle scattering layer. That is, halving the assumed thickness of the scattering layer requires a doubling of ϵ in order to achieve similar fits. This is only true down to a certain thickness. Below a thickness of 100 km, the synthetics are unable to match the observed time-dependence for any ϵ.

4.4 Discussion

In the previous section we proposed a single mantle heterogeneity spectrum that simultaneously explains, to first-order, (1) the long-period constraints presented in this study, (2) the high-frequency constraints reported previously (*Shearer and Earle*, 2004), (3) and constraints from global and regional tomography. Here we discuss geodynamically plausible scenarios for the generation of the heterogeneity observed at scales from 5–800 km.

Nearly 30 years ago, it was suggested that the upper mantle might contain elongated strips of subducted lithosphere that have been stretched and folded to small scales by convective strains (*Allègre and Turcotte*, 1986). This so-called marble-cake mantle contains heterogeneity at many scales, likely possessing a power-law spectrum with an exponent of -1 (*Batchelor*, 1959; *Antonsen and Ott*, 1991; *Agranier et al.*, 2005; *Ricard et al.*, 2014). The two primary components of this mixture would be basalt and harzburgite. (Basalt undergoes a phase change to eclogite at depth. For the purposes of this paper, "basalt" refers to both of these

phases.) Although the seismic velocities of these compositions vary with depth, they differ from each other by about 10% when averaged over the uppermost 800 km of the mantle (*Xu et al.*, 2008). Figure 4.10 illustrates the textures associated with self-similar mixtures of basalt and harzburgite.

In Figure 4.11, we plot spectra for various basalt-harzburgite mixtures. First, assuming that mixing occurs only at wavelengths between 5 and 800 km, we vary the basalt fraction of the mantle (10%, 25%, 50%). Unsurprisingly, the 50–50 mixture produces the greatest rms scattering, but it is not large enough to match the preferred spectrum for the paths with the strongest codas. Second, we vary the minimum wavelength at which mixing occurs, assuming that the mantle is 50% basalt. We find that mixing down to the centimeter or meter scale significantly reduces the rms of the spectrum. If a basalt–harzburgite mixture is indeed responsible for the scattered energy in P-coda, this result implies that the mixing does not occur at scales much smaller than a kilometer. This is contrary to the notion that a marble-cake texture persists to the centimeter scale, at which point chemical diffusion homogenizes the mantle (*Kellogg and Turcotte*, 1987).

Another factor that may affect the velocity contrast between basalt and harzburgite is the presence of water. If basalt and harzburgite are fully hydrated, the contrast may increase from 10% to 20% or even 30% in the uppermost 185 km of the mantle in the vicinity of low temperature subduction zones (*Hacker*, 2003). Such an effect may contribute to the lateral variations in scattering strength discussed in the previous section.

Earlier we noted a tradeoff between the thickness of the assumed scattering layer and the value of ϵ required to match the amplitude of the scattered energy. Figure 4.12 shows the seismic velocity contrast between two components that would be required to match the observations. A scattering layer 100-km thick, for example, would require a velocity contrast of 45% between compositions. More reasonable velocity contrasts are compatible with thicker scattering layers, such as the 600-km thick one we have assumed throughout much of this study.

Of course, it is possible that scattering is stronger in the crust and lithosphere than in the underlying upper mantle due to compositional heterogeneity

with stronger velocity contrasts than our assumed 10%. The presence of such a strong shallow scattering zone would reduce the scattering required at deeper depths in our model, but unfortunately we lack the depth resolution to test this idea.

We can, however, place this result within the context of the numerous studies that have used high-frequency S-wave envelopes to estimate the scattering properties of the lithosphere. At 1 Hz, regional studies typically suggest lithospheric mean-free-paths around 150 km (e.g., Japan, *Hoshiba*, 1993), although depending on the region this value can be as low as 28 km (Northern Greece, *Hatzidimitriou* (1994)) and as high as 1000 km (Germany, *Sens-Schönfelder and Wegler* (2006)). Our preferred spectrum has a transport mean-free-path of 330 km for 1-Hz S energy in the lithosphere, which is within the range of previously reported values. Our spectrum also predicts an increase in g_0 (reciprocal of the mean-free-path) with increasing frequency between 1 and 10 Hz. While some regional S-coda studies (e.g., *Fehler et al.*, 1992; *Przybilla et al.*, 2009) agree with this trend, a majority show a constant or decreasing g_0 with frequency (e.g., *Hoshiba*, 1993; *Giampiccolo et al.*, 2006).

Another important question is whether anisotropic scattering plays an important role in this problem. *Kawakatsu et al.* (2009) proposed horizontal melt-rich bands beneath the lithosphere-asthenosphere boundary; whereas *Kennett and Furumura* (2013) invoked horizontally elongated heterogeneities throughout the lithosphere and asthenosphere to model the codas of Po and So. The presence of intrinsic anisotropy in seismic wavespeed may also be relevant. Varying orientations of olivine might provide a viable way to scatter enough energy, as the velocity difference between the fast and slow axes of olivine is on the order of 10%.

Thus far we have focused on how compositional variations might shape the observed spectrum, but lateral variations in temperature also play a role, especially at long wavelengths. Large scale variations in the uppermost mantle are dominated by the thermal differences between continents and oceans, i.e. warm, seismically-slow spreading ridges versus cold, seismically-fast cratons. At scales of $\sim$ 10 km, the heterogeneity is most likely compositional because small-scale tem-

perature perturbations quickly diffuse away. Thus, the intermediate scales may represent a transition region where both thermal and compositional variations give significant contributions to observed perturbations in seismic velocity. This, perhaps, is an overly simplistic view, as it has been argued that large-scale variations in both temperature and composition are required to satisfy gravity observations (*Deschamps et al.*, 2002).

In the future, extending these results to shorter ranges may help resolve the depth extent of scattering. Modeling scattered regional phases such as *Pn*- and *Sn*-coda (e.g. *Tittgemeyer et al.*, 1996) may facilitate comparisons with local and regional coda studies and improve constraints on heterogeneity in the uppermost mantle.

Scattering of surface-wave energy may also contribute to our understanding of intermediate-scale structure in the upper mantle. Incoherent long-period ($\sim$ 100 s) energy following the fundamental-mode surface waves can be modeled by invoking self-similar small-scale velocity perturbations throughout the mantle (*Meschede and Romanowicz*, 2015b). More events should be analyzed in order to obtain quantitative global constraints, as these will be important in confirming or refining our proposed spectrum.

Acknowledgements

This research was supported by National Science Foundation grant EAR-111111 and the National Science Foundation Graduate Research Fellowship Program. Qinya Liu was supported by the Discovery Grants of the Natural Sciences and Engineering Research Council of Canada (NSERC, No. 487237). The facilities of IRIS Data Services, and specifically the IRIS Data Management Center, were used for access to waveforms and related metadata used in this study. IRIS Data Services are funded through the Seismological Facilities for the Advancement of Geoscience and EarthScope (SAGE) Proposal of the National Science Foundation under Cooperative Agreement EAR-1261681. Computing resources for the SPECFEM3D_GLOBE simulations were provided by the Extreme Science

and Engineering Discovery Environment (XSEDE), which is supported by National Science Foundation grant number ACI-1053575. The authors would like to acknowledge Zhitu Ma for generating normal mode synthetics which helped us diagnose the cause of the discrepant PKP amplitudes.

Chapter 4, in full, has been submitted for publication of the material as it may appear in Journal of Geophysical Research – Solid Earth: Mancinelli, N. J., P. M. Shearer, and Q. Liu, Contraints on the heterogeneity spectrum of the upper mantle. I was the primary investigator and author of this paper.

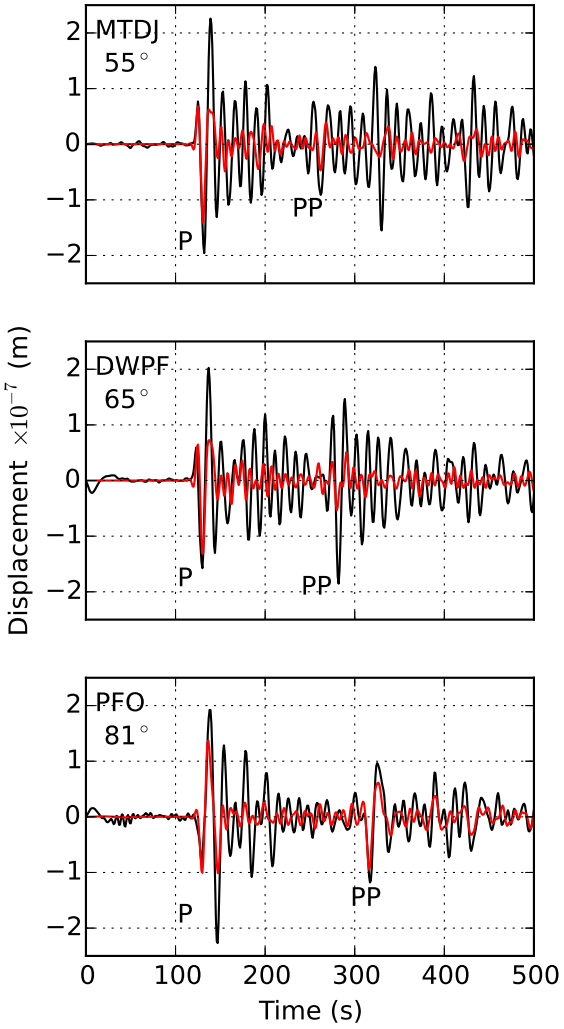

Figure 4.1: A comparison of recorded (black) and synthetic (red) seismograms for the 9 September 2010 *Mw* 6.2 earthquake near the coast of Central Chile. Synthetic seismograms were computed as part of the Global Shake Movie project (*Tromp et al.*, 2010) using 3-D velocity model S362ANI (*Kustowski et al.*, 2008). Both the data and synthetics have been filtered from 20–40 s.

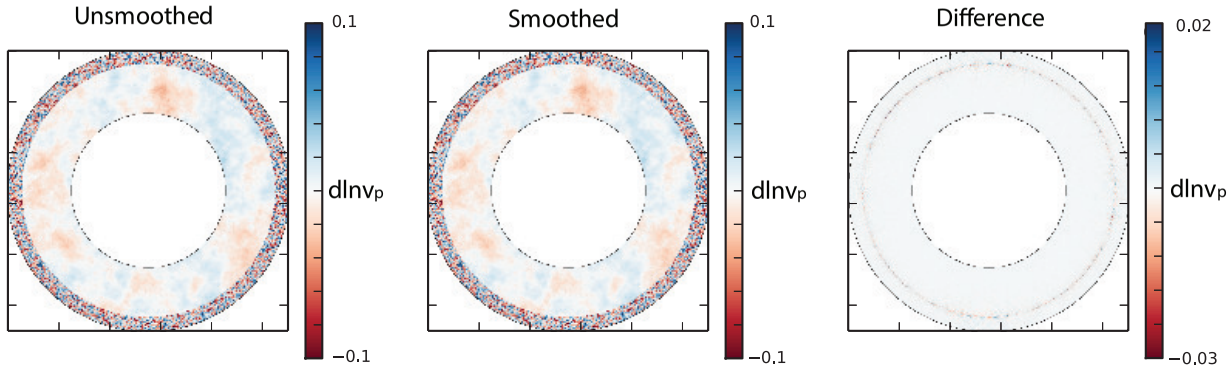

Figure 4.2: Illustration of the smoothing procedure. This random heterogeneity model has strong small-scale heterogeneity in the upper mantle and weak large-scale heterogeneity in the lower mantle. The transition between the two layers has been smoothed in the wavenumber domain by suppressing all structure with a wavelength smaller than 60 km.

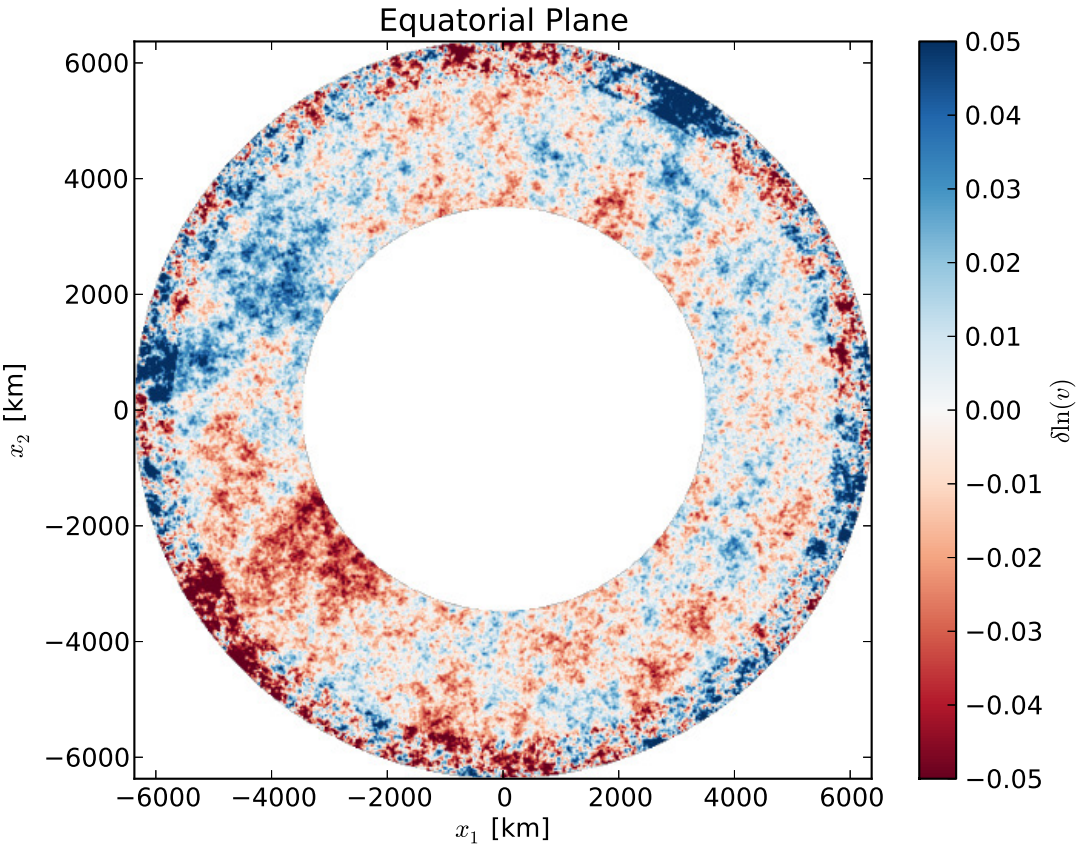

Figure 4.3: Cross-section through an example 3D mantle model with random heterogeneity. The mantle is divided into two layers. The upper mantle—600 km thick— has stronger heterogeneity than the lower mantle. The heterogeneity in both the upper and lower mantle layers are random realizations of a Von Kármán autocorrelation function.

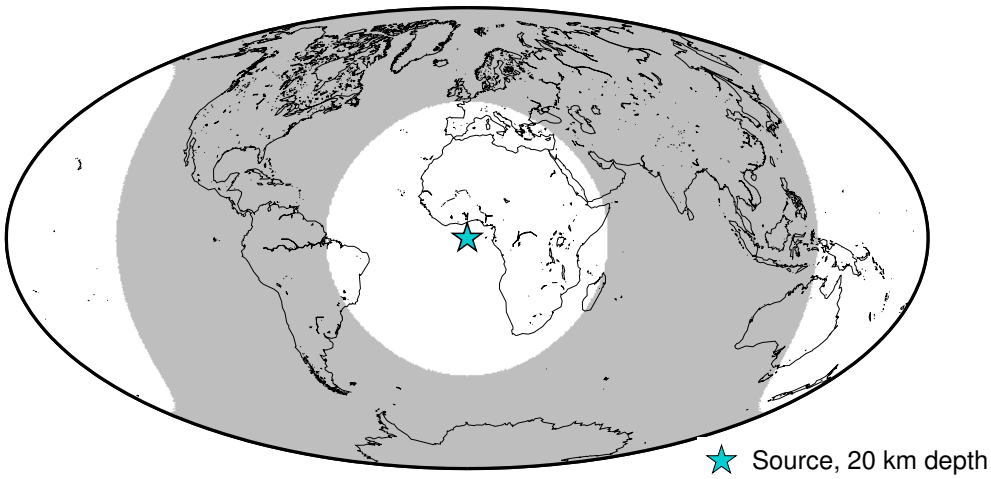

Figure 4.4: SEM model setup. 26,484 receivers are located in the gray region (50-130° range) at $\sim 1°$ spacing. The source is placed at the intersection of the equator and the prime meridian, at a depth of 20 km.

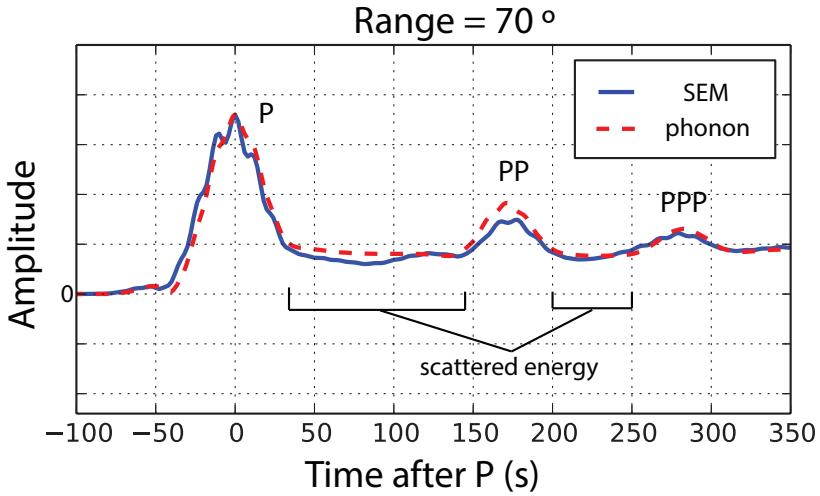

Figure 4.5: A comparison between the phonon and SEM methods for P-coda. The SEM synthetics were computed for a thrust source. They were filtered from 20–40s before stacking. The phonon code was run at 30s. The output was convolved, in power, with the filter wavelet used to postprocess the SEM synthetics.

Figure 4.6: Time and range dependence of P-coda filtered from 5–10s (upper-left), 10–20s (upper-right), 20–40s (lower-left), and 30–60s (lower-right). Data are plotted in gray; 95% confidence bounds obtained by regional bootstrapping are shown by thin black curves. The amplitudes predicted by the phonon code for the preferred random heterogeneity model are shown by dashed red curves. The phonon models were run at 7.5s (upper-left), 15s (upper-right), 30s (lower-left), and 45s (lower-right).

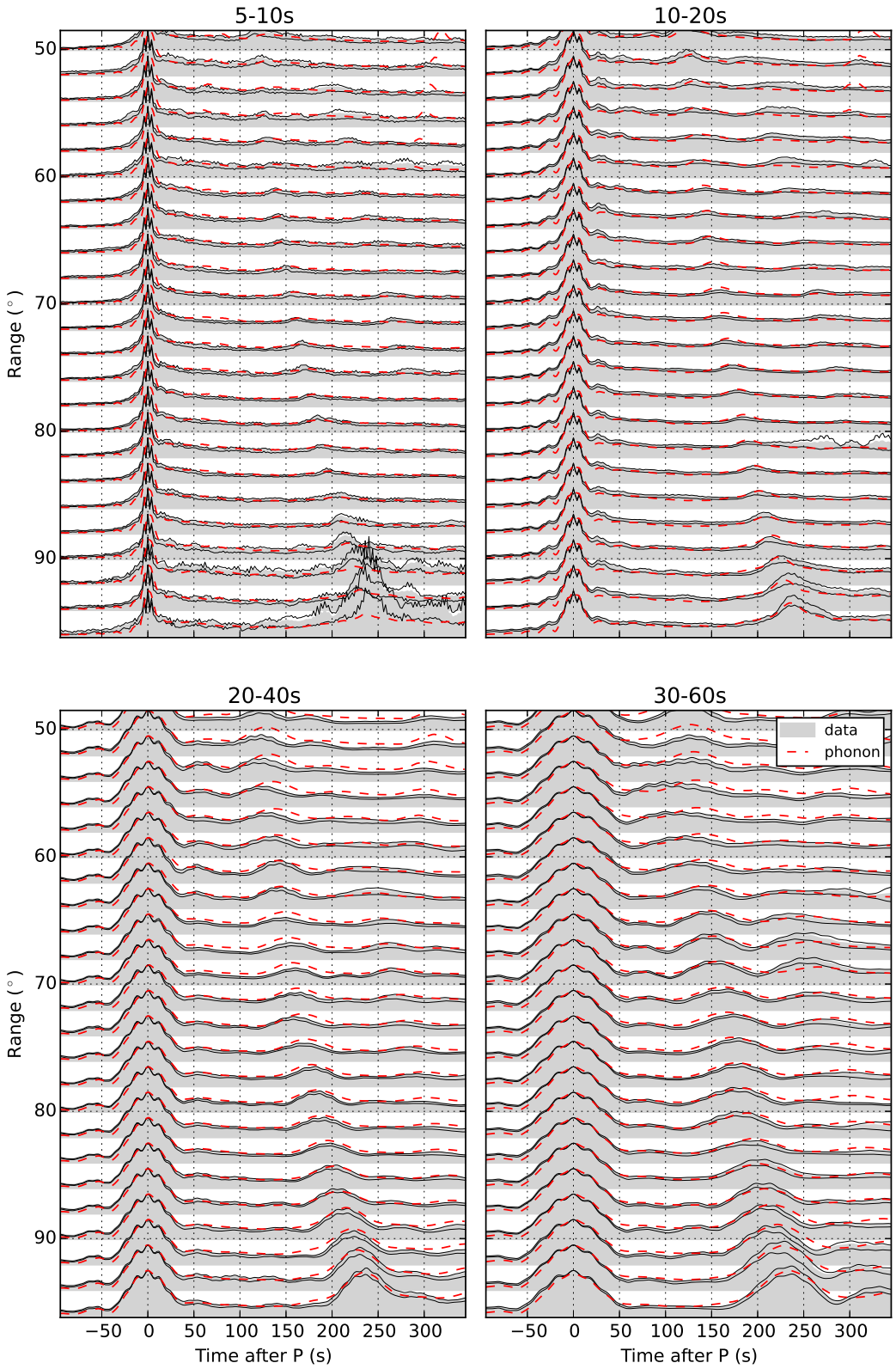
5-10s
10-20s
20-40s
30-60s
Range (°)
50
60
70
80
90
data
phonon
−50
0
50
100
150
200
250
300
Time after P (s)

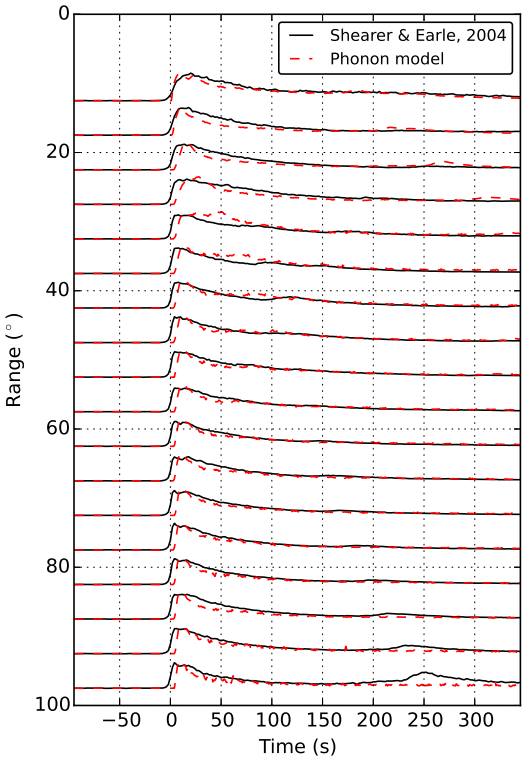

Figure 4.7: Fits of our preferred model (dashed red) to the 1-Hz data stacks published by Shearer and Earle, 2004. Phonon code run at 1s.

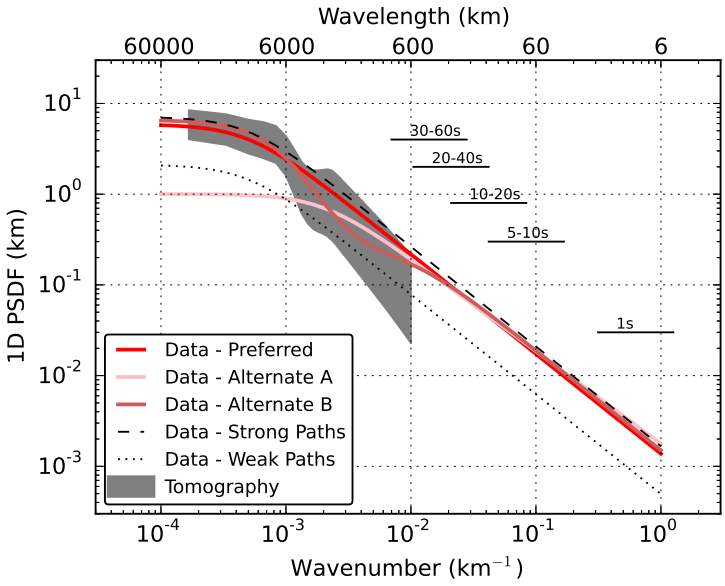

Figure 4.8: The preferred heterogeneity spectrum based on fits to scattering observations and tomography results. Two alternate spectra are plotted that fit the scattering observations almost as well. Bounds for the preferred spectrum are shown by black dashed lines. Each period of observation constrains the spectrum for a range of wavenumbers; these are shown by the black horizontal bars.

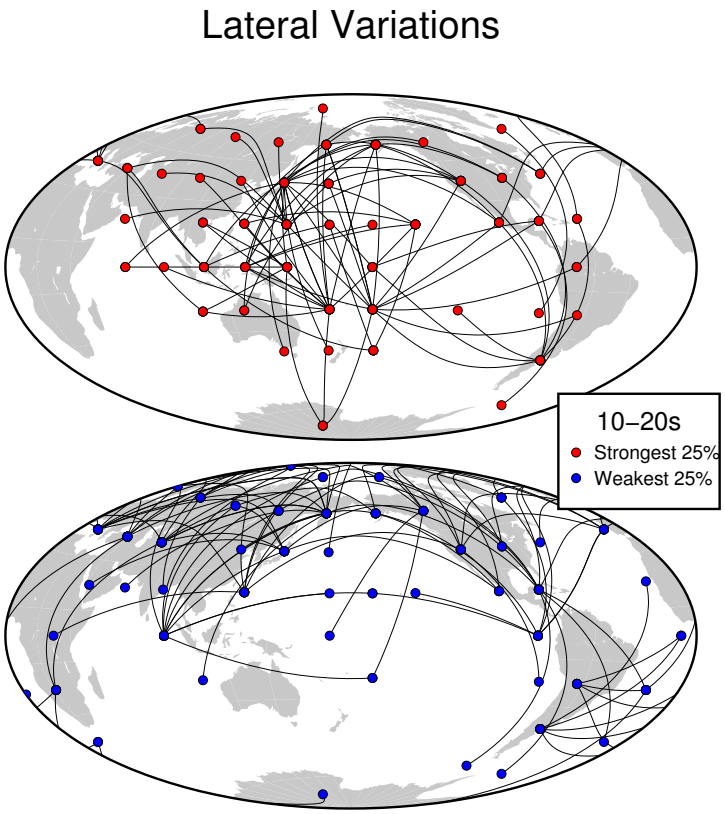

Figure 4.9: Lateral variations in P-coda amplitude when filtered from 10–20s. Data are grouped based on their ray endpoints (both source- and receiver-side). For each populated "bin" we show the associated source cell and receiver cell (colored circles) connected by a black curve. The statistical significance of these variations is confirmed by bootstrap resampling the measurements in each bin.

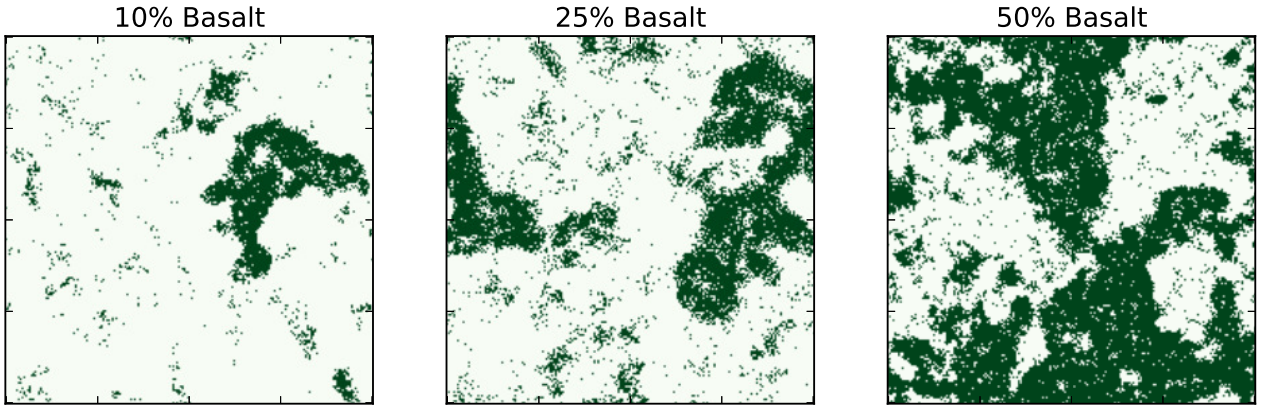

Figure 4.10: Random realizations of two-phase mixtures of basalt (dark green) and harzburgite (light green). The mixtures are self-similar so any linear length-scale may be applied to the axes.

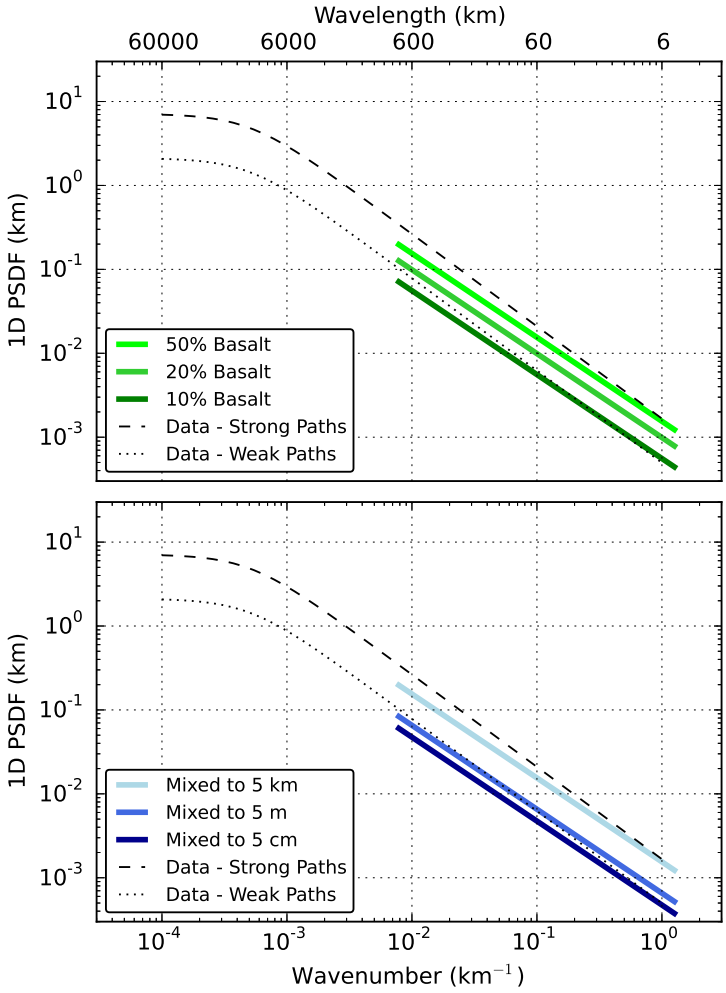

Figure 4.11: **Top**: Predicted spectra for a marble-cake mixture of basalt and harzburgite. The net power of the spectrum is affected by changing the basalt fraction of the mixture. These models assume mixing occurs primarily at wavelengths between 5 and 800 km. **Bottom**: Predicted spectra for a marble-cake mixture of basalt (50%) and harzburgite (50%). The power of the spectrum over the range of observations (5-800 km) is reduced by allowing mixing to occur at smaller scales.

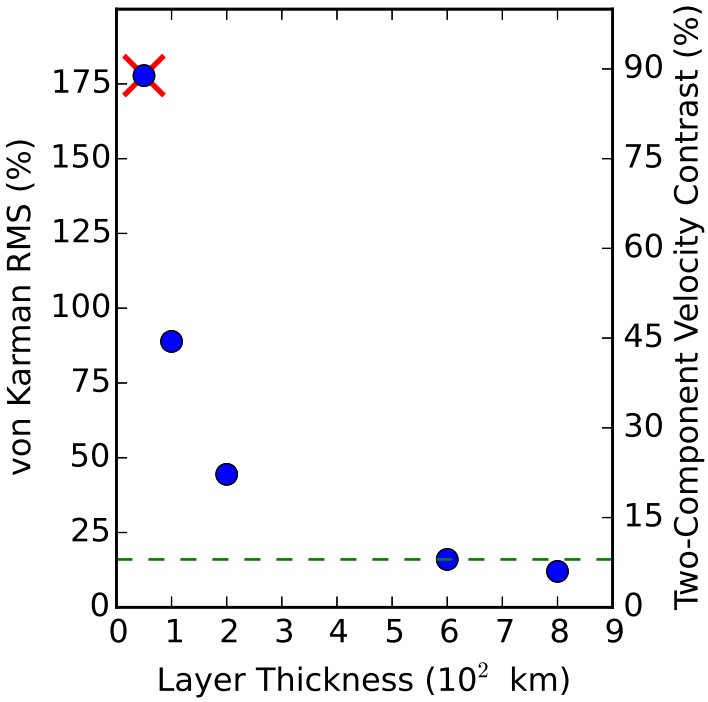

Figure 4.12: Tradeoffs between the thickness of the scattering layer and the required rms velocity perturbations. The thinnest layer tested (denoted by a red x) did not fit the data as well as the thicker layers. Assuming a two-component mixture with self-similar structure from 5–800 km, the equivalent velocity contrast between the two components can be calculated. The dashed green line represents the average velocity contrast between basalt and harzburgite throughout the upper mantle.

Table 4.1: Mean-free-paths (in km) for P energy (l_P) and S energy (l_S) for the preferred heterogeneity model. The superscript t denotes the transport mean-free-path.

	Lithosphere (0–200 km)				Upper Mantle (200–600 km)			
Period (s)	l_P	l_S	l_P^t	l_S^t	l_P	l_S	l_P^t	l_S^t
1	11	7.2	370	330	12	7.8	410	360
7.5	67	44	2,300	2,000	77	48	2,500	2,200
15	130	83	4,300	3,700	150	91	4,600	4,100
30	270	160	8,000	7,000	310	180	8,700	7,600
45	450	240	12,000	10,000	520	270	13,000	11,000

Appendices

4.A Generating cubes of random media

We take the following approach (following *Hoshiba* (2000)) to generate global random media models. The fractional velocity fluctuation of the random medium $\xi(\mathbf{x})$ by definition has zero mean and rms perturbation ϵ. Let $n(\mathbf{x})$ be the discretized version of the fractional velocity fluctuation with discretization intervals $\Delta_x, \Delta_y, \Delta_z$ along the respective x-, y-, and z-axes, and N_x, N_y, and N_z are the total number of discretization points in these orthogonal directions.

The random fluctuations $n(\mathbf{x})$ can be generated by taking the three dimensional inverse Fast Fourier Transform (FFT) of a function whose amplitude spectrum is the square root of the discretized PSDF and whose phase $\theta(\mathbf{m})$ is randomly generated from a uniform probability density in [0,2π) and satisfies $\theta(-\mathbf{m}) = -\theta(\mathbf{m})$:

$$n(\mathbf{x}) = F^{-1}\left[P(|\mathbf{m}|)^{1/2}(N_x\Delta_x N_y\Delta_y N_z\Delta_z)^{1/2}e^{i\theta(\mathbf{m})}\right] \tag{4.3}$$

Limitations imposed by computer memory make it difficult to span many scale-lengths in these models. For models shown in this work, Δ_x is typically around 25 km, meaning that power at wavelengths smaller than about 50 km cannot be represented in the discretized form. The rms perturbations in these models will always be less than or equal to the ϵ used to parameterize the continuous PSDF defined on ($-\infty$,∞). If the PSDF decays away rapidly at high wavenumbers (as is the case for a Gaussian PSDF), then

$$\epsilon^2 = \frac{1}{N_x N_y N_z}\sum_{i,j,k} n_{ijk}^2 \tag{4.4}$$

holds true. We use this relation to verify the accuracy of our FFT routine and normalization factors for the case of Gaussian random media. We can then be confident that our algorithm is correct for arbitrary random-media parameterizations, including those that have a considerable fraction of heterogeneity power at sub-grid length-scales.

4.B Comparison with tomography

We wish to relate our scattering results to long-wavelength heterogeneity power that has been constrained by global and regional inversions of seismic data. *Meschede and Romanowicz* (2015a) conduct a comprehensive analysis of global and regional tomography models, providing a constraint on heterogeneity power in the upper mantle down to scales of about 300 km (i.e. up to degree 128). *Meschede and Romanowicz* (2015a) present their results in units of logarithmic-density, or power-per-octave, $s(l)$, which is a function of spherical-harmonic degree, l. As it is not immediately obvious how to relate $s(l)$ with the power-spectral-density function that is constrained by our scattering observations, we dedicate this section to defining the different measures of heterogeneity power so that we can reliably compare one metric with another.

4.B.1 Spherical spectra

Following the notation used by *Meschede and Romanowicz* (2015a), any square-integrable function on a sphere, $f(\mathbf{r})$, can be represented by a weighted sum of the spherical-harmonic functions $Y_l^m(\mathbf{r})$, with degree l and angular order m:

$$f(\mathbf{r}) = \sum_{l=0}^{\infty} \sum_{m=-l}^{l} c_{lm} Y_l^m(\mathbf{r}) \tag{4.5}$$

with real valued c_{lm} coefficients. The spherical harmonic functions are given by

$$Y_l^m(\mathbf{r}) = \sqrt{(2l-1)\,\frac{(l-m)!}{(l+m)!}} P_{lm}(\cos\theta)\, e^{im\phi} \tag{4.6}$$

where P_{lm} is the associated Legendre function of degree l and order m, θ is the polar angle, and ϕ is the azimuthal angle. These basis functions, in addition to being orthogonal and complete, posses unit power normalization:

$$\frac{1}{4\pi} \int_{\Omega} Y_l^m(\mathbf{r}) Y_n^{k*}(\mathbf{r})\, d\Omega = \delta_{ln}\delta_{mk}. \tag{4.7}$$

Here, Ω denotes the surface of the unit sphere. The mean square velocity perturbations of the model can be obtained directly from the c_{lm} coefficients via Parseval's

Theorem

$$\frac{1}{4\pi}\int_{\Omega} f(\mathbf{r})^2\, d\Omega = \sum_l \sum_m |c_{lm}|^2 = \sum_l S_l \tag{4.8}$$

where $S_l = \sum_m |c_{lm}|^2$ is the power-per-degree. *Meschede and Romanowicz* (2015a) present their results in power-per-octave, $s(l)$, given by

$$s(l) = \log_{10}(2) l S_l \tag{4.9}$$

which has the desirable property that for self-similar media $s(l)$ plots as a constant function. Converting from power-per-octave to power-per-degree is straightforward using Equation 4.9, but before relating power-per-degree to power-spectral-density, we will precisely define the power-spectral-density function and discuss how the choice of dimensionality affects results.

4.B.2 Power spectral density

For functions defined on $\mathbb{R}^N$, the power-spectral-density function (PSD or PSDF) is the common measure of how a function's power is distributed across a range of frequencies. The PSD of a time-series with units U, to take a common example from geophysics, has units of power-per-Hertz (U^2-s). In this work, we are concerned with variations of an elastic medium in space, so the units of these spectra will be in either power-per-inverse-distance (U^2-km), power-per-inverse-area (U^2-km^2), or power-per-inverse-volume (U^2-km^3). When concerned with fractional fluctuations of a property, as is our case, U is dimensionless.

We assume that the P velocity α and the shear velocity β exhibit equal fractional fluctuations ξ. The fluctuation in density, ρ, is assumed to be proportional to ξ by a scaling factor ν:

$$\xi = d\ln\alpha = d\ln\beta = \nu\, d\ln\rho. \tag{4.10}$$

Birch's Law suggests that $\nu = 0.8$ is an appropriate value for the lithosphere, but smaller values may be appropriate for the deeper mantle. The autocorrelation function of our random medium is given by

$$R(\mathbf{x}) = \langle \xi(\mathbf{y})\xi(\mathbf{y}+\mathbf{x})\rangle \tag{4.11}$$

where the brackets denote an ensemble average. This function depends on only the lag vector $\mathbf{x}$ if the statistics are stationary with respect to space. Moreover, if the statistics are isotropic (i.e. the perturbations have an average aspect ratio of unity), R depends only on the magnitude of the lag vector, $x \equiv ||\mathbf{x}||$.

Sato and Fehler (1998) define the power spectral density function (PSDF) as the three-dimensional Fourier transform of a function $R(x)$:

$$P(\mathbf{m}) = P(m) = \iiint_{-\infty}^{\infty} R(x) e^{-i\mathbf{m}\cdot\mathbf{x}} \, d\mathbf{x}. \tag{4.12}$$

where $\mathbf{m}$ is the (angular) wavenumber vector and $m \equiv ||\mathbf{m}||$. This function is important because it directly relates to the scattering properties of the medium. To our knowledge, there is no current theory that relates heterogeneity parameterized in terms of spherical harmonics to scattering properties.

In this work, we are dealing only with isotropic, stationary media, so we will be presenting power spectral densities computed for one dimension. One can convert an N-dimensional PSDF to an M-dimensional PSDF by using the following relations:

$$R(x) = \frac{1}{(2\pi)^N} \int P_{ND}(m) e^{i\mathbf{m}\cdot\mathbf{x}} \, d^N\mathbf{m}. \tag{4.13}$$

$$P_{MD}(m) = \int R(x) e^{-i\mathbf{m}'\cdot\mathbf{x}} \, d^M\mathbf{x}. \tag{4.14}$$

where the integrals are over $\mathbb{R}^N$ and $\mathbb{R}^M$, respectively. In the second relation, $\mathbf{m}'$ is also a wavenumber vector but it may differ in dimensionality from $\mathbf{m}$.

As a note of caution, the choice of dimensionality affects the shape and units of the power spectrum. For example, the statistics of a self-similar random medium is described by a three-dimensional PSDF of power-law form with an exponent -3 which has units of distance cubed. The equivalent one-dimensional PSDF computed for a random line drawn through that same volume will have a power law exponent of -1 and have units of distance. This is an important point when comparing spectral decay rates from different studies. Similarly, spherical-spectra are subject to arbitrary choices in normalization (e.g., power-per-degree versus power-per-octave) which affect the apparent amplitude and fall-off rate of the spectrum.

4.B.3 Direct comparisons between power-per-degree and power-spectral-density

Now that power-per-degree and power-spectral-density have been explicitly defined, we move to explain how to directly compare the power-per-octave data of *Meschede and Romanowicz* (2015a) and our constrained 1-D PSDF. In other words, how do we take spherical harmonic spectra, S_l and plot them on the same axes as the PSDF?

First, we obtain the spherical autocorrelation function, $\breve{R}(\theta)$, defined over the interval [-π,π] for the model at a given radius, r, where θ represents the angle of separation at the origin between two points on the sphere. This can be done by taking a weighted sum of the Legendre polynomials, P_l:

$$\breve{R}(\theta) = \sum_l S_l P_l(\cos\theta) \tag{4.15}$$

We provide a brief proof of Equation 4.15 in the following section.

After obtaining $\breve{R}(\theta)$, we can estimate what the corresponding ACF, $R(x)$, would be by unwrapping and flattening $\breve{R}(\theta)$ onto the cartesian x-axis. This is done by scaling θ by r, which yields a function defined on the interval [-πr,πr]

$$R(x) = \begin{cases} \breve{R}\,(x/r) & \text{if } \; x \in [-\pi r, \pi r] \\ \text{undefined} & \text{otherwise.} \end{cases}$$

Since we have no interest in wavelengths longer than $2\pi r$, we need not worry about the finite domain of this function.

Third, we estimate $P(m)$ numerically by discretizing $R(x)$ into n elements with indices $j = 0, 1, ..., n-1$ evenly spaced by Δx. We take the scaled digital Fourier transform (DFT) of R_j to obtain a discretized PSDF:

$$P_k = \sum_{j=0}^{n-1} R_j \exp\left(-2\pi i \frac{jk}{n}\right)\Delta x \qquad k = 0, ..., n-1 \tag{4.16}$$

with corresponding angular wavenumbers

$$m_k = \frac{2\pi k}{n\Delta x} \qquad k = 0, ..., n-1. \tag{4.17}$$

To perform this operation, we use built-in real fast Fourier transform (RFFT) and functions provided by Scipy (www.scipy.org).

4.B.4 Proof

To prove $\breve{R}(\cos\theta) = \sum_l S_l P_l(\cos\theta)$, we begin by defining the spherical autocorrelation function as:

$$\breve{R}(\hat{r}\cdot\hat{s}) = \langle f(\hat{r}) f(\hat{s})\rangle = \langle f(\hat{r}) f(\hat{s})^*\rangle \tag{4.18}$$

The second step is justified because we are concerned with real functions on a sphere. The model $f(\hat{r})$ can be written as a weighted sum of the spherical harmonic functions:

$$f(\hat{r}) = \sum_{l,m} c_{lm} Y_l^m(\hat{r}) \tag{4.19}$$

so Equation 4.18 becomes

$$\breve{R}(\hat{r}\cdot\hat{s}) = \langle \sum_{l,m} c_{lm} Y_l^m(\hat{r}) \sum_{n,k} c_{nk}^* Y_n^k(\hat{s})^* \rangle = \sum_{l,m} \langle |c_{lm}|^2 \rangle Y_l^m(\hat{r}) Y_l^m(\hat{s})^* \tag{4.20}$$

where the second step is justified because the c_{lm} coefficients are uncorrelated for a random stationary process on a sphere. Using the spherical harmonic addition theorem, we obtain:

$$\breve{R}(\hat{r}\cdot\hat{s}) = \sum_l \langle |c_{lm}|^2 \rangle (2l+1) P_l(\hat{r}\cdot\hat{s}) = \sum_l S_l P_l(\hat{r}\cdot\hat{s}) \tag{4.21}$$

where $S_l = \sum_m |c_{lm}|^2$ or equivalenty $(2l+1)\langle |c_{lm}|^2\rangle$.

The addition theorem is given by:

$$(2l+1) P_l(\hat{s}\cdot\hat{r}) = \sum_{m=-1}^{l} Y_l^m(\hat{s}) Y_l^{m*}(\hat{r}) \tag{4.22}$$

References

Abubakirov, I., and A. Gusev (1990), Estimation of scattering properties of lithosphere of Kamchatka based on Monte-Carlo simulation of record envelope of a near earthquake, *Physics of the Earth and Planetary Interiors*, *64*(1), 52–67, doi:10.1016/0031-9201(90)90005-I.

Agranier, A., J. Blichert-Toft, D. Graham, V. Debaille, P. Schiano, and F. Albarède (2005), The spectra of isotopic heterogeneities along the mid-Atlantic Ridge, *Earth and Planetary Science Letters*, *238*, 96–109, doi:10.1016/j.epsl.2005.07.011.

Allègre, C. J., and D. L. Turcotte (1986), Implications of a two-component marble-cake mantle, *Nature*, *323*, 123–127, doi:10.1038/323123a0.

Antonsen, T. M., and E. Ott (1991), Multifractal power spectra of passive scalars convected by chaotic fluid flows, *Physical Review A*, *44*(2).

Bal, G., and M. Moscoso (2000), Polarization effects of seismic waves on the basis of radiative transport theory, *Geophysical Journal International*, *142*, 571–585.

Batchelor, G. K. (1959), Small-scale variation of convected quantities like temperature in turbulent fluid: Part 1. General discussion and the case of small conductivity, *Journal of Fluid Mechanics*, *5*(01), 113–133, doi:10.1017/S002211205900009X.

Becker, T. W., and L. Boschi (2002), A comparison of tomographic and geodynamic mantle models, *Geochemistry Geophysics Geosystems*, *3*.

Chaljub, E., D. Komatitsch, J.-P. Vilotte, Y. Capdeville, B. Valette, and G. Festa (2007), Spectral-element analysis in seismology, *Advances in Geophysics*, *48*, 365–419.

Chevrot, S., J. P. Montagner, and R. Sneider (1998), The spectrum of tomographic earth models, *Geophys. J. Int.*, *133*, 783–788.

Deschamps, F., J. Trampert, and R. K. Snieder (2002), Anomalies of temperature and iron in the uppermost mantle inferred from gravity data and tomographic models, *Physics Of The Earth And Planetary Interiors*, *129*(3-4), 245–264, doi:10.1016/S0031-9201(01)00294-1.

Fehler, M., M. Hoshiba, H. Sato, and K. Obara (1992), Separation of scattering and intrinsic attenuation for the Kanto-Tokai region, Japan, using measurements of S-wave energy versus hypocentral distance, *Geophysical Journal International*, *108*(3), 787–800, doi:10.1111/j.1365-246X.1992.tb03470.x.

Giampiccolo, E., T. Tuvè, S. Gresta, and D. Patanè (2006), *S*-waves attenuation and separation of scattering and intrinsic absorption of seismic energy in southeastern Sicily (Italy), *Geophysical Journal International*, *165*(1), 211–222, doi:10.1111/j.1365-246X.2006.02881.x.

Gudmundsson, O., J. H. Davies, and R. W. Clayton (1990), Stochastic analysis of global travel time data: Mantle heterogeneity and random errors in the ISC data, *Geophysical Journal International*, *102*, 25–43, doi:10.1111/j.1365-246X.1990.tb00528.x.

Gusev, A. A., and I. R. Abubakirov (1987), Monte-Carlo simulation of record envelope of a near earthquake, *Physics of the Earth and Planetary Interiors*, *49*(1-2), 30–6, doi:10.1016/0031-9201(87)90130-0.

Hacker, B. R. (2003), Subduction factory 1. Theoretical mineralogy, densities, seismic wave speeds, and H_2O contents, *Journal of Geophysical Research*, *108*, 1–26, doi:10.1029/2001JB001127.

Hatzidimitriou, P. M. (1994), Scattering and anelastic attenuation of seismic energy in northern Greece, *Pure and Applied Geophysics*, *143*(4), 557–601.

Hedlin, M. A. H., P. M. Shearer, and P. S. Earle (1997), Seismic evidence for small-scale heterogeneity throughout the Earth's mantle, *Nature*, *387*(6629), 145–150, doi:10.1038/387145a0.

Hoshiba, M. (1991), Simulation of multiple-scattered coda wave excitation based on the energy conservation law, *Physics of the Earth and Planetary Interiors*, *67*(1-2), 123–136, doi:10.1016/0031-9201(91)90066-Q.

Hoshiba, M. (1993), Separation of scattering attenuation and intrinsic absorption in Japan using the multiple lapse time window analysis of full seismogram envelope, *Journal of Geophysical Research*, *98*(B9), 15,809, doi:10.1029/93JB00347.

Hoshiba, M. (2000), Large fluctuation of wave amplitude produced by small fluctuation of velocity structure, *Physics of the Earth and Planetary Interiors*, *120*(3), 201–217, doi:http://dx.doi.org/10.1016/S0031-9201(99)00165-X.

Kawakatsu, H., P. Kumar, Y. Takei, M. Shinohara, T. Kanazawa, E. Araki, and K. Suyehiro (2009), Seismic evidence for sharp boundaries of oceanic plates, *Science*, *324*(April), 499–502.

Kellogg, L., and D. Turcotte (1987), Homogenization of the mantle by convective mixing and diffusion, *Earth and Planetary Science Letters*, *81*(4), 371–378, doi:10.1016/0012-821X(87)90124-5.

Kennett, B. L. N., and T. Furumura (2013), High-frequency Po/So guided waves in the oceanic lithosphere: I—long-distance propagation, *Geophysical Journal International*, *195*(3), 1862–1877, doi:10.1093/gji/ggt344.

Komatitsch, D., and J. Tromp (2002a), Spectral-element simulations of global seismic wave propagation—I. Validation, *Geophysical Journal International*, *149*(2), 390–412, doi:10.1046/j.1365-246X.2002.01653.x.

Komatitsch, D., and J. Tromp (2002b), Spectral-element simulations of global seismic wave propagation—II. Three-dimensional models, oceans, rotation, and self-gravitation, *Geophysical Journal International*, *149*(2), 390–412, doi:10.1046/j.1365-246X.2002.01653.x.

Komatitsch, D., J. Ritsema, and J. Tromp (2002), The spectral-element method, Beowulf computing, and global seismology, *Science*, *298*(5599), 1737–1742, doi:10.1126/science.1076024.

Kustowski, B., G. Ekström, and A. M. Dziewoski (2008), Anisotropic shear-wave velocity structure of the Earth's mantle: A global model, *Journal of Geophysical Research*, *113*(B6), doi:10.1029/2007JB005169.

Mancinelli, N. J., and P. M. Shearer (2013), Reconciling discrepancies among estimates of small-scale mantle heterogeneity from PKP precursors, *Geophysical Journal International*, *195*(3), 1721–1729, doi:10.1093/gji/ggt319.

Margerin, L., and G. Nolet (2003a), Multiple scattering of high-frequency seismic waves in the deep Earth: PKP precursor analysis and inversion for mantle granularity, *Journal of Geophysical Research*, *108*(B11), 2514.

Margerin, L., and G. Nolet (2003b), Multiple scattering of high-frequency seismic waves in the deep Earth: Modeling and numerical examples, *Journal of Geophysical Research: Solid Earth*, *108*(B5), doi:10.1029/2002JB001974.

Margerin, L., M. Campillo, and B. Van Tiggelen (2000), Monte Carlo simulation of multiple scattering of elastic waves, *Journal of Geophysical Research: Solid Earth*, *105*(B4), 7873–7892, doi:10.1029/1999JB900359.

Meschede, M., and B. Romanowicz (2015a), Lateral heterogeneity scales in regional and global upper mantle shear velocity models, *Geophysical Journal International*, *200*(2), 1076–1093, doi:10.1093/gji/ggu424.

Meschede, M., and B. Romanowicz (2015b), Non-stationary spherical random media and their effect on long-period mantle waves, *Geophysical Journal International*, *203*(3), 1605–1625, doi:10.1093/gji/ggv356.

Owens, T. J., H. P. Crotwell, C. Groves, and P. Oliver-Paul (2004), SOD: Standing Order for Data, *Seismological Research Letters*, *75*(4), 515–520.

Passier, M. L., and R. K. Snieder (1995), On the presence of intermediate-scale heterogeneity in the upper mantle, *Planetary and Space Science*, *123*, 817–837, doi:10.1016/0032-0633(75)90189-0.

Przybilla, J., U. Wegler, and M. Korn (2009), Estimation of crustal scattering parameters with elastic radiative transfer theory, *Geophysical Journal International*, *178*(2), 1105–1111, doi:10.1111/j.1365-246X.2009.04204.x.

Ricard, Y., S. Durand, J.-P. Montagner, and F. Chambat (2014), Is there seismic attenuation in the mantle?, *Earth and Planetary Science Letters*, *388*(0), 257–264, doi:http://dx.doi.org/10.1016/j.epsl.2013.12.008.

Sato, H. (1984), Attenuation and Envelope Formation of Three-Component Seismograms of Small Local Earthquakes in Randomly Inhomogeneous Lithosphere, *Journal of Geophysical Research*, *89*(B2), 1221–1241.

Sato, H., and M. C. Fehler (1998), *Seismic Wave Propagation and Scattering in the Heterogeneous Earth*, Springer.

Sens-Schönfelder, C., and U. Wegler (2006), Radiative transfer theory for estimation of the seismic moment, *Geophysical Journal International*, *167*(3), 1363–1372, doi:10.1111/j.1365-246X.2006.03139.x.

Shearer, P. M., and P. S. Earle (2004), The global short-period wavefield modelled with a Monte Carlo seismic phonon method, *Geophysical Journal International*, *158*(3), 1103–1117, doi:10.1111/j.1365-246X.2004.02378.x.

Shearer, P. M., and P. S. Earle (2008), Observing and modeling elastic scattering in the deep Earth, *Advances In Geophysics, Vol 50*, *50*, 167–193, doi:DOI10.1016/S0065-2687(08)00006-X.

Su, W.-j., and A. M. Dziewonski (1992), On the scale of mantle heterogeneity, *Physics of the Earth and Planetary Interiors*, *74*(1-2), 29–54, doi:10.1016/0031-9201(92)90066-5.

Tittgemeyer, M., F. Wenzel, K. Fuchsl, and T. Ryberg (1996), Wave propagation in a multiple-scattering upper mantle - observations and modelling, *Geophysical Journal International*, *127*(2), 492–502.

Tromp, J., D. Komatitsch, and Q. Liu (2008), Spectral-Element and Adjoint Methods in Seismology, *Communications in Computational Physics*, *3*(1), 1–32.

Tromp, J., D. Komatitsch, V. Hjörleifsdóttir, Q. Liu, H. Zhu, D. Peter, E. Bozdag, D. McRitchie, P. Friberg, C. Trabant, and A. Hutko (2010), Near real-time simulations of global CMT earthquakes, *Geophysical Journal International*, *183*(1), 381–389, doi:10.1111/j.1365-246X.2010.04734.x.

Wieczorek, M. a., and F. J. Simons (2005), Localized spectral analysis on the sphere, *Geophysical Journal International*, *162*(3), 655–675, doi:10.1111/j.1365-246X.2005.02687.x.

Xu, W., C. Lithgow-Bertelloni, L. Stixrude, and J. Ritsema (2008), The effect of bulk composition and temperature on mantle seismic structure, *Earth and Planetary Science Letters*, *275*, 70–79, doi:10.1016/j.epsl.2008.08.012.

Chapter 5

Evidence for a reduced velocity gradient in the lowermost outer core from the range dependence of $PKKP$ precursor amplitudes

Abstract

We stack a large global dataset of 1-Hz $PKKP$ waveforms to constrain globally-averaged properties of $PKKP$ precursors. We find that the precursor observations are better explained by scattering from core-mantle boundary (CMB) topography than by scattering from the near-surface, lower mantle, outer core, or inner core. However, as previously noted, simple models of CMB topography and standard 1D seismic velocity models fail to model the range dependence of the relative amplitude between $PKKP_{bc}$ and its precursors. We propose a new reference model with a reduced velocity gradient in the lowermost 250 km of the outer core that fits both our $PKKP_{bc}$ precursor amplitudes and constraints on absolute PKP_{bc} travel times. Our globally averaged $PKKP$ precursor observations are consistent with random CMB topography with rms variations of $\sim$440 m and a horizontal correlation length of $\sim$7 km.

5.1 Introduction

High-frequency scattered energy associated with $PKKP$—a core phase reflected from the underside of the core–mantle boundary—has been observed since the 1970s (*Doornbos*, 1974). Short-wavelength topography on the core-mantle boundary (CMB) is capable of generating precursors to $PKKP$ (*Chang and Cleary*, 1981), and global stacks of this energy have been modeled by invoking small-scale topography on the CMB (*Earle and Shearer*, 1997). However, a problem remains with this simple interpretation. *Earle and Shearer* (1997) were unable to match the range dependence displayed in the data with simple models of CMB scattering: synthetics underpredict precursor amplitudes at short ranges (80–90°) and overpredict amplitudes at long ranges (100–110°).

In this paper, we reproduce the observations of *Earle and Shearer* (1997) by stacking a global dataset of ∼16,000 high-quality $PKKP$ waveforms recorded from 1990–2013. We use a Monte Carlo seismic-particle approach (e.g., *Shearer and Earle*, 2004) to forward model the observations, and we confirm that simple models where energy is scattered by CMB topography generate precursors with a range-dependence that systematically mismatches the observations. To address the possibility of scattered energy from other regions within the Earth, we explore a broad set of models that account for these possible contributions, including scattering from the inner-core, from the lower mantle, and from the lithosphere. We find many models that excite precursory energy to $PKKP_{bc}$, but none that match the range dependence of the observations within their estimated errors.

After failing to find a scattering geometry that explains the range dependence seen in the data, we explore the possibility that changes to the underlying 1-D velocity model could provide a better fit to the $PKKP_{bc}$ precursor observations. We find that the synthetic amplitudes are sensitive to the assumed velocity profile above the inner-core. Several velocity profiles exist that improve the model fits, but many of these models are irreconcilable with observed travel times for other seismic phases. Observed PKP_{bc} travel-time residuals from *Souriau* (2015), however, do imply that standard 1-D velocity models such as $ak135$ need a increased velocity gradient about 400–550 km above the ICB and a decreased velocity gradient in

a 300-km-thick region above the ICB. We design a 1-D velocity model that fits the PKP_{bc} travel times from *Souriau* (2015), and find that this model, together with scattering from CMB topography, produces improved fits to the $PKKP_{bc}$ precursors at shorter ranges. This result supports: (1) CMB scattering as the primary cause of $PKKP_{bc}$ precursor energy, and (2) a lowermost outer core that is characterized by a change in composition or phase at an average depth of 250 km above the ICB.

5.2 Methods

5.2.1 Data stacking

We begin our analysis with a collection of 604,626 broadband vertical (i.e., BHZ) seismograms from 7,696 events occurring from 1990–2013, recorded at epicentral distances between 70° and 120°. The seismograms are windowed around $PKKP_{bc}$ and, after applying an anti-aliasing filter, downsampled to 10 Hz. We apply a stacking procedure similar to *Earle and Shearer* (1997), following the strategy outlined by *Shearer and Earle* (2008). In brief, each seismogram is filtered between 0.7 and 2.5 Hz and aligned on the ray-theoretical arrival time of $PKKP_{bc}$. If the resulting waveform exhibits a signal-to-noise amplitude ratio lower than $\sqrt{1.9}$, it is rejected from the stack. We experimented with different noise windows, but settled on a window from -140 to -80 s to be consistent with the processing method of *Earle and Shearer* (1997). If the seismogram passes the signal-to-noise test, the envelope function of the seismogram is computed and converted to power. The average pre-event noise power is subtracted from the entire trace, and the resulting time-series is summed in an appropriate range bin.

The final stack contains a total of 16,205 seismograms; note that many have been rejected due to signal-generated noise. Figure 5.1 shows the spatial coverage of these data. Although much of the Earth's surface area is represented, the coverage is far from uniform. To get a sense of how close our stack is to the true global average, we apply bootstrap resampling to regional subsets of the data. We divide the Earth's surface into 104 cells, each about 20° across. Each

seismogram is assigned two integers, i and j, that index the source and receiver cells, respectively. Of course, not all (i,j)-combinations are populated because the ray geometry of this phase is limited to a small range of epicentral distances and the source and receiver distributions are non-uniform. The number of populated substacks is between 124 and 274 depending on the particular range bin. The seismograms are grouped with others of the same (i, j)-pair. For each bootstrap sample, data are combined from a random selection of the populated groups and stacked. The mean of the 1000 bootstrap samples provides our estimate for the global average; the square-root of the variance provides an estimate of the standard error. These are plotted for each range bin in Figure 5.2.

5.2.2 Waveform modeling

To model the global stack, we use a particle-based Monte Carlo phonon algorithm. This method has been used in previous studies to model energy scattered from volumetric heterogeneity (*Shearer and Earle*, 2004; *Peng et al.*, 2008; *Mancinelli and Shearer*, 2013; *Mancinelli et al.*, 2015), but it has not yet been used to model scattering from interface topography. *Bataille and Flatté* (1988) and *Bataille et al.* (1990) derived a theory based on the Kirchhoff-Helmholtz method where the average scattered power at a given point is computed by summing scattering contributions from the entire CMB interface. Their theory suggests that (1) the scattered power scales linearly with the mean-square fluctuation of the topographic surface (provided that the perturbations are < 1 km); and (2) the scattering pattern is directly related to the two-dimensional (2-D) Fourier transform, $\Phi(\mathbf{k})$, of the topography autocorrelation function where the wavenumber vector $\mathbf{k} = \omega/\alpha\,(\hat{\mathbf{r}} - \hat{\mathbf{s}})$, and $\hat{\mathbf{r}}$ and $\hat{\mathbf{s}}$ are unit vectors describing the directions of the specular reflection and the scattered wave, respectively. More concretely, the intensity radiated by the rough surface is given by

$$I(\mathbf{k}) = A^2 R^2 ||\mathbf{k}||^2 \left[\delta(\mathbf{k}) + ||\mathbf{k}||^2 \Omega\, \Phi\,(\mathbf{k})\right] \tag{5.1}$$

where Ω depends upon geometry (*Bataille and Flatté*, 1988, equation A19), A is the amplitude of the incident wave, and R is the reflection coefficient. The total

probability that a reflected phonon scatters away from the specular direction is given by integrating the second term over all directions, i.e.,

$$P_s = ||\mathbf{k}||^2 \iint \Omega\Phi \left[||\mathbf{k}|| \left(\hat{\mathbf{r}} - \hat{\mathbf{s}}\right)\right] d\hat{\mathbf{s}}. \tag{5.2}$$

To simulate the effects of CMB topography on $PKKP$, we directly define a scattering probability, P_s, and a distribution of scattering angles (e.g., zero-mean Gaussian with width, σ). After finding a working model, we can estimate the correlation length, a, of Gaussian topography from the 2-D Fourier transform, i.e.,

$$a = \frac{\alpha}{\sqrt{2}\omega \sin\frac{\sigma}{2}} \tag{5.3}$$

and the rms fluctuation in topography, ζ, by applying numerical integration to Equation 5.2 assuming

$$\Phi(\mathbf{k}) = \frac{\zeta^2}{4\pi} a^2 e^{-||\mathbf{k}||^2 a^2/4} \tag{5.4}$$

$$\Omega = 1. \tag{5.5}$$

The advantage of this theory is that it directly relates the statistical properties of a rough surface to scattering probabilities. This is in contrast to the approach taken by *Earle and Shearer* (1997), who generated Kirchhoff synthetics from specific realizations of random topography.

5.3 Scattering throughout the Earth

Fine-scale seismic structure is likely present in nearly every depth range throughout the Earth, possibly excepting the liquid outer-core (*Shearer*, 2015). In this section, we explore the possibility of scattering contributions to the observed $PKKP$ precursors from many of these depth-ranges including the core, the lower mantle, and the shallow Earth.

5.3.1 Inner-core scattering and $PKIJKP$

Strong scattering by small-scale structure within the solid inner core has been proposed previously by several studies. *Vidale and Earle* (2000) and *Peng*

et al. (2008) modeled $PKiKP$-coda as backscattered energy originating from just beneath the inner-core boundary. It has also been suggested that strong, small-scale heterogeneity throughout the inner-core could be primarily responsible for inner-core attenuation observed at frequencies near 1 Hz (*Cormier et al.*, 1998).

We find, however, that heterogeneity within the inner core does not produce observable precursors to $PKKP_{bc}$, provided that one assumes a realistic value for the inner-core attenuation, $1/Q_\alpha$. If one relaxes this constraint and allows for arbitrarily large inner-core Q_α, $PKIJKP$—a core phase with an underside reflection and conversion at the inner-core boundary—becomes visible in the precursor window of the synthetics. This phase displays large amplitudes at short ranges and small amplitudes at long ranges, as do the observations, but the emergent nature of the observed precursors is not well-matched by this candidate, as $PKIJKP$ is not a scattered phase. Moreover, it is unlikely that $PKIJKP$ can be seen in global stacks, given what is known about the bulk attenuation of the inner core.

Topography on the inner-core boundary (e.g., *Cao et al.*, 2007) may also scatter energy; we did not explicitly test this scenario because the ray geometries involved are expected to be very similar to those of energy scattered by inner-core heterogeneity.

5.3.2 Outer-core scattering

Although it is generally assumed that the fluid outer core is well mixed (*Stevenson*, 1987), we test to see if scattering in this region might contribute energy to the observed signal. Back-scattering from a heterogeneous layer at the top of the outer core with variable thickness between 100–300 km indeed generates precursors to $PKKP_{bc}$ in our synthetics. These precursors, however, behave much like those produced from CMB topography: they are too large at ranges $> 90°$ and too small at ranges $< 90°$. Forward-scattering in the outer core is unlikely from evidence from PKP precursor onset times, but backward-scattering is permissible. However, it is difficult to imagine a mechanism the scatters energy in the backward direction only, so we pursue this candidate no further.

5.3.3 CMB topography

Of all the scattering models that we tried, CMB topography produces synthetics that most closely resemble the observed data stacks. The observations are best matched when 20% of the CMB-reflected energy is scattered according to Gaussian scattering probabilities with a width of 15° (Figure 5.2, center panel). Increasing the overall scattering probability tends to increase the scattered amplitudes at all times. Increasing the Gaussian width (i.e., increasing the average scattering angle) tends to affect the time-dependence of the precursor energy; larger angles generally redirect a greater proportion of energy to earlier times. The main problem with these models, again, is that they systematically underpredict the observations at short ranges and overpredict the observations at long ranges. We find that our preferred model is associated with a Gaussian correlation length of 7 km and an rms topography fluctuation of 440 m. These findings are largely consistent with those reported by *Earle and Shearer* (1997), although our preferred rms topography fluctuation is outside of their preferred range of 250–350 m.

5.3.4 Lower-mantle scattering

Volumetric heterogeneity in the lower mantle also excites visible precursors to $PKKP_{bc}$, provided that the rms pertrubations are on the order of 1%. This model is problematic for two reasons: (1) synthetics associated with this model display a wide bump of strong energy from -60 to -20 s at ranges near $\sim$86°, whereas the observations show no such feature; and (2) it is difficult to reconcile this model with observations of PKP precursors that suggest weak small-scale variations on the order of 0.1% in the lowermost mantle (*Margerin and Nolet*, 2003; *Mancinelli and Shearer*, 2013).

5.3.5 Scattering near the Earth's surface

Finally, structure near the Earth's surface can produce precursors to $PKKP_{bc}$. This energy is thought to be scattered from teleseismic P to PKP, or vice-versa, near or at the underside reflection from the free surface. The focusing effect of

the b-caustic amplifies this energy, termed $P \bullet PKP$, and is likely responsible for $PKKP_x$—high-frequency energy observed at ranges beyond the c caustic (*Earle and Shearer*, 1998; *Earle*, 2002).

Both volumetric heterogeneity in the lithosphere/upper-mantle and topography at the Earth's surface can generate precursors to $PKKP_{bc}$. This model is problematic, however, because these precursors have much earlier onset times than those observed (Figure 5.2, left panel), particularly at long ranges. Moreover, synthetics associated with this model display relatively constant power at greater times; this is at odds with the emergent nature of the observed energy.

It is interesting that the heterogeneity parameters for the lithosphere and upper mantle published by *Shearer and Earle* (2004) predict synthetic precursors that are much larger than the observations (not shown). This suggests that either (1) the strength of $P \bullet PKP$ varies laterally and our signal-to-noise check is doing its job of rejecting the set of seismograms that are contaminated by this energy; or (2) the *Shearer and Earle* (2004) model underestimates the role of intrinsic attenuation in the mantle and thus $P \bullet PKP$ retains too much energy. Explanation (1) is more likely due to the clear observations of $P \bullet PKP$ made at the LASA array by *Earle* (2002).

After exploring all of these models, we find that CMB topography is most likely responsible for the observed precursors to $PKKP_{bc}$. These models, however, still fail to explain the observed range-dependence. In the following section, we show that improved fits can be achieved through more careful modeling of the reference phase $PKKP_{bc}$.

5.4 The validity of ray theory

One possible reason that scattering models might fail to match the observed range-dependence is if ray theory breaks down for rays turning near the ICB. This would result in lower relative $PKKP_{bc}$ amplitudes at short ranges near the c-caustic, as finite-frequency waves begin to sense inner-core structure. We test this idea by generating ∼1-Hz reflectivity synthetics (e.g., *Choy et al.*, 1980) for

the *bc* branch. This involves applying the Earth Flattening Transformation to *iasp*91 and approximating the result with a model of 500 uniform layers. The layer thicknesses vary with depth, but are around 20–30 km (in Flat Earth coordinates) in the vicinity of the ICB. We generate synthetic seismograms accurate to 1.05 Hz for slowness values between 0.005 and 0.07 s/km; the slowness spacing is on the order of 10^{-6} s/km. The result of this test, shown in Figure 5.3, indicates that the amplitudes of $PKKP_{bc}$ are only significantly affected by finite-frequency effects at ranges less than $\sim 78^{\circ}$. Since we are concerned with improving the fits at ranges between 80° and 100°, it is unlikely that the limitations of ray theory are causing the systematic misfits to the observations.

5.5 Perturbing the outer-core velocity gradient

Another factor that affects the amplitude of $PKKP_{bc}$ is geometrical spreading. This is handled in the phonon code by counting the number of phonons that return to the free surface in any given time–range bin. Increasing (or decreasing) the velocity gradient in a particular depth range refracts more (or fewer, respectively) phonons into a particular range bin at the free surface. Thus, the amplitude of the $PKKP_{bc}$ branch can be reduced near the *c*-caustic by reducing the *P*-velocity gradient just above the ICB. Likewise, the amplitude of the $PKKP_{bc}$ branch can be increased away from the *c*-caustic by increasing the *P*-velocity gradient in a layer located a few hundred km above the ICB. We find that imposing a reduction in the velocity gradient at 250 km above the ICB significantly improves our ability to match the observed range-dependence with a model of CMB topography. A few of these velocity profiles are shown in Figure 5.4.

5.6 A plausible velocity model for the base of the outer core

Although we are able to achieve better fits to the $PKKP_{bc}$ precursor stacks by perturbing the velocity gradient of the outer core, we would be remiss to ignore

the effect this has on the travel-times of the core phases. In this section, we attempt to find a model that improves fits to the $PKKP_{bc}$ precursor amplitudes while maintaining reasonable fits to PKP_{bc} travel-times. As a first step, we replace our initial 1-D model, *iasp*91 (*Kennett and Engdahl*, 1991), with its update, *ak*135 (*Kennett et al.*, 1995). The updated model is highly similar to *iasp*91, except in the region above the ICB where a reduced velocity gradient is imposed to provide better fits to the core phases. Upon first glance, model *ak*135 is appealing because it features a layer of reduced velocity-gradient above the ICB. After generating synthetics from this model, however, we find no significant improvement to the data fits. This is likely because the gradient reduction in *ak*135 occurs at about 100 km above the ICB, but our earlier results suggest that the reduction ought to be much higher, at about 250 km above the ICB, if we are to achieve better fits to $PKKP_{bc}$ precursors.

While *ak*135 is generally accepted as one of the best models for modeling the travel-times of a broad range of core phases, it does not perfectly match the observed travel-times of every individual phase. Observed travel-time residuals of PKP_{bc} with respect to *ak*135 suggest an increased velocity gradient in a layer 400–550 km above the ICB and a decreased gradient at depths in a layer 0–300 km above the ICB (*Souriau*, 2015, Fig. 2b). We design a 1-D velocity model that has a visible reduction in velocity gradient at about 250 km above the ICB and fits the observed travel-time residuals of *Souriau* (2015), as shown in Figure 5.4.

This model clearly improves the fits to the $PKKP_{bc}$ precursor observations at 86° and 90° by increasing the relative precursor amplitudes at these ranges (Figure 5.2, right panel). An additional (and unexpected) improvement from this model occurs at 106°, where the direct $PKKP_{ab}$ amplitude the resembles the data more closely than before. The most apparent flaw of our new model appears at 102°, where the synthetic precursor amplitudes are much larger than are observed. This may be due to the tunneling effect of the *ab* branch past the *a* point, which would likely increase the amplitude of the reference phase at 102°.

5.7 Discussion

Several previous studies support the idea of a decreased velocity gradient in the lowermost outer core, suggesting a change in composition (or phase) that raises the density of the fluid approaching the ICB. To model PKP_{bc} and PKP_c-diffracted traveltimes, *Souriau and Poupinet* (1991) used a liquid core model in which the velocity is constant in the lowermost 150 km of the fluid core. *Song and Helmberger* (1992) modeled PKP waveforms with a low-velocity gradient in the lowermost 400 km of the fluid core. This resulted in the proposal of PREM2 (*Song and Helmberger*, 1995), a P-velocity model for the core that shows a better fit to PKP differential travel times, amplitude ratios, and waveforms than does PREM (*Dziewonski and Anderson*, 1981). PREM2 is much like $ak135$, having nearly constant velocity throughout the lowermost 100 km of the outer core.

More recently, *Yu et al.* (2005) argue for large-scale lateral variability in lowermost outer-core structure using differential travel times, waveforms, and amplitude ratios of core phases. Rays traversing the eastern hemisphere are best explained by PREM, whereas data traversing the western hemisphere are better explained by another model (called OW) that has reduced velocities relative to PREM in the lowermost 200 km of the outer core. Another study by *Zou et al.* (2008) found that travel times of $PKPc$-diffracted favor models with a reduced gradient like $ak135$, while $PKPc$-diffracted amplitudes favor PREM-like models. The authors suggest that this paradox may be reconciled by introducing a low Q_α zone in the bottom 350 km of the outer core. *Adam and Romanowicz* (2015) report global observations of a mystery (M-) phase, which likely represents scattered energy from the vicinity of the inner-core boundary. *Adam and Romanowicz* (2015) tentatively explain the travel times of this phase by invoking an increased gradient from 100 to 400 km above the ICB with a 50-km-thick low-velocity layer right above the ICB. The two regions are connected by a 50-km-thick transition with a steep negative velocity gradient. We test an outer-core velocity model with a low-velocity layer similar to that proposed by *Adam and Romanowicz* (2015), but we found that this model generates precursors that are much too large at ranges from 75–85°, likely because the low-velocity layer dramatically reduces the direct

$PKKP_{bc}$ amplitudes at ranges less than $\sim$85°.

5.8 Conclusion

In summary, we find that commonly-used reference models such as *iasp*91 and *ak*135 do not adequately explain the relative amplitudes between $PKKP_{bc}$ phases and their precursors. We propose a new reference model that better fits both (1) PKP_{bc} travel-time constraints adapted from *Souriau* (2015), and (2) $PKKP_{bc}$ precursor amplitudes, assuming that CMB scattering is the primary cause of the observed precursor energy. We test and rule out contributions of scattered energy from the inner-core, the outer-core, and the lower-mantle. Although there remains the possibility that the precursor window is partially contaminated by $P \bullet PKP$ energy scattered near the Earth's surface, we are unable to find a model of near-surface scattering that explains the time- and range-dependence of the observations as well as do models of CMB topography.

Acknowledgements

This research was supported by National Science Foundation grant EAR-111111 and the National Science Foundation Graduate Research Fellowship Program. The facilities of IRIS Data Services, and specifically the IRIS Data Management Center, were used for access to waveforms and related metadata used in this study. IRIS Data Services are funded through the Seismological Facilities for the Advancement of Geoscience and EarthScope (SAGE) Proposal of the National Science Foundation under Cooperative Agreement EAR-1261681.

Chapter 5, in full, has been submitted for publication of the material as it may appear in Geophysical Research Letters: Mancinelli, N. J., and P. M. Shearer, Evidence for a reduced velocity gradient in the lowermost outer core from the range dependence of $PKKP$ precursor amplitudes. I was the primary investigator and author of this paper.

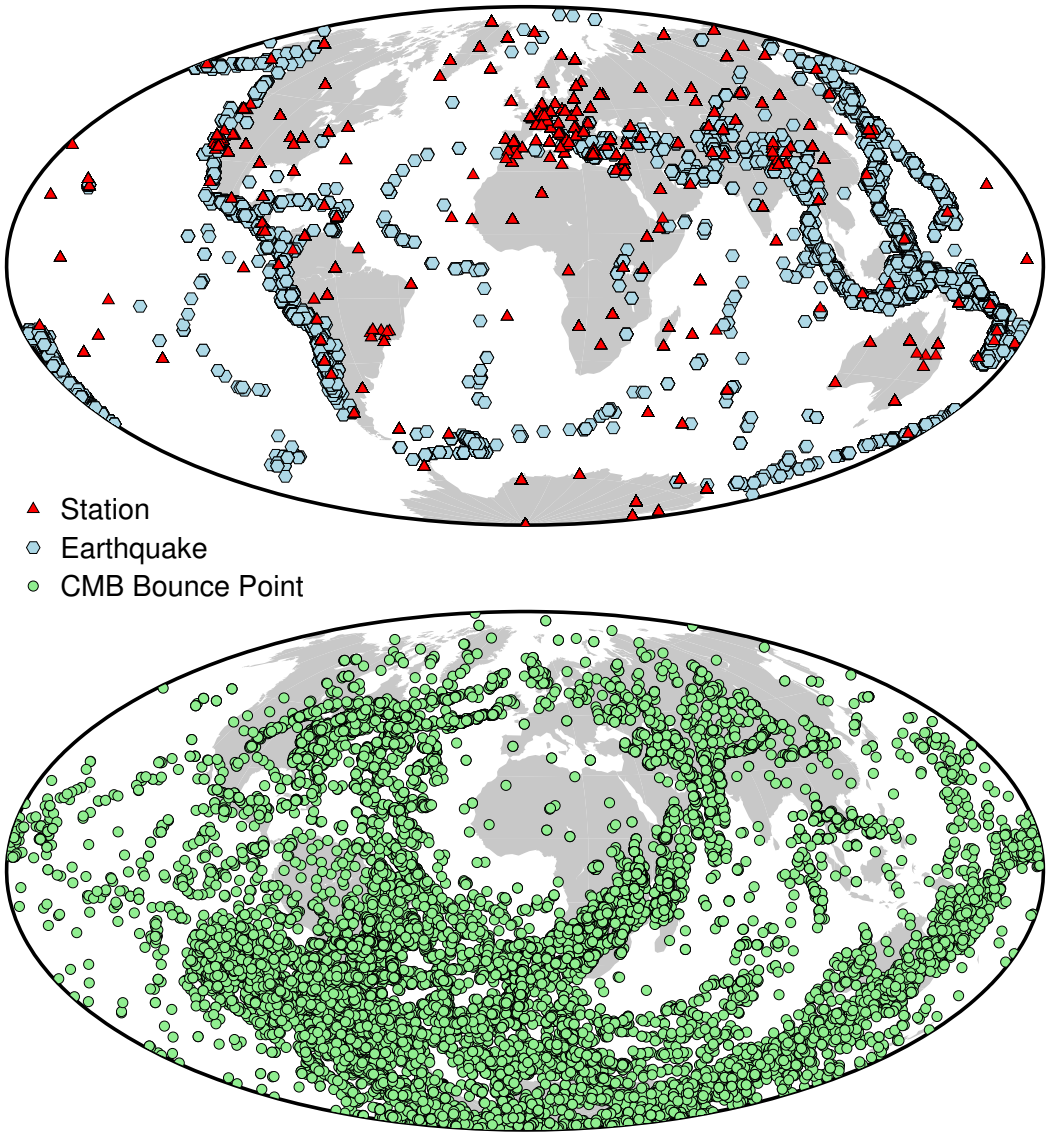

Figure 5.1: Spatial distribution of the $PKKP$ dataset used in this study. The upper map shows the source–receiver locations for the ∼17,000 recordings that passed our signal-to-noise test; the lower map shows corresponding CMB underside reflection points.

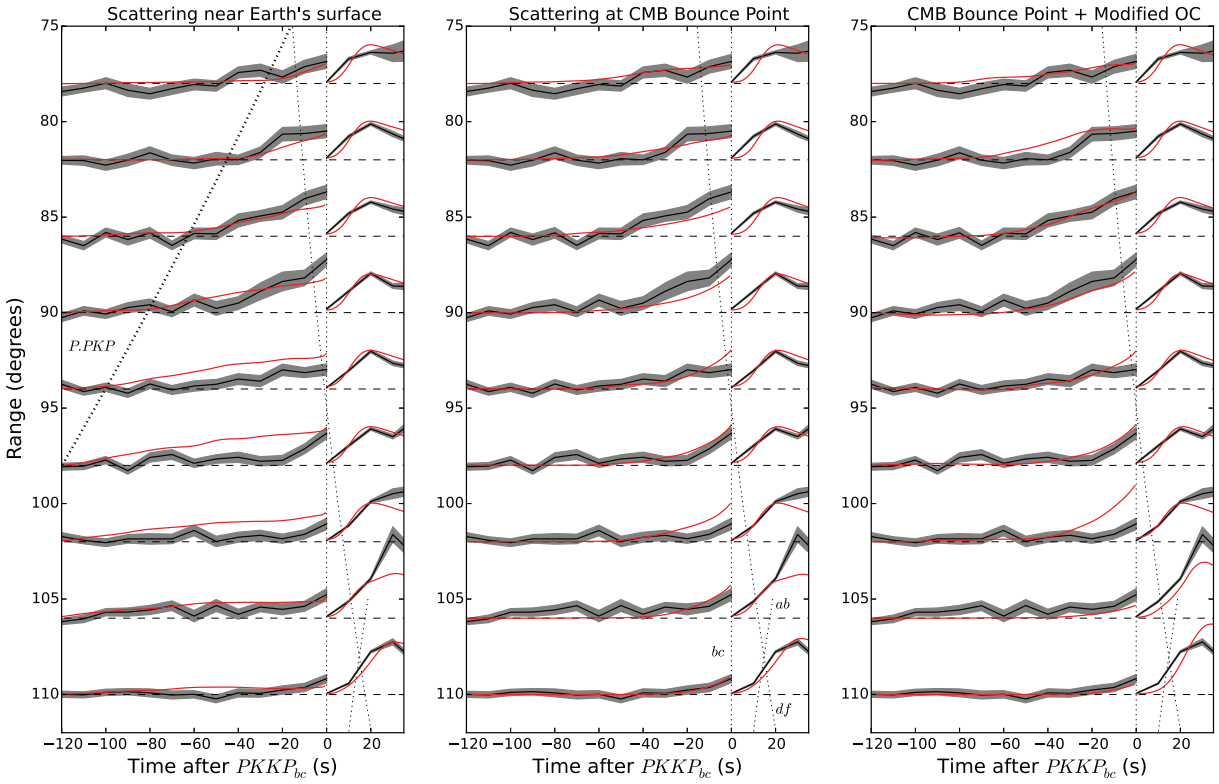

Figure 5.2: Globally-averaged $PKKP$ precursor stacks (black); the standard error of the mean is shown by gray shading. The red curves represent phonon code predictions for scattering (left) in the uppermost 200 km of the mantle; (center) at the CMB reflection point; and (right) at the CMB reflection point with a decreased gradient in the outer core. The precursors are scaled by a factor of 15 to enhance visibility. The thick dotted line in the left panel delineates onset times for $P \bullet PKP$ scattering at the Earth's surface.

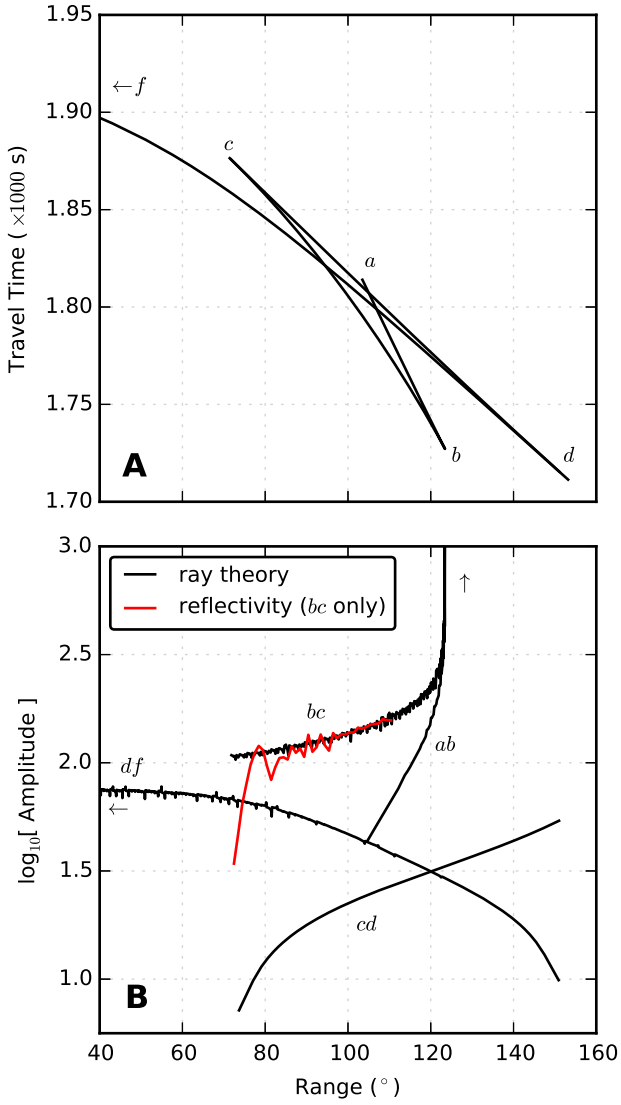

Figure 5.3: **(A)** Ray-theoretical travel times of the $PKKP$ triplication for velocity model *iasp*91. **(B)** Comparison between ray-theoretical and 1-Hz reflectivity amplitudes for $PKKP_{bc}$. On the *bc* branch near the *c*-caustic, the reflectivity amplitudes decrease more rapidly than the ray-theoretical amplitudes as finite-frequency waves begin to sense inner-core structure. Note that all amplitudes are relative and that the $PKKP_{df}$ amplitudes shown do not include the effects of inner-core attenuation or the transmission coefficient at the ICB.

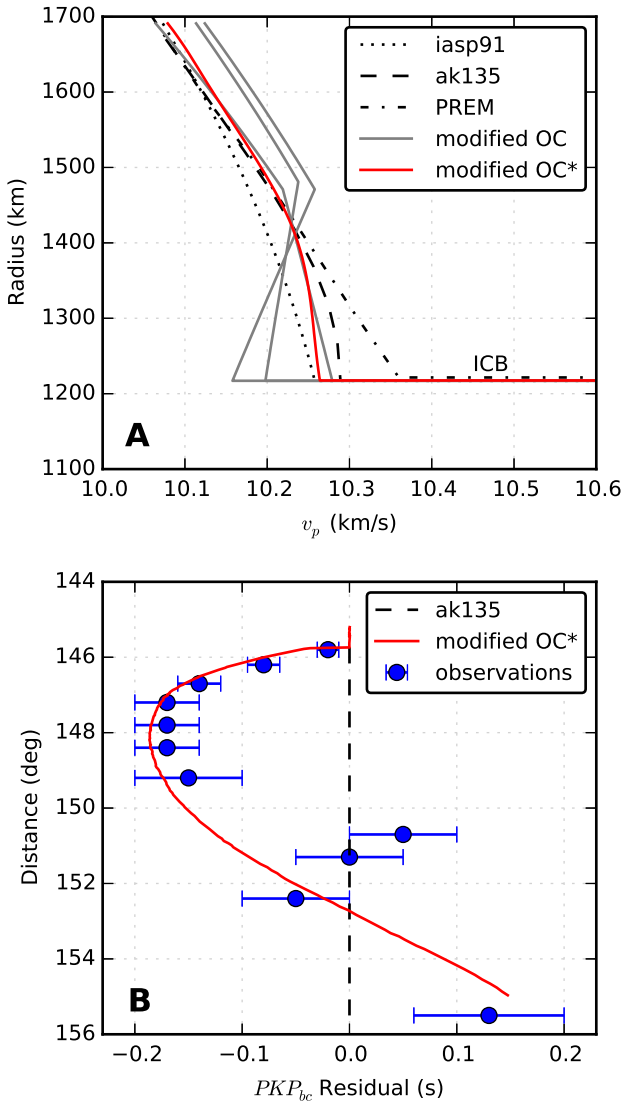

Figure 5.4: **(A)** One-dimensional reference models of the lowermost outer-core. The initial model we use is *iasp*91 (*Kennett and Engdahl*, 1991); models *ak*135 (*Kennett et al.*, 1995) and PREM (*Dziewonski and Anderson*, 1981) are plotted for comparison. The collection of models plotted in grey allow us to better fit the range dependence of the $PKKP$ precursors, but degrade fits to PKP travel-times. The model plotted in red allows for better fits to the range dependence of the observations, and it also predicts ray-theoretical travel times that match the PKP_{bc} residuals measured by *Souriau* (2015). **(B)** Comparison between the observed travel-time residuals (blue) reported by *Souriau* (2015) (blue) and the ray-theoretical prediction corresponding to the model denoted by an asterisk (red).

References

Adam, J.-C., and B. Romanowicz (2015), Global scale observations of scattered energy near the inner-core boundary: Seismic constraints on the base of the outer-core, *Physics of the Earth and Planetary Interiors*, *245*, 103–116, doi: 10.1016/j.pepi.2015.06.005.

Bataille, K., and S. M. Flatté (1988), Inhomogeneities near the core–mantle boundary inferred from scattered PKP waves recorded at the Global Digital Seismograph Network, *Journal of Geophysical Research*, *93*(B12), 15,057–15,064, doi:10.1029/JB093iB12p15057.

Bataille, K., R. S. Wu, and S. M. Flatté (1990), Inhomogeneities near the core-mantle boundary evidenced from scattered waves: A review, *Pure and Applied Geophysics*, *132*(1-2), 151–173, doi:10.1007/BF00874361.

Cao, A., Y. Masson, and B. Romanowicz (2007), Short wavelength topography on the inner-core boundary, *Proceedings of the National Academy of Sciences*, *104*(1), 31–35, doi:10.1073/pnas.0609810104.

Chang, A. C., and J. R. Cleary (1981), Scattered PKKP: Further evidence for scattering at a rough core-mantle boundary, *Physics of the Earth and Planetary Interiors*, *24*(1), 15–29, doi:10.1016/0031-9201(81)90075-3.

Choy, G. L., V. F. Cormier, and R. Kind (1980), A comparison of synthetic seismograms of core phases generated by the full wave theory and by the reflectivity method, *Journal of the Royal Astronomical Society*, *61*(1), 21–39, doi: 10.1111/j.1365-246X.1980.tb04301.x.

Cormier, V. F., L. Xu, and G. L. Choy (1998), Seismic attenutation of the inner core: Viscoelastic or stratigraphic?, *Geophysical Research Letters*, *25*(21), 4019–4022.

Doornbos, D. J. (1974), Seismic Wave Scattering Near Caustics: Observations of PKKP Precursors, *Nature*, *247*(5440), 352–353, doi:10.1038/247352a0.

Dziewonski, A. M., and D. L. Anderson (1981), Preliminary Reference Earth Model, *Physics of the Earth and Planetary Interiors*, *25*(4), 297–356.

Earle, P. S. (2002), Origins of high-frequency scattered waves near $PKKP$ from large aperture seismic array data, *Bulletin of the Seismological Society of America*, *92*(2), 751–760, doi:10.1785/0120010169.

Earle, P. S., and P. M. Shearer (1997), Observations of $PKKP$ Precursors Used to Estimate Small-Scale Topography on the Core-Mantle Boundary, *Science*, *277*(5326), 667–670, doi:10.1126/science.277.5326.667.

Earle, P. S., and P. M. Shearer (1998), Observations of high-frequency scattered energy assocated with the core phase $PKKP$, *Geophysical Research Letters*, *25*(3), 405–408.

Kennett, B. L. N., and E. R. Engdahl (1991), Traveltimes for global earthquake location and phase identification, *Geophysical Journal International*, *105*(2), 429–465, doi:10.1111/j.1365-246X.1991.tb06724.x.

Kennett, B. L. N., E. R. Engdahl, and R. Buland (1995), Constraints on seismic velocities in the Earth from traveltimes, *Geophysical Journal International*, *122*(1), 108–124, doi:10.1111/j.1365-246X.1995.tb03540.x.

Mancinelli, N. J., and P. M. Shearer (2013), Reconciling discrepancies among estimates of small-scale mantle heterogeneity from PKP precursors, *Geophysical Journal International*, *195*(3), 1721–1729, doi:10.1093/gji/ggt319.

Mancinelli, N. J., P. M. Shearer, and Q. Liu (2015), Constraints on the heterogeneity spectrum of the upper mantle, *Journal of Geophysical Research*, *Submitted*.

Margerin, L., and G. Nolet (2003), Multiple scattering of high-frequency seismic waves in the deep Earth: PKP precursor analysis and inversion for mantle granularity, *Journal of Geophysical Research*, *108*(B11), 2514.

Peng, Z., K. D. Koper, J. E. Vidale, F. Leyton, and P. Shearer (2008), Inner-core fine-scale structure from scattered waves recorded by LASA, *Journal of Geophysical Research*, *113*(B9), B09,312, doi:10.1029/2007JB005412.

Shearer, P. M. (2015), *Deep Earth Structure: Seismic Scattering in the Deep Earth*, vol. 1, 759–787 pp., Elsevier B.V., doi:10.1016/B978-0-444-53802-4.00018-X.

Shearer, P. M., and P. S. Earle (2004), The global short-period wavefield modelled with a Monte Carlo seismic phonon method, *Geophysical Journal International*, *158*(3), 1103–1117, doi:10.1111/j.1365-246X.2004.02378.x.

Shearer, P. M., and P. S. Earle (2008), Observing and modeling elastic scattering in the deep Earth, *Advances in Geophysics*, *50*, 167–193.

Song, X., and D. V. Helmberger (1992), Velocity structure near the inner core boundary from waveform modeling, *Journal of Geophysical Research*, *97*(B5), 6573–6586.

Song, X., and D. V. Helmberger (1995), A P wave velocity model of Earth's core, *Journal of Geophysical Research*, *100*(B6), 9817, doi:10.1029/94JB03135.

Souriau, A. (2015), Presumption of large-scale heterogeneity at the top of the outer core basal layer, *Earth and Planetary Science Letters*, *415*, 175–182, doi:10.1016/j.epsl.2015.01.024.

Souriau, A., and G. Poupinet (1991), The velocity profile at the base of the liquid core from PKP(BC+Cdiff) data: An argument in favour of radial inhomogeneity, *Geophysical Research Letters*, *18*(11), 2023, doi:10.1029/91GL02417.

Stevenson, D. (1987), Limits on lateral density and velocity variations in the Earth's outer core, *Geophysical Journal International*, *88*(1), 311–319, doi: 10.1111/j.1365-246X.1987.tb01383.x.

Vidale, J., and P. Earle (2000), Fine-scale heterogeneity in the Earth's inner core, *Nature*, *404*(6775), 273–5, doi:10.1038/35005059.

Yu, W.-c., L. Wen, and F. Niu (2005), Seismic velocity structure in the Earth's outer core, *Journal of Geophysical Research*, *110*(B02302), doi:10.1029/ 2003JB002928.

Zou, Z., K. D. Koper, and V. F. Cormier (2008), The structure of the base of the outer core inferred from seismic waves diffracted around the inner core, *Journal of Geophysical Research: Solid Earth*, *113*(5), 1–13, doi:10.1029/2007JB005316.

Chapter 6

Conclusion

6.1 Summary of findings

We have made progress in addressing our original research question: how strong is heterogeneity within the Earth's mantle and how is this strength distributed across different scale lengths? Major accomplishments include: (1) successful modeling of several scattered phases at a variety of frequencies; (2) new constraints on upper-mantle heterogeneity at scales from 5–500 km; and (3) relating constraints from tomography, long-period scattering, and high-frequency scattering to a single heterogeneity spectrum. Below we briefly review the other main findings presented in this thesis.

In Chapter 2, we found that small-scale ($\sim$10 km) heterogeneity in the lowermost mantle is weak (rms perturbations of $\sim$0.1%), in agreement with *Margerin and Nolet* (2003). We found the bug in the code used by *Hedlin et al.* (1997) that was responsible for the previously published value of 1%. We confirmed that the small-scale structure is likely distributed throughout the lowermost mantle, rather than concentrated near the core–mantle boundary. Scattering from within the upper mantle and lithosphere is likely much stronger than scattering from within the lower mantle, as evidenced by the strong PKP coda.

In Chapter 3, we characterized and modeled PKP precursor amplitudes over a range of frequencies in order to constrain the broader spectrum of heterogeneity within the lowermost mantle. From low-frequency precursors, in particular,

we found evidence for structure larger than ∼8 km in size. We also observed large-scale lateral variations in PKP precursor amplitudes, which are deemed significant based on bootstrap resampling tests. We used array processing techniques on an improvised array of stations to locate scatterers near the core–mantle boundary beneath Southern California.

In Chapter 4, we characterized and modeled long-period P-coda in order to place constraints on intermediate scales of heterogeneity within the upper mantle. We proposed a single spectrum that matches constraints from (1) long-period scattering observations, (2) high-frequency scattering observations, and (3) results from seismic tomography. The fall-off rate of the spectrum appears to be consistent with a self-similar mixture of basalt and harzburgite.

In Chapter 5, we stacked and modeled $PKKP$ precursor amplitudes to constrain short-wavelength topography on the core–mantle boundary. We ruled out scattering contributions from other depth regions, including the core and lower-mantle. We found that standard 1-D models of seismic velocity fail to predict the observed relative amplitudes between $PKKP$ and their precursors. We proposed a new 1-D model with a 250-km-thick reduced gradient above the inner-core boundary that provides a better match to the observations, while improving fits to absolute PKP_{df} travel times.

6.2 Future research directions

6.2.1 Pdiff coda and $PKKP_x$

A study of high-frequency Pdiff coda by *Earle and Shearer* (2001) showed that the long-duration of the scattered wavetrain can be modeled by imposing rms velocity perturbations of 1% throughout the mantle. We explicitly showed in Chapter 2, however, that perturbations of such strength predict PKP precursor amplitudes that are much larger than those observed. At the time of the *Earle and Shearer* (2001) study, it was assumed that 1% was the appropriate constraint from PKP precursors (*Hedlin et al.*, 1997), so the authors made an effort to find a model that could explain Pdiff coda while being consistent with earlier results. Now that

the constraint from PKP precursors has been revised, the time is right to revisit Pdiff coda. *Earle and Shearer* (2001) used a hybrid approach: the scattering effects were modeled using ray theory while diffraction at the core–mantle boundary was modeled by computing amplitudes from reflectivity. The phonon code—in its current form—is based entirely on ray theory, so some method development needs to be done in order to handle diffraction effects.

An alternative mechanism for the generation of Pdiff coda is multiple scattering near the core–mantle boundary (e.g., *Bataille and Lund*, 1996), but this hypothesis may be difficult to reconcile with the emergent nature of PKP precursors, which favors single scattering from heterogeneity distributed uniformly across lowermost mantle depths.

Another scattered phase, $PKKP_x$, consists of emergent high-frequency energy extending beyond the $PKKP$ c-caustic and was first documented by *Earle and Shearer* (1998). This phase, initially thought to originate from scattering at depth, has been reinterpreted as $P \bullet PKP$—energy scattered near the Earth's surface from teleseismic P into the PKP b-caustic—based on slowness measurements from the LASA array (*Earle*, 2002). Time-domain modeling of this phase may provide additional constraints on near-surface heterogeneity, which, when combined with constraints from P-coda, may help resolve the depth extent of scattering from within the upper-mantle and may offer additional constraints on the competing effects of scattering versus intrinsic attenuation.

6.2.2 Phase velocity spectra

In Chapter 4, we used tomography spectra compiled and published by *Meschede and Romanowicz* (2015) to obtain long-wavelength constraints on the heterogeneity spectrum. Alternatively, one may be able to derive constraints from long-period phase velocity maps (e.g., *Ekström*, 2011). For example, from an arbitrary random realization of our preferred heterogeneity spectrum from Chapter 4, we can obtain associated phase velocity maps that represent the average velocity structure over some depth ranges. Spherical harmonic spectra from these maps

can be directly compared with those from phase velocity maps based on inversions of actual data. One complication that arises when performing this exercise is determining the relative importance of perturbations in v_p versus perturbations in v_s. As is common in scattering studies, we have assumed that $\frac{\delta v_p}{v_p}$ and $\frac{\delta v_s}{v_s}$ are equal, but this is not likely to hold for large-scale velocity changes that are primarily due to thermal effects. We look forward to further collaboration with Zhitu Ma and Guy Masters to develop this research more fully.

6.2.3 Modeling heterogeneity spectra with geodynamics

Allègre and Turcotte (1986) suggested that convective strains can deform and stir elongated strips of depleted lithosphere into the bulk mantle, thereby producing a marble-cake texture after billions of years. The P-coda results presented in Chapter 4 of this thesis may provide direct geophysical evidence for such mantle structure. To assess whether these observational constraints indeed suggest the presence of an incompletely-mixed marble-cake mantle, we propose to perform geodynamical calculations.

In collaboration with Dave Stegman, we plan to use StagYY (*Tackley*, 2008) to simulate three-dimensional mantle stirring processes for realistic Earth models. The code generates compositional heterogeneity at spreading ridges and injects it into the deeper mantle at subduction zones. After simulating 4 billion years of heterogeneity production, subduction, and subsequent stirring, we will convert the final compositional field to a model of seismic wavespeed perturbations using mineral physics relationships from *Xu et al.* (2008). We can assess how well the geodynamical calculations agree with our observational constraints by (1) examining the statistical properties of the geodynamic models (comparing spherical power spectra, e.g.), and (2) interpolating the geodynamics-based velocity model onto the SPECFEM3D_GLOBE (e.g., *Komatitsch et al.*, 2002) mesh in order to generate synthetic seismograms which then can be compared directly with observations.

6.3 Final remarks and outstanding challenges

The Earth's mantle appears to be heterogeneous at all scales that can be probed by seismic waves, from a few kilometers to thousands of kilometers. The upper mantle, in particular, is likely to contain significant amounts of compositional heterogeneity at small scales, giving the mantle a fractal-like character that is visually at odds with the artificially smooth tomography images that pervade the geophysical literature. This richness of small-scale structure may even control how waves are attenuated, especially at high-frequencies. An ultimate goal of this research is to develop a reference 1-D heterogeneity model that is able to produce the features of all the known scattered phases, including P-coda, Pdiff coda, PKP precursors, and $PKKP$ precursors, among others. Although the findings presented in this thesis bring us closer to this goal, several outstanding issues remain, including:

(1) The depth distribution of scattering in the upper mantle is poorly resolved. A major remaining challenge is determining the relative scattering contributions from heterogeneity within the crust and lithosphere versus those from heterogeneity in the asthenosphere and below. Analyses of scattered regional phases may help resolve this issue, but these phases are typically limited to shorter periods.

(2) The intermediate scale lengths in the lower mantle remain unconstrained. The challenge here is finding a phase that is sensitive to $\sim$100 km structure in the deep mantle. The time duration of PKP precursors is too short to be sensitive to structure much larger than a few tens of km, and long-period Pdiff coda can be adequately modeled with reasonable amounts of upper-mantle heterogeneity. Backscattered energy from $P' \bullet P'$ (e.g., *Rost et al.*, 2015) may help resolve this gap in the lower-mantle spectrum, but preliminary research suggests that the signal-to-noise ratio of this phase is quite poor.

(3) What is the role of anisotropic scattering? *Cormier* (1999) tested various models of anisotropic heterogeneity in the lower mantle, finding that isotropic heterogeneity produces the best fits to observations of broadband PKP precursors. Anisotropic heterogeneity is commonly invoked in order to explain the scattered re-

gional coda that appears to be channelled to long distances. *Kennett and Furumura* (2013), for example, invoked horizontally elongated heterogeneities throughout the lithosphere and asthenosphere to model the codas of Po and So.

The competing effects of heterogeneity in isotropic elastic parameters versus heterogeneity in anisotropic parameters should also be further explored. It is possible that 3-D variations in the orientations of olivine crystals may provide an alternative way to scatter seismic waves (Karen Fischer, personal communication) that does not require differences in bulk composition.

In conclusion, considerable work remains to be done in improving our understanding of the distribution of small-scale heterogeneity throughout the Earth, yet it is becoming increasingly evident that the mantle contains structure at many scale lengths. Our constraints on the upper-mantle heterogeneity spectrum may provide geophysical evidence for the gradual stirring of different compositions (i.e., basalt and harzburgite) within the mantle. An interesting observation is the order-of-magnitude difference between heterogeneity strength in the upper- and lower-mantle, as the latter appears to contain much weaker small-scale velocity perturbations than does the former. We speculate that this difference might be simply explained by the post-garnet phase transition at the base of the upper-mantle, which reduces the velocity contrast between the two components of the hypothesized marble-cake mantle from about 10% to less than 1% (*Stixrude and Lithgow-Bertelloni*, 2012). Of course, there are several other phase transitions throughout the upper mantle that are thought to affect the velocity contrast between compositions, so we look forward to conducting more detailed attempts at modeling this in the future.

References

Allègre, C. J., and D. L. Turcotte (1986), Implications of a two-component marble-cake mantle, *Nature*, *323*, 123–127, doi:10.1038/323123a0.

Bataille, K., and F. Lund (1996), Strong scattering of short-period seismic waves by the core-mantle boundary and the P-diffracted wave, *Geophysical Research Letters*, *23*(18), 2413–2416, doi:10.1029/96GL02225.

Cormier, V. F. (1999), Anisotropy of heterogeneity scale lengths in the lower mantle from $PKIKP$ precursors, *Geophysical Journal International*, *136*(2), 373–384, doi:10.1046/j.1365-246X.1999.00736.x.

Earle, P. S. (2002), Origins of high-frequency scattered waves near $PKKP$ from large aperture seismic array data, *Bulletin of the Seismological Society of America*, *92*(2), 751–760, doi:10.1785/0120010169.

Earle, P. S., and P. M. Shearer (1998), Observations of high-frequency scattered energy assocated with the core phase $PKKP$, *Geophysical Research Letters*, *25*(3), 405–408.

Earle, P. S., and P. M. Shearer (2001), Distribution of fine-scale mantle heterogeneity from observations of P_{diff} coda, *Bulletin of the Seismological Society of America*, *91*(6), 1875–1881, doi:10.1785/0120000285.

Ekström, G. (2011), A global model of Love and Rayleigh surface wave dispersion and anisotropy, 25-250s, *Geophysical Journal International*, *187*, 1668–1686, doi: 10.1111/j.1365-246X.2011.05225.x.

Hedlin, M. A. H., P. M. Shearer, and P. S. Earle (1997), Seismic evidence for small-scale heterogeneity throughout the Earth's mantle, *Nature*, *387*(6629), 145–150, doi:10.1038/387145a0.

Kennett, B. L. N., and T. Furumura (2013), High-frequency Po/So guided waves in the oceanic lithosphere: I—long-distance propagation, *Geophysical Journal International*, *195*(3), 1862–1877, doi:10.1093/gji/ggt344.

Komatitsch, D., J. Ritsema, and J. Tromp (2002), The spectral-element method, Beowulf computing, and global seismology, *Science*, *298*(5599), 1737–1742, doi: 10.1126/science.1076024.

Margerin, L., and G. Nolet (2003), Multiple scattering of high-frequency seismic waves in the deep Earth: PKP precursor analysis and inversion for mantle granularity, *Journal of Geophysical Research*, *108*(B11), 2514.

Meschede, M., and B. Romanowicz (2015), Lateral heterogeneity scales in regional and global upper mantle shear velocity models, *Geophysical Journal International*, *200*(2), 1076–1093, doi:10.1093/gji/ggu424.

Rost, S., P. S. Earle, P. M. Shearer, D. A. Frost, and N. D. Selby (2015), Seismic Detections of Small-Scale Heterogeneities in the Deep Earth, in *The Earth's Heterogeneous Mantle*, pp. 367–390, Springer, doi:10.1007/978-3-319-15627-9.

Stixrude, L., and C. Lithgow-Bertelloni (2012), Geophysics of chemical heterogeneity in the mantle, *Annual Review of Earth and Planetary Sciences*, *40*(1), 569–595, doi:10.1146/annurev.earth.36.031207.124244.

Tackley, P. J. (2008), Modelling compressible mantle convection with large viscosity contrasts in a three-dimensional spherical shell using the yin-yang grid, *Physics of the Earth and Planetary Interiors*, *171*, 7–18, doi:10.1016/j.pepi.2008.08.005.

Xu, W., C. Lithgow-Bertelloni, L. Stixrude, and J. Ritsema (2008), The effect of bulk composition and temperature on mantle seismic structure, *Earth and Planetary Science Letters*, *275*, 70–79, doi:10.1016/j.epsl.2008.08.012.